Politecnico
di Torino

Corso di laurea magistrale in ingegneria aerospaziale

Aeroelastic behavior of a parameterized sailplane wing using Tsai's Modulus

Relatore:

Prof. Alfonso Pagani

Correlatore:

Prof. Marco Petrolo

Referente aziendale:

Dott. Naresh Sharma, Phd;
CEO NASHERO SRL

Laureando:

Andrea Del Monte

Anno accademico 2023/2024

Ai miei cari

Ringraziamenti

Ci tengo a ringraziare tutte le persone che mi hanno supportato nella realizzazione di questo lavoro, senza le quali non sarebbe stato possibile. Vorrei ringraziare innanzitutto i miei relatori, i professori Alfonso Pagani e Marco Petrolo, che non mi hanno mai fatto mancare il loro sostegno, fornendomi preziosi consigli. Ringrazio anche il dottor Naresh Sharma, ideatore del tema di questa tesi, che mi ha ospitato presso la sua azienda, per avermi indicato la via per procedere e fungendo da guida per l'impostazione del modello su cui sono state eseguite le varie analisi.

Vorrei ringraziare, inoltre, tutte le persone che mi sono state vicine durante questi anni di università. Ringrazio innanzitutto la mia famiglia, che mi ha sempre sostenuto sin dalla mia infanzia e mi ha sempre aiutato a seguire la strada che più amavo. Ringrazio Elena, che mi ha dato sostegno e amore nei momenti più belli, ma anche soprattutto nei momenti di difficoltà. Senza di te sarebbe stato tutto più complicato.

Ringrazio poi tutti i miei amici e compagni di corso che mi hanno accompagnato durante questi anni e hanno reso questa avventura molto più divertente e piena, dentro e fuori il Politecnico.

Abstract

Today's design trends in aeronautics focus on decreasing structural weight and increasing aerodynamic efficiency in order to reduce emissions. These trends are towards slender aircraft configurations and are consequently prone to aeroelastic phenomena. At the same time composite materials allows to reduce structural weight and they are today's state of the art in aircraft industry. Furthermore, composite materials, with their different possible laminations that allows to induce coupling between bending and twisting deformation, can be exploited to counteract aeroelastic instabilities establishment, a phenomenon called aeroelastic tailoring.

In this context an invariant approach able to normalize stiffness components of every composite material could be tremendous in simplifying composite material design. Such invariant approach was not possible until Tsai and Melo published in 2014 their results about a novel invariant approach to describe elastic properties of composites plies and laminates. In this approach the trace of the plane stress stiffness matrix, namely Tsai's Modulus, is evaluated as a material property and it is an invariant.

Relatively to this, the present thesis aims to exploit the potentiality of this newly discovered invariant in the field of aeroelasticity. In particular, a finite element parametric sailplane wing model will be built to analyze flutter and divergence behaviour as function of material Tsai's Modulus. Tsai's Modulus is a measure of the total stiffness of an orthotropic composite material (longitudinal and shear combined). Since the focus is on composite materials, 2D orthotropic plate elements parameterized as function of Tsai's Modulus will be used for the FEM model. For aerodynamics loads evaluation the vortex lattice method (VLM) and doublet lattice method (DLM), two of the most powerful tools for linear aeroelastic analysis in subsonic regime, will be used respectively for steady and unsteady aerodynamics.

Since Tsai's Modulus measure exactly the total stiffness of an orthotropic laminated composite, given that the aeroelastic behaviour of a wing is inherently tied to its bending, torsion, and shear properties, it logically follows that it should also be influenced by Tsai's modulus of the material it is constructed from, as suggested by Dr. Sharma. Consequently, the primary objective of this thesis is twofold: first, to empirically verify the validity of this hypothesis, and secondly, if substantiated, to delineate the correlation between flutter behavior and Tsai's modulus. This investigation will be undertaken by conducting comprehensive parametric flutter analysis on the specified wing.

Should this hypothesis stand true, it implies that the process of wing design can be streamlined. Initial steps would involve identifying the optimal lamination sequence for the wing. Subsequently, the choice of the most suitable material becomes a straightforward task, contingent upon the desired flutter velocity.

Contents

1 Introduction 1

1.1 Historical aeroelasticity preface 1
1.2 Sailplane flutter 2
1.3 Aeroelasticity of composite wings 3
1.4 Stiffness effects on flutter 4
1.5 Aim of the thesis 5
1.6 Outline 5

2 Aeroelasticity theory 9

2.1 Structural dynamics 10
2.2 Static aeroelasticity 11
2.3 Dynamic aeroelasticity 12
  2.3.1 Simplified flutter mechanics 13
  2.3.2 P-method with steady aerodynamics 14
  2.3.3 P-method with quasi-steady aerodynamics 15
  2.3.4 p-k method 17
2.4 Aerodynamic models 18
  2.4.1 Vortex Lattice Method (VLM) 18
  2.4.2 Doublet Lattice Method (DLM) 20
  2.4.3 VLM and DLM application in aeroelastic analysis 21
2.5 Aeroelastic equations of motion 22
  2.5.1 Modal approach and generalized matrices 22

3 FEM theory 25

3.1 Reissner-Mindlin theory 25
3.2 Finite element "Reissner-Mindlin plate" 26
  3.2.1 Evaluation of stiffness matrix 28
  3.2.2 Evaluation of mass matrix 30

4 Tsai’s Modulus 33

4.1 What is Tsai’s Modulus 33
  4.1.1 Master ply for carbon/polymer composites 37
4.2 Tsai’s Modulus application in structural optimization and design 37

5 AVL **39**

5.0.1 Vortex lattice spacing distributions 40

6 Wing geometry definition **43**

7 Static sizing **47**

7.1 FEM Model 47

7.1.1 Mesh 47

7.1.2 Materials and global plies definition 51

7.1.3 Layups and properties definition 52

7.1.4 Boundary conditions and loads 54

7.2 Aerodynamics loads 55

7.2.1 2D airfoil aerodynamic characteristics 55

7.2.2 3D wing aerodynamic characteristic 56

7.2.3 V-n diagram 58

7.2.4 Pressure on wing 60

7.3 Sizing results 60

7.3.1 First results 60

7.3.2 Improvement in geometry 63

7.3.3 Final sizing 64

8 Modal analysis **67**

8.1 Normal modes and natural frequencies 68

8.2 Results comparison with analytic model 71

8.3 Results comparison with a FEM equivalent beam model 73

9 Flutter analysis **77**

9.1 Aerodynamic mesh 77

9.2 Analysis settings 78

9.3 Results 79

10 Parametric analysis and results **81**

10.1 Aeroelastic behaviour by varying the position of the main spar 81

10.2 Evaluation of the relationship between flutter speed and Tsai's Modulus . . . 83

10.2.1 Validity of the linear approximation 87

10.2.2 Example of application of the linear approximation 87

10.3 Evaluation of the relationship between divergence speed and Tsai's Modulus . 88

10.3.1 Validity of the linear approximation 91

11 Conclusions **93**

11.1 Outline 93

11.2 Concluding remarks 95

11.3 Further works 95

A AVL wing model **97**

B V-n parametric diagram definition **101**

C AVL mesh convergence analysis **105**

D DLM mesh definition **107**

Chapter 1

Introduction

1.1 Historical aeroelasticity preface

Aeroelasticity is an engineering study field concerning the interaction between aerodynamic loads applied on a deformable structure subject to inertial and damping effects.

Aeroelastic and structural-dynamic phenomena can result in dangerous static and dynamic deformations and instabilities and, thus, have important practical consequences in many areas of technology. Especially when one is concerned with the design of modern aircraft which are characterized by the demand for extremely lightweight structures [1].

One of the first appearance of aeroelastic problems in human handiwork was with windmills. The problem was solved empirically more than four hundreds years ago in Holland by moving the front spars of the blades from about midchord to quarter-chord position [2]. Aeronautical wise, aeroelastic instability is a phenomenon that affected aircraft almost since the beginning of aviation. Wright brothers discovered that by making the blades of the propeller much wider and thinner than the originals performance of propellers during flight did not agree closely with their calculation. This was due to the the propeller blades twisted in shape under aerodynamic pressure [2]. It is also speculated that Langley was not able to beat Wright brothers to the race to the first flight due to aeroelastic instability, as G.T.R. Hill suggested that failure on Langley's tandem monoplane (fig. 1.1) was the result of insufficient wing-tip stiffness resulting in wing torsional divergence [2].

To move a little closer in time, World War I planes were haunted by static divergence, that was solved at the time by ad hoc stiffening. The first recorded and documented case of aircraft flutter was that which occurred to a Handley Page O/400 biplane bomber during a flight in 1916. It experienced violent antisymmetric oscillations of fuselage and tail. Since then, with the increase of flight speed, flutter would have become a more and more big problem. From Theodorsen theory in the 30s huge progress in flutter prediction has been made, especially with the introduction of computational fluid dynamics in the means of Doublet lattice methods (DLM) or Navier-Stokes methods (RANS, URANS, LES). The former method, DLM, the one used in this thesis, was introduced in the late 60s thanks to Albano and Rodden [3] and then developed by Rodden and al. [4]. This method is still one of the most used nowadays for flutter prediction as [5]:

- it offers good accuracy (unless transonic regimes are considered or separation occurs);
- it is cost competitive with respect to simpler methods such as strip theories;
- fairly complex geometries can be analysed.

Higher fidelity methods, able to represent effects of viscosity, are required in case of presence of transonic regime or separation, requiring much higher computational costs.

Today's design trends are towards engineering solutions prone to aeroelastic phenomena, such as slender aircraft wings. Focus has, therefor, being put on composite materials design to try and postpone aeroelastic phenomena by means of aeroelastic tailoring. Thus, great attention has been put towards the study of new composite materials properties, such as Tsai's Modulus, a new invariant discovered by Tsai and Melo in 2014 [6] that defines elastic properties of composite plies and laminates, which will be the key focus of the thesis.

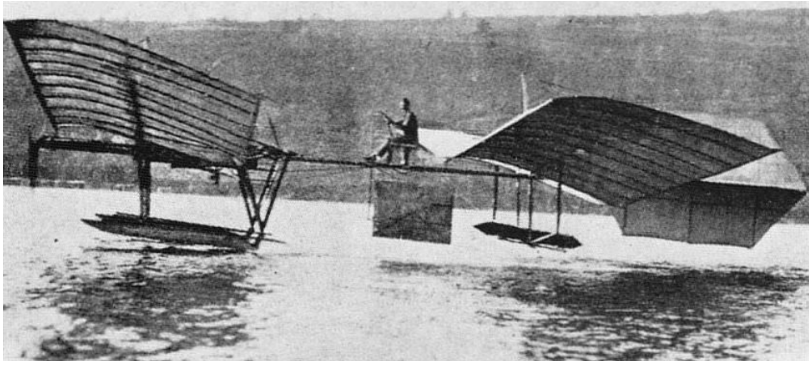

Figure 1.1: Langley's aerodrome

1.2 Sailplane flutter

Sailplanes (fig. 1.2) are aircraft heavier than air aircraft, usually non powered, designed for soaring and characterized by a very high aerodynamic efficiency, typically better than $L/D = 20$. They are certified by the European Aviation Safety Agency (EASA) according to the regulation CS 22.

Sailplanes benefit from producing very low drag using very long, slender and thin wings. As said before, this type of wing is very prone to flutter, therefore great attention must be put in the sailplane design to not incur in aeroelastic phenomena inside the flight envelope. The regulation, the CS 22.629, prescribes that the sailplane must be free from flutter, aerofoil divergence, and control reversal in each configuration and at each appropriate speed up to at least V_D (design maximum speed). Sufficient damping must be available at any appropriate speed so that aeroelastic vibration dies away rapidly. Compliance with that must be shown by a ground vibration test (GVT) which includes an analysis and an evaluation of the established vibration modes and frequencies for the purpose of recognising combinations critical for flutter, either by an analytical method, which will determine any critical speed in the range up to 1.2 V_D, or any other approved method [7]. Since the present thesis will be realized only on a computational base the absence of any aeroelastic instability up to 1.2 V_D will be verified

Figure 1.2: Rolladen-Schneider sailplane

based only on the modes evaluated through finite element analysis (FEM) and not via ground vibration testing.

1.3 Aeroelasticity of composite wings

As said before, targeted design advancements in aeronautics include wing structural weight reduction and increased wing aspect ratio to decrease lift-induced drag [8]. High aspect ratio wings operating at minimum weight are typically highly flexible structures prone to aeroelastic instabilities. Thus, composite wing could be the most efficient solution, as with aeroelastic tailoring distructive phenomena can be postponed at higher speed. Aeroelastic tailoring was defined by Shirk M. et al. [9] as “the embodiment of directional stiffness into an aircraft structural design to control aeroelastic deformation, static or dynamic, in such a fashion as to affect the aerodynamic and structural performance of that aircraft in a beneficial way". Aeroelastic tailoring can essentially modify the wing’s primary stiffness direction, changing the wing’s bending and torsional stiffness as well as the degree of coupling between the two. The wing’s primary stiffness direction is defined as the “locus of points where the structure exhibits the most resistance to bending deformation”. The structural reference axis is the “conventional wing structure elastic axis” [10]. If the primary stiffness axis is not coincident with the structural reference axis, the wing will have bendtwist coupling. When the primary stiffness direction is moved forward of the structural reference axis, the bendtwist coupling causes the wing to have more “wash-out” (leading edge down) characteristics. When the primary stiffness direction is moved behind the structural reference axis, the bend-twist coupling causes the wing to have more “wash-in” (leading edge up) characteristics. As can be seen in figure 1.3 moving the primary stiffness axis in either direction produces desirable changes in wing performance. Clearly a trade off between the two direction is needed to be found for every specific case.

Since variation on primary stiffness direction can be obtained mainly by changing lamination sequence an invariant approach to stiffness, by using Tsai’s Modulus, could play a key role in simplifying the wing design, as, once chosen the desired lamination, material selection could be executed only based on the required stiffness of the material to obtained for example a certain flutter speed, hence its Tsai’s Modulus. This is the kernel of the present thesis

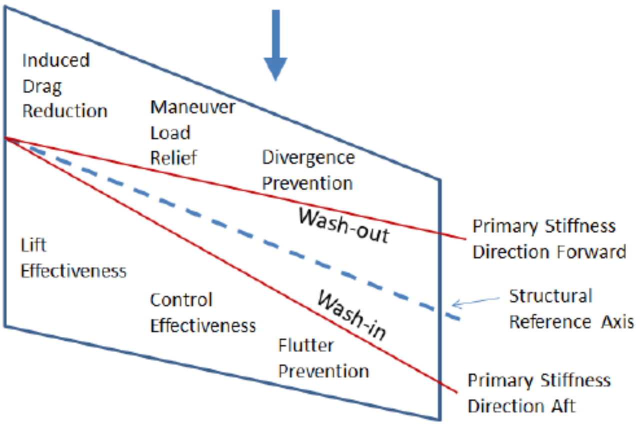

Figure 1.3: Effect of location of primary stiffness axis on wing behaviour [10]

as, if a relationship between flutter behaviour and Tsai's Modulus exists, then the choice of the ideal material for a wing would become the last step in the aeroelastic wing design, as it would be done only after having found the optimal lamination, as it is better explained in the sub-chapter 1.5.

1.4 Stiffness effects on flutter

Since stiffness is one of the key parameters, together with inertia and aerodynamics, that determines the establishment of flutter, great attention has been put in literature to study the effects of stiffness variation on flutter. From theory it is known that increasing stiffness properties will result in an increase in the natural frequencies and, therefor, an increase in the dissipated energy per cycle, since it depends on frequency [11]. However, a direct mathematical relationship between stiffness and flutter behaviour is still not known, therefor research on the influence of the first on the latter has been performing to the modern days, using from some of the easier methods such as 2 DOFs airfoil systems to way more accurate 3D methods that compute aerodynamics with unsteady Navier-Stokes methods. In 2022 Oskar Tylen [12] realized a CFD model based on a simple airfoil 2 DOF system, free to translate vertically and rotate around its elastic axis. The bending and torsional stiffness of a 3-dimensional airfoil was modeled using a flexural and torsional spring. To compute the fluid-dynamics around the airfoil a URANS (unsteady RANS) model was used, in order to be able to capture the airfoil oscillations. By running the simulations it was clear that the main parameter that determined flutter was the torsional degree of freedom. By increasing torsional stiffness it was possible to prevent flutter and improve damping characteristics. Qiao S. and al. performed a more sophisticated analysis [13], where they evaluated flutter around a 3D wing using a coupled implicit Spalart-Allmaras model to perform CFD. They evaluated stiffness of the wing by using an equivalent beam model. They evaluated that when the wing bending stiffness and torsional stiffness of each section along the span increase by an average of 8.28% and 5.22%, the flutter amplitude value decreases by approximately 30%. In general, they concluded that, in terms of the overall impact, the stiffness has a greater effect on the wing flutter critical speed. Increasing the wing stiffness overall increases the wing flutter critical speed. Similar effects of stiffness on flutter behaviour were found also by Barnes and Visbal [14], using even more sophisticated aerodynamics model, in the means of high order ILES (implicit large eddies simulations). In conclusion it appears that, despite an increase in the level of accuracy of the simulations, both on the FEM and CFD sides, the correlation between stiffness and flutter behaviour is maintained.

Since Tsai's Modulus measure exactly the total stiffness of an orthotropic laminated composite a similar correlation is expected, and it will be investigated throughout the present thesis.

1.5 Aim of the thesis

As can be better seen in chapter 4, it has been established through the classical lamination theory that Tsai's Modulus is a material constant [6] and it measures the total stiffness of an orthotropic composite material. The structural response of a system, encompassing characteristics like bending, torsion, and shear, is intrinsically linked to these material constants.

Given that the behaviour of a wing is inherently tied to its bending, torsion, and shear properties, it logically follows that it should also be influenced by Tsai's Modulus of the material it is constructed from.

Furthermore, flutter, a phenomenon closely intertwined with the structural dynamics of a wing, should exhibit a proportionate relationship with Tsai's Modulus. Consequently, the primary objective of this thesis is twofold: first, to empirically verify the validity of this hypothesis, and secondly, if substantiated, to delineate the correlation between flutter characteristics and Tsai's Modulus. This investigation will be undertaken by conducting a comprehensive parametric flutter analysis on the specified wing.

Should this hypothesis stand true, it implies that the process of wing design can be streamlined. Initial steps would involve identifying the optimal lamination sequence for the wing. Subsequently, the choice of the most suitable material becomes a straightforward task, contingent upon the desired flutter velocity. This streamlined approach capitalizes on the established connection between flutter velocity and Tsai's Modulus.

Credit for this statement must be done to Dr. Naresh Sharma, as he is the original thinker of a possible relationship between the flutter behaviour of a wing and Tsai's Modulus.

1.6 Outline

The present thesis is composed mainly by two parts. The first part consists of the first five chapters and it consists of a revision of theoretical notions related to the argument of the thesis. The second part, instead, summarizes the actual work executed to find the relationship between flutter behaviour of the sailplane wing and Tsai's Modulus, starting from the construction of the FEM model, passing through a static sizing to determine the wing's parts thicknesses, then a modal analysis is executed to identify the normal modes and, in the end, the flutter analysis is performed.

Chapter 2 presents some notes on aeroelasticity theory, describing every component taking part in this phenomena. First a rapid review of structural dynamics is given, since it is the starting point for any flutter analysis. Then it is present a fast review on static aeroelasticity with the definition of the divergence phenomenon. A more accurate description is provided for dynamic aeroelasticity, and especially flutter. Here the flutter establishment mechanism is briefly explained, then some flutter prediction methods are presented. Following an historical sequence, p-method with steady and quasi-steady aerodyanimcs, then p-k method with Theodorsen aerodynamic are presented, in order to allow the reader to understand how flutter prediction methods works with some simple methods. In the end, some aerodynamic models to predict steady and unsteady loads, in the means of VLM and DLM are enunciated. These are respectively the methods used in the present thesis to evaluate the steady loads for the static sizing and then to execute the flutter calculations.

Chapter 3 presents some notes on the FEM theory at the basis of the 2D plate elements. There the Reissner-Mindlin plate element is presented and then its stiffness and mass matrices are evaluated.

Chapter 4 presents the essence of Tsai's Modulus. First it is shown how Tsai and Melo deduced the invariant nature of Tsai's Modulus, using classical lamination theory and transformation relations. The essence of Tsai's Modulus is here explained, as it essentialy represents the total and upper bound of the stiffness property of a composite material. Then exploiting Tsai's Modulus the definition of master ply is given, as universal normalized [0] ply common for every composite material. Finally some literature examples of application of Tsai's Modulus in the world of composite materials are presented.

Chapter 5 gives some information about AVL, the vortex lattice software used to evaluate the aerodynamic loads used for the static sizing.

Chapter 6 provides a short overview on the wing CAD construction, using some reference imposed values as the surface area and the wing span.

In chapter 7 the construction of the FEM model and then the static sizing executed on that model are presented. There the mesh, materials, layups and boundary conditions definition are enunciated in detail. A paragraph regarding the definition of the aerodynamic loads using AVL is also present. Last, the results of the sizing are exposed, with all the modifications and all the main laminations imposed.

In chapter 8 a modal analysis extracting the first 20 natural frequencies is executed. Through this analysis the modal shapes that will then take part in the flutter analysis are deeply analysed. Then a comparison with some analytical modal results for a uniform cantilever beam and also with an equivalent FEM beam model are performed to prove the goodness of the FEM model implemented in the thesis.

The most significant modal frequencies found in the previous chapter are then used in Chapter 9 to perform a flutter analysis on the wing model. There all the settings imposed to perform the analysis, including the aerodynamic mesh, are deeply analyzed.

Finally, in Chapter 10 some parametric analysis are executed to investigate the aeroelastic response to the varying of the main spar position and Tsai's Modulus. The possible existence of a relationship between flutter and divergence speeds and Tsai's Modulus will be there deeply analyzed.

Chapter 2

Aeroelasticity theory

Aeroelasticity is an engineering study field concerning the interaction between aerodynamic loads applied on a deformable structure subject to inertial and damping effects. Thus, the free main fields involved in aeroelastic theories are:

1. Aerodynamics: loads applied on a body;
2. Elasticity: state of deformation of a body;
3. Dynamics: Inertia and damping of a body;

The interaction between these three subjects are well described by the Collar triangle (fig. 2.1).

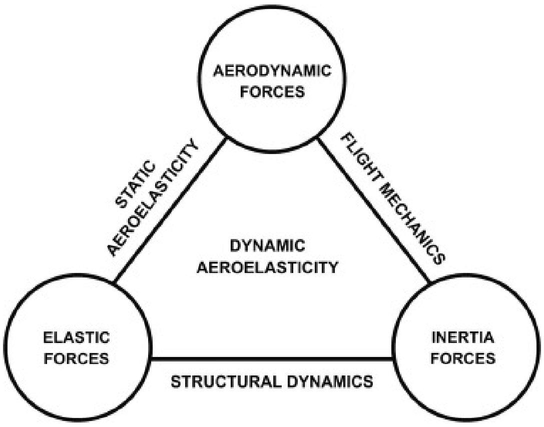
AERODYNAMIC FORCES
STATIC AEROELASTICITY
FLIGHT MECHANICS
DYNAMIC AEROELASTICITY
ELASTIC FORCES
INERTIA FORCES
STRUCTURAL DYNAMICS

Figure 2.1: Collar triangle [15]

Flight mechanics sees the plane as a rigid body and it is not interest of this analysis.

Static aeroelasticity analyses the effects of steady or quasi-steady aerodynamics loads on a deformable body, without accounting inertial and damping effects.

Structural dynamics studies the main vibration frequencies of a body and their respective deformation modes. These deformation modes, at certain frequencies, can interact with unstedy aerodynamics loads to give birth to some unstable configurations, as flutter. This possible unstable configurations are studied by means of dynamic aeroelasticty.

2.1 Structural dynamics

Structural dynamics are studied through modal analysis. Every structure with mass and inertia is characterized by a set of natural frequencies at which the structure vibrate with a corresponding modal shape. Technically, these set are composed by infinite natural frequencies, but only the lowest frequencies are aeroelastically important. Thus, in general, it is satisfactory to extract only the lowest ten natural frequencies and their relative modes. Normal modes analysis can be carried out both by computational methods (FEM) or by ground vibration testing (GVT). The former one is the method used during this thesis, as the analysis will be performed only on a computational basis. To find normal modes computationally a free vibration analysis can be executed (such as Nastran SOL 103). Essentially it investigates the equilibrium between elastic forces and inertial forces. Using the principle of virtual work (PVD) this equilibrium can be written as:

$$\delta W_{int} = \delta W_{ine} \tag{2.1}$$

Where:
W_{int}: internal work;
W_{ine}: inertial work.
The virtual variation of internal work can be expressed as:

$$\delta W_{int} = \int \delta \varepsilon^T \sigma \, dv \tag{2.2}$$

Using the FEM approximation, by assembling the stiffness matrix K, δW_{int} can be expressed as:

$$\delta W_{int} = \delta U^T K U \tag{2.3}$$

With:
U:displacements vector.
The virtual variation of inertial work can be expressed as:

$$\delta W_{ine} = \int \delta u \rho \ddot{u} \, dv \tag{2.4}$$

Where:
ρ: material density;
u: displacement;
$\ddot{u} = \frac{d^2u}{dt^2}$:acceleration.
Using the FEM approximation the variation of the inertial work can be written as:

$$\delta W_{ine} = \delta U^T M \ddot{U} \tag{2.5}$$

Substituting (2.3) and (2.5) in (2.2) the following equation is obtained:

$$M\ddot{U} + KU = 0 \tag{2.6}$$

The solution of this homogeneous problem must be searched through an eigenvalue problem. Considering an harmonic solution:

$$U = \overline{U}e^{i\omega t} \tag{2.7}$$

and its derivative:

$$\ddot{U} = -\omega^2\overline{U}e^{i\omega t} \tag{2.8}$$

the equation (2.6) can be rearranged as:

$$(-M\omega^2 + K)\overline{U} = 0 \tag{2.9}$$

Where:
$\overline{U}$: amplitude of the displacements;
ω: angular frequency.
By solving the characteristic polynomial it is easy to find the natural frequencies:

$$f = \frac{\omega}{2\pi} \tag{2.10}$$

Considering again equation (2.9) each frequency gives an eigenvector U, representing the respective modal shape, or normal mode.

This computational approach can be sufficient for a preliminary analysis and it is usually developed before executing ground vibration testing, to have an idea of the places subject to the major displacements. This particular spots are optimal to place some accelerometers that will gather data when the particular mode is externally excited by some electrical actuators or by moving lifting surfaces at the expected natural frequencies. In fact, most of GVT processes are based on preliminary information given by FEM analysis. GVT are used in order to get more accurate information about the natural frequencies, the modal shapes and also about damping properties of the real structure of a plane.

2.2 Static aeroelasticity

As it was said previously static aeroelasticity implies an analysis on a deformable body without taking in count of inertial and damping phenomena. This kind of analysis is good at predicting the divergence and commands inversion phenomena.

To simply understand what is the essence of static aeroelasticity the so called "typical section" (fig. 2.2), a 1 DOF system representative of a 2D airfoil, is considered. The airfoil is approximated by a flat plate mounted on a torsional spring. The spring is representative of the elastic line of the wing box. The degree of freedom is expressed by the elastic deformation angle θ:

$$\alpha = \alpha_R + \theta \tag{2.11}$$

With:
α: angle of attack of the airfoil;
α_R: angle of attack of the airfoil considered as a rigid body (fixed).
In this model the aerodynamic force, applied on the aerodynamic centre Q placed at 0.25%

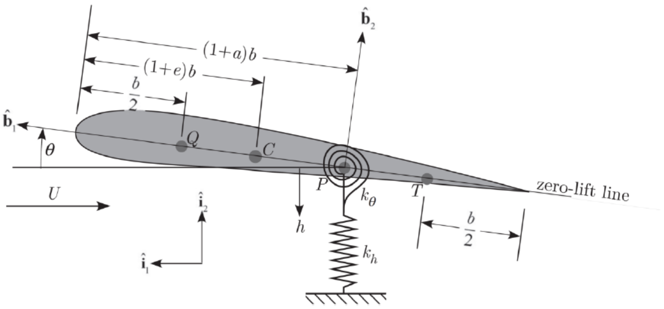

Figure 2.2: Typical section

of chord, is function of the deformation angle θ, as if the wing rotates rigidly around the elastic line placed in P:

$$L = \frac{1}{2}\rho V_\infty^2 S C_{L_\alpha} \alpha = \frac{1}{2}\rho V_\infty^2 S C_{L_\alpha}(\alpha_R + \theta) \tag{2.12}$$

With:
ρ: air density;
V_∞: air velocity relative to the airfoil;
S: wing aerea;
$C_{L_\alpha} = \frac{dC_L}{d\alpha}$;

Contrarily, the aerodynamic torque applied in Q is known to be constant with the angle of attack for moderate α and it is, therefor, neglected.
By imposing a static equilibrium around P a velocity for which the angle θ tends to infinity is found, the so called divergence velocity:

$$U_D = \sqrt{\frac{2K_\theta}{\rho S C_{L_\alpha}(\frac{1}{2} + a)b}} \tag{2.13}$$

With:
$b = c/2$;
a: aeroelastic parameter.

Therefor, this velocity corresponds to a condition of "infinite" elastic deformation, or, more realistically, a breaking condition for the wing.
Interesting it is to note that if the aerodynamic center is positioned downstream the elastic line divergence cannot occur.

2.3 Dynamic aeroelasticity

Dynamic aeroelasticity analyzes unsteady phenomena of fluid-structure interactions such as flutter.
Flutter is a phenomenon of dynamic instability caused by interactions between aerodynamic

loads and structure's natural modes.

During the last century various methods have been developed to predict this potentially destructive phenomenon, initially analytical, then, with the development of computational power, more and more flutter prediction codes have been published, with increasing accuracy.

2.3.1 Simplified flutter mechanics

Flutter, as said earlier, is an unstable configurations generated by unsteady aerodynamic loads that change due to the induced deformation of a wing. Since flutter depends on aerodynamic loads it usually emerges at moderate/high speeds, but flutter prediction are essential in aviation for every aircraft, as prescribed by EASA .

The unstable configurations starts when aerodynamic forces act near a resonance frequency of the wing, in a way that the work executed by the air on the wing increases in every load cycle. This happens when the structural damping relative to at least one normal mode is no more big enough to counteract aerodynamics loads. Aerodynamic loads can, therefor, be expressed as a fictitious damping that sums to the structural one. When the sum of the two factors is no more negative the flutter configuration is reached and oscillations amplifies exponentially. Towards flutter condition a torsional and a bending mode usually merges and the wing starts to deform in a torsional-flexural way.

This phenomenon can be visualized in all its fashion in a video realised by NASA in 1966 during a Piper PA-30 Twin Comanche tail flutter test, from which the following images are taken.

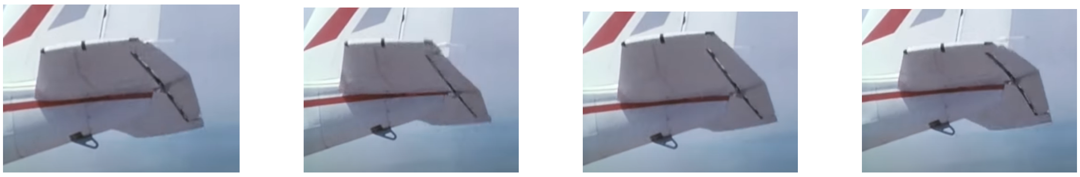

Figure 2.3: PA-30 Twin Comanche tail flutter test

Thus, the flutter problem can be expressed by the following homogeneous equation:

$$([M_s]-[M_a])\ddot{U}+([D_s]-[D_a])\dot{U}+([K_s]-[K_a])U=0 \tag{2.14}$$

with:

X_a: aerodynamic mass/damping/stiffness matrix;

X_s: structural mass/damping/stiffness matrix.

Usually $[M_s] >> [M_a]$ and $[D_a] >> [D_s]$, so equation (2.14) can be simplified as:

$$[M_s]\ddot{U}+(-[D_a])\dot{U}+([K_s]-[K_a])U=0 \tag{2.15}$$

The flutter condition is, therefor reached when $(-[D_a])$ is no more negative.

Aerodynamic damping is directly influenced by deformation levels of the wing and, consequently, by its stiffness. Thus, flutter can be fought by increasing material stiffness, or, as it will be seen, its Tsai's Modulus, by increasing wing box stiffness, and by introducing some flexural-torsional coupling in the material stiffness matrix. This can be done by not using quasi isotropic laminations. In this way, for example, when a wing is subject to pure bending loads it can deform in order to reduce its angle of attack, an excercise called aeroelastic tailoring.

An other way to influence aerodynamic damping is by modifying the wing geometry. In particular, it is good to have a centre of mass far from the elastic centre of the wing, to increase wing's inertia. In addition to this it is good to have the elastic line upstream the aerodynamic centre, or, if that is not possible, the nearest possible. In this way an increase in lift, by having a little arm or a negative arm, will induce respectively little torsional deformation or a negative torsional deformation and so, it will increase only by a small amount the angle of attack or it will decrease it.

A last way to counteract flutter is to introduce a positive swept angle in the wing configuration.

Finally, from equation (2.15) also the divergence phenomenon can be extracted, and it establish when $[K_a]$ became greater than $[K_s]$.

2.3.2 P-method with steady aerodynamics

The P-method is historically one of the first flutter calculation methods developed. It is based on a quasi-steady or steady aerodynamic model. In the case of steady aerodynamics lift is function solely of the elastic deformation angle θ:

$$L = L_I = \frac{1}{2}\rho V^2 S C_{L_\alpha}(\alpha_r + \theta) \tag{2.16}$$

On the contrary the aerodynamic torque results constant for low to moderate angles of attack and, therefor, it is usually not much important. Thus, with α_r constant, lift variation results to be function solely of structural torsional deformation and can be interpreted as an aerodynamic stiffness matrix to be add to at the structural stiffness matrix, obtaining the equation:

$$[M]\ddot{U} + ([K_s] - [K_a])U = 0 \tag{2.17}$$

In fact, if we consider again the typical section (fig. 2.2) with 2 DOFs, one rotational around P (θ) and one translational along the vertical direction (h), the displacement vector U is equal to:

$$U = \begin{Bmatrix} h \\ \theta \end{Bmatrix} \tag{2.18}$$

And so it is natural to represent aerodynamic loads as a stiffness matrix.

It is clear from equation (2.17) that structural damping has been neglected and aerodynamic damping does not appear due to the lift hypothesis.

Equation (2.17) is an eigenvalue problem and can be resolved by imposing an exponential solution:

$$U = \overline{U}e^{i\lambda t} \tag{2.19}$$

With:
$\lambda = \lambda_r + i\lambda_i$: complex eigenvalue.

P-method exploit these hypothesis, in fact it studies the stability of the system using the dimensionless eigenvalue "p":

$$p = \lambda \frac{b}{V} \tag{2.20}$$

with:
$b = c/2$: semichord;
V: air speed.
This method essentially studies the stability of the system by analyzing the change of eigenvalues values with speed, in particular the real part of p. In fact $Re(p)$ expresses the stability condition of the system. If $Re(p)$ become positive the system become unstable.

This method unfortunately provides good results only when the airfoil oscillates very slowly. If we introduce an other non dimensional eigenvalue, the reduced frequency, related to the angular frequency of the system:

$$k = \omega \frac{b}{V} = \lambda_i \frac{b}{V} \tag{2.21}$$

The condition of validity of this method can be expressed as:

$$k \to 0 \tag{2.22}$$

That means that also ω must tend to zero. This condition is too unrealistic for a typical flutter condition, where high amplitude oscillations can occur at high frequency.

2.3.3 P-method with quasi-steady aerodynamics

This method extends the aerodynamic theory exposed in the previous section by adding two quasi-steady extra terms related to vertical velocity and and deformation angular velocity:

$$L_{II} = \frac{1}{2}\rho V^2 S C_{L_\alpha} \alpha_{vs} = \frac{1}{2}\rho V S C_{L_\alpha} \dot{h} \tag{2.23}$$

With:
$\alpha_{vs} \simeq \frac{\dot{h}}{V}$: angle of attack due to wing vertical speed.

$$L_{III} = \frac{1}{2}\rho V^2 S C_{L_\alpha} \alpha_{rs} \tag{2.24}$$

Due to the rotation of the airfoil (fig. 2.2) around P, Q (aerodynamic centre) is subject to a vertical velocity $\dot{h}$ equal to:

$$\dot{h} = -b(\frac{1}{2} + a)\dot{\theta} \tag{2.25}$$

Now, developing L_{III} in the same way as L_{II} the third lift component is obtained as a function of $\dot{\theta}$

$$L_{III} = -\frac{1}{2}\rho V S C_{L_\alpha} b(\frac{1}{2}+a)\dot{\theta} \tag{2.26}$$

Finally the lift can be expressed as a sum of the three terms:

$$L = L_I + L_{II} + L_{III} = \frac{1}{2}\rho V S C_{L_\alpha}[V\theta + \dot{h} - b(\frac{1}{2}+a)\dot{\theta}] \tag{2.27}$$

Also in this case aerodynamic torque results constant for low to moderate angles of attack and, therefor, it is neglected in the analysis. Thus, with α_r constant, lift variation results to be function of structural torsional deformation θ, torsional angular velocity $\dot{\theta}$ and vertical velocity $\dot{h}$ (or flexural deformation velocity). The term $f(\theta)$ can be seen, as previously, as an aerodynamic stiffness matrix, whereas, the terms function of $\dot{h}$ and $\dot{\theta}$ can be seen as an aerodynamic damping matrix, obtaining the following equation:

$$[M_s]\ddot{U} + (-[D_a])\dot{U} + ([K_s] - [K_a])U = 0 \tag{2.28}$$

In fact, considering the 2 DOFs typical section (2.2), the displacements velocity vector is equal to:

$$\dot{U} = \begin{Bmatrix} \dot{h} \\ \dot{\theta} \end{Bmatrix} \tag{2.29}$$

Since in general $[D_a] >> [D_s]$ the latter is neglected. The problem (2.28) can be solved in the usual way by imposing an exponential solution and studying the eigenvalue stability with air speed. In this equation a damping term appears, so now $Re(p)$ can assume also negative values. Flutter condition is, therefor, reached when $Re(p)$ is no more negative. In fact, as a typical mass-spring-dumper system, with the variation of $Re(p)$ different behaviours are obtained:

- $Re(p) << 0$: strongly dumped solution;
- $Re(p) < 0$: dumped oscillating solution;
- $Re(p) = 0$: harmonic solution;
- $Re(p) > 0$: amplified oscillating solution;
- $Re(p) >> 0$: strongly amplified solution.

P-method with quasi-steady aerodynamics gives a bit more accurate results than with steady aerodynamics, but its validity field remains too low, as it also requires that the reduced frequency

$$k \to 0 \tag{2.30}$$

In fact, the big flaw of this method is that it is not able to taking in count of the delay in lift generation in respect to the perturbations. This delay can be neglected only if the wing oscillates very slowly.

Some more complex form of p-method have been developed to be able to analyze also unsteady aerodynamics cases, such as the one developed by Mazelsky and O'Connel which accounts for apparent mass, aerodynamic lag and aerodynamic coupling between different strips on the wing (Hassig, 1971 [16]).

2.3.4 p-k method

p-k method allows to take in count phase differences between disturbances ($\theta, \dot{h}, \dot{\theta}$) and generation of lift. This can be done by using more complex aerodynamics models, such as Theodorsen or DLM (doublet lattice method). These aerodynamic methods gives results only for harmonic oscillations. This introduces a discrepancy in the model because post-flutter or pre-flutter conditions imply an amplification or damping in oscillations, whereas these aerodynamic methods can only represent harmonic oscillations. As explained by Hassig [16] the rationale for this approach is that for sinusoidal motions with slowly increasing or decreasing amplitude aerodynamics based on constant amplitude are a good approximation. So near flutter conditions can be well represented.

In this model aerodynamic loads are function of the reduced frequency:

$$k = \omega \frac{b}{V} \tag{2.31}$$

k allows to account for phase differences between disturbances and effective angle of attack.

To simply understand how the method works, the 2 DOFs typical section (fig. 2.2) is again considered, using Theodorsen aerodynamics.

Effective angle of attack evaluated at 3/4 of chord can be expressed as:

$$\alpha_{eff} = C(k)[\theta + \frac{\dot{h}}{V} + \frac{b}{V}(\frac{1}{2} - a)\dot{\theta}] \tag{2.32}$$

$C(k)$ is the Theodorsen function and it is a complex function:

$$C(k) = F(k) + iG(k) \tag{2.33}$$

Essentially the deformation angle is multiplied for a complex function in order to take in count the delay in the generation of lift due to the non immediate change in circuitation value. Phase difference can be expressed by:

$$\phi = \arctan(\frac{G(k)}{F(k)}) \tag{2.34}$$

Now, if the aeroelastic problem is solved as an eigenvalue problem imposing an exponential solution the characteristic polynomial will result as function of the eigenvalue p, similarly to the p-method. However, the coefficients of the polynomial terms result to be function of the reduced frequency k, whose value is not known. The i-th eigenvalue p is in turn function of k, in fact:

$$p_i = p_{i_r} + ik_i \tag{2.35}$$

To solve the problem an iterative method is required. To find the roots of the characteristic polynomial

$$A(k)+B(k)p+D(k)p^2+...+N(k)p^n=0 \tag{2.36}$$

it is necessary to impose a guess value k_{guess}. With this guess value a first value for the p vector is found:

$$p_1 = p_{1_r} \pm ik_1 \tag{2.37}$$

The k_1 value just found will differ from k_{guess} and will be used in the second iteration cycle. After recalculating the aerodynamic terms the roots of the characteristic polynomial are found again using k_1, obtaining:

$$p_2 = p_{2_r} \pm ik_2 \tag{2.38}$$

This iteration cycle continues until convergence is reached. This process is repeated for every speed incremental.

p-k method, using more complex aerodynamic theories such as DLM is able to predict pretty accurately the flutter velocity and it is still one of the most used methods for subsonic flutter prediction. CFD based codes have also been developed, but require much higher computational costs.

2.4 Aerodynamic models

To evaluate accurately aerodynamic loads some computational methods are required. Since in subsonic aeroelasticity the interest is to evaluate Lift and Lift variations, also in strong unsteady regimes, the most suited methods are potential based methods and, in particular, VLM (vortex lattice methods) and DLM (doublet lattice methods), as Navier-Stokes based CFD codes would still be too computationally expensive for the present work. These methods are based on Prandtl lifting line theory and consequently viscosity effects are neglected. VLM works better with quasi-steady aerodynamics and it is best suited for divergence evaluation, whereas DLM represents very well harmonic aerodynamic phenomena, and it gives good results for flutter analysis. Both methods represent the wing as an infinite thin surface divided into a finite lattice of quadrangular elements, called panels. Lifting properties are respectively represented through vortex or doublets placed on the panels.

2.4.1 Vortex Lattice Method (VLM)

In VLM on each panel is placed a horseshoe element that consists of a straight bound vortex segment and two semi-infinite vortex lines (fig. 2.4). On the bound vortex, placed at the first quarter of chord, is concentrated the vorticity that models the lifting properties. The trailing vortex lines extend to infinity and model the wake. At infinity the vorticity lines close the circuit (fig. 2.4) in order to obtain a total vorticity value equal to zero. This closure is needed to respect the Helmholtz theory, which states that the vorticity flow through every fundamental surface that move with the fluid is constant respect to time, or mathematically:

$$\frac{D}{Dt}(\omega \cdot n d\sigma) = 0 \tag{2.39}$$

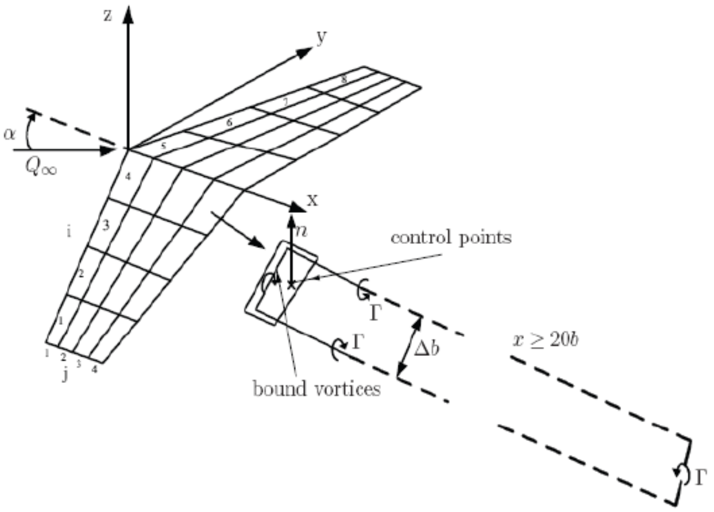

Figure 2.4: VLM horseshoe element [17]

However this closure vortex, or starting vortex to be more precise, is so far downstream that it does not influence wing lifting properties [18]. Thus the vorticity system of the wing and its wake is represented by N horseshoe vortex of intensity Γ_i.

To find the value of induced velocity on the panel i induced by the sending vortices of the sending panel j wall tangency condition (WTC) must be imposed for all panels. This condition must be imposed in the mid point of 3/4 chord line, called control point. In this way Kutta condition is automatically satisfied.

Considering the assumption that the freestream velocity is directed along $+x$ (fig. 2.5), for the panel i the wall tangency condition on the receiving panel is:

$$V_j^{i^T} = [(V_\infty + u'_i)i + v'_i j + w'_i k] \cdot n_i = 0 \tag{2.40}$$

Where n is the panel normal and u', v', w' are the induced velocity by the j-th panel on the i-th, respectively in direction x, y, z. Considering small wing deflection the products $u'_i \cdot n_i$ and $v'_i \cdot n_i$ are negligible and the WTC equation simplifies as:

$$V_\infty \sin\alpha^i + w'_i \cos\alpha^i = 0 \tag{2.41}$$

Considering the displacement along the z axis of the control point, since:

$$\tan\alpha^i = -\frac{\partial Z_i}{\partial x} \tag{2.42}$$

WTC can be rewritten as:

$$V_\infty \frac{\partial Z_i}{\partial x} = w'_i \tag{2.43}$$

Or, if normalized normalwash ($w_i = w'_i / V_\infty$) is considered:

$$\frac{\partial Z_i}{\partial x} = w_i \tag{2.44}$$

This relation is very important because it links the normlwash acting on the panel with the deformation of the panel itself.

The dimensionless normalwash w_i on a generic panel can be expressed also as a function of dimensionless pressure differences Δp_j acting on every j-th panel as:

$$w_i = \sum_{j=1}^{N_{AP}} A_{ij}^{D} \cdot \Delta p_j \tag{2.45}$$

Or, in a matricial form:

$$\{w\} = [A^D] \cdot \{\Delta p\} \tag{2.46}$$

$[A^D]$ is the Aerodynamic Influence Coefficient Matrix for the aerodynamic panels. It depends on geometrical quantities, in fact, the input data consists of the vertices' coordinates of the horseshoes, the coordinates of control points, the chords and the normal vectors of each panel. Essentially it only depends on the aerodynamic discretization. $[A^D]$ has dimension equal to $N_{AP} \times N_{AP}$, whereas $\{w\}$ and $\{\Delta p\}$ are vectors of dimension $N_{AP} \times 1$, with N_{AP} number of aerodynamic panels. Δp is the dimensionless pressure differential:

$$\Delta p = \frac{\Delta P}{\frac{1}{2}\rho_\infty V_\infty^2} \tag{2.47}$$

2.4.2 Doublet Lattice Method (DLM)

The DLM is based on the same assumptions of potential flow as VLM, with an analogous discretization, but, instead of a vortex, a doublet horseshoe is used. Thus the DLM solves the acceleration potential equations using an harmonic approach [19]. If dimensionless normalwash and dimensionless pressure jump are considered:

$$w = \frac{w'}{V_\infty} \qquad\qquad \Delta p = \frac{\Delta P}{\frac{1}{2}\rho_\infty V_\infty^2} \tag{2.48}$$

Considering harmonic motion w' and Δp can be expressed in the exponential form:

$$w = \overline{w} e^{i\omega t} \qquad\qquad \Delta p = \overline{\Delta p} e^{i\omega t} \tag{2.49}$$

The normalwash $\overline{w}$ in a point with coordinates x, y is related to the pulsating pressure jump Δp in the point with coordinates ξ, η by the following expression [3]:

$$\overline{w} = \frac{1}{8\pi} \int_A \overline{\Delta p}\, K(x_0, y_0, \omega, M)\, dA \tag{2.50}$$

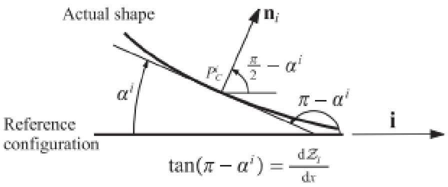

Figure 2.5: Reference configuration

This a surface integral to be executed on every aerodynamic panel, where:
M is the freestream Mach number;

$$x_0 = x - \xi \qquad y_0 = y - \eta; \tag{2.51}$$

and the Kernel function K can be written as:

$$K = e^{-\frac{i\omega x_0}{V_\infty}} \frac{K_1 T_1}{r^2} \tag{2.52}$$

With:

$$\begin{aligned} r &= (y_0^2)^{\frac{1}{2}} & T_1 &= 1 \\ K_1 &= I_1 + \frac{M\, r}{R} \frac{e^{-ik_1 u_1}}{(1+u_1^2)^{\frac{1}{2}}} \\ I_1 &= \int_{u_1}^{\infty} \frac{e^{-ik_1 u_1}}{(1+u_1^2)^{\frac{3}{2}}} du \\ u_1 &= \frac{MR - x_0}{\beta^2 r} & k_1 &= \frac{\omega\, r}{V_\infty} \\ R &= (x_0^2 + \beta^2 r^2)^{\frac{1}{2}} & \beta &= (1-M^2)^{\frac{1}{2}} \end{aligned} \tag{2.53}$$

From normalized normalwash $\overline{w}$ pressure differentials Δp can be computed using an Aerodynamic Influence Matrix, similarly to VLM:

$$\overline{w} = \sum_{j=1}^{N_{AP}} A_{ij}^{D} \overline{\Delta p_j} \tag{2.54}$$

A_{ij} depends on the geometry of the wing and on the aerodynamic discretization as in VLM. For DLM a good expression for A_{ij}^D is given by:

$$A_{ij}^D = \frac{\Delta x_j}{8\pi} \int_{-bj}^{+bj} K_{ij}\, dy_j \tag{2.55}$$

The presence of the Kernel function means that nearer panels have a stronger influence on each other than farther panels.

2.4.3 VLM and DLM application in aeroelastic analysis

The pressure differentials are the final result of the aerodynamic analysis. They are calculated relying on modal shapes form given by a structural FEM model. Displacements of the FEM nodes are passed to the control point (the point placed at 3/4 of chord) of the aerodynamic mesh through a spline interpolation. Then, thanks to equation 2.44, by differentiating vertical displacements along the longitudinal direction, the normalized normalwash w_i is found. Knowing the Aerodynamic Influence Coefficient Matrix, with equation 2.46 is now easy to find the value of normalized pressure differentials Δp with some numerical methods. By integrating the pressure value on every aerodynamic panel surface the lift applied at the load points (the point placed at 1/4 chord) is calculated. By transferring the load back again to the

FEM model with a spline interpolation it is possible to compute the aeroelastic stiffness and damping matrices or to apply a flutter calculation method such as the p-k method.

2.5 Aeroelastic equations of motion

Now that all components of aeroelasticity has been enunciated the aeroelastic equation in time-domain can be expressed as [20]:

$$M\ddot{u}(t)+C\dot{u}(t)+Ku(t)=F(t) \tag{2.56}$$

With:
M: mass matrix;
C: structural damping matrix;
K: stiffness matrix;
F: force vector;
u: displacements vector.

The solution, in Laplace domain, of the aeroelastic problem will have the following oscillating form:

$$u(t)=\hat{u}e^{st}=\hat{u}e^{(\sigma+i\omega)t} \tag{2.57}$$

Introducing the aerodynamic term:

$$[Ms^2+Cs+K-\frac{1}{2}\rho V^2Q(s)]\hat{u}(s)=0 \tag{2.58}$$

The non-dimensional p eigenvalue can now be introduced:

$$p=\frac{b}{V_\infty}s=\frac{b}{V_\infty}(\sigma+i\omega)=g+ik \tag{2.59}$$

Where b is the reference length, usually half chord length. k is the reduced frequency and it is the imaginary part of p.
Substituting p into (2.58):

$$\left[(\frac{V_\infty}{b})^2Mp^2+\frac{V_\infty}{b}Cp+K-\frac{1}{2}\rho V^2Q(p)\right]\hat{u}(p)=0 \tag{2.60}$$

2.5.1 Modal approach and generalized matrices

To deal with a computationally cheap problem the modal approach can be used. Usually only the lower modes play a role in flutter occurrence. Typically the first ten modes are enough to describe the structural deformation of flutter. The displacements vector can be written using the modal superposition and the unknown modal amplitudes vector q:

$$u=\phi q \tag{2.61}$$

ϕ is a matrix where a number of modal shapes N_{modes} are contained.
The generalized aerodynamic matrix for a given reduced frequency is given by:

$$\tilde{Q}_{ij}(ik) = \sum_{N=1}^{N_{AP}} \Delta p_j^N(ik)\tilde{Z}_i^N S_{AP}^N \tag{2.62}$$

Where:
$\delta p_j^N(ik)$ is the pressure jump due to the j-th set of motions acting on the N-th aerodynamic panel. It is computed by means of DLM;
$\tilde{Z}_i^N$ is the i-th transversal motion set evaluated at the N-th aerodynamic panel. Starting from the i-th modal shape given by a structural code, the i-th motion set is then mapped on the aerodynamic mesh by means of splining process;
S_{AP}^N is the area of the N-th aerodynamic panel.
$Q_{ij}(ik)$ is, therefor, a square matrix with $N_{modes} \times N_{modes}$ elements.

The generalized mass matrix is given by:

$$\tilde{M} = \phi^T M \phi \tag{2.63}$$

$\tilde{M}$ is a square diagonal matrix with $N_{modes} \times N_{modes}$ elements.

The generalized stiffness matrix is a square diagonal matrix with $N_{modes} \times N_{modes}$, whose diagonal terms are:

$$\tilde{K}_{ij} = \omega_i^2 \tilde{M}_{ij} \tag{2.64}$$

Where ω_{ij} is the oscillatory frequency associated to the i-th modal shape.

The aeroelastic equation, neglecting the damping term[1], becomes:

$$\Big[(\frac{V_\infty}{b})^2 \tilde{M} p^2 + \tilde{K} - \frac{1}{2}\rho V^2 \tilde{Q}(p)\Big] q(p) = 0 \tag{2.65}$$

The use of the generalized matrices allows to reduce the problem's dimensions, that decrease from $N_{DOF} \times N_{DOF}$ using the regular matrices to $N_{modes} \times N_{modes}$ using the generalized matrices.

If to solve (2.65) is chosen the p-k method, Q is obtained from simple harmonic motion:

$$\Big[(\frac{V_\infty}{b})^2 \tilde{M} p^2 + \tilde{K} - \frac{1}{2}\rho V^2 \tilde{Q}(ik)\Big] q(p) = 0 \tag{2.66}$$

This formulation, as explained in section 2.3.4, is mathematically inconsistent because p was assumed as dumped sinusoidal motion. Despite this approximation this method usually provides good results.

---

[1] Usually structural damping is much smaller than aerodynamic damping, so it can be neglected

Chapter 3

FEM theory

Finite element method is a tool to evaluate the approximate solution to boundary conditions problems for partial differential equations. Fem utilizes a discretization of the domain in a finite number of elements and variational methods to rewrite equations in terms of simple algebraic equations.

Finite elements models are today's state of the art for aeroelastic calculations since, as seen in section 2.5, stiffness matrix and mass matrix must be known to perform an aeroelastic analysis. Therefor, an introduction to how FEM works is presented here in this chapter. Since a 2D elements model will be realized during the thesis particular attention will be put to plate elements. Thus, the stiffness matrix and the mass matrix will be evaluated for a Reissner-Mindlin plate element.

3.1 Reissner-Mindlin theory

The first step needed to compute a 2D FEM model is to approximate a 3D displacement field with a 2D field. Usually 2D FEM codes are based on Reissner-Mindlin (R-M) theory. This theory is based on two hypothesis on the displacements field:

- the displacements field is linear;
- plate thickness is constant ($\varepsilon_{zz} = 0$).

From these hypothesis the following displacement field is found:

$$\begin{cases} u(x,y,z) = u^0(x,y) + z\ \phi_x(x,y) \\ v(x,y,z) = v^0(x,y) + z\ \phi_y(x,y) \\ w(x,y,z) = w^0(x,y) \end{cases} \tag{3.1}$$

Through these hypothesis the field on the plate volume is determined by the displacements field on a reference surface on the plate, which usually correspond to the mean surface of the plate. Therefor, the 3D problem has been rewritten as a 2D problem. The unknowns are now the displacements (u^0, v^0, w^0) and the rotations (ϕ_x, ϕ_y) of the reference surface (apex "0"):

$$\{s^0\}^T = \{u^0\ v^0\ w^0\ \phi_x\ \phi_y\} \tag{3.2}$$

The vector $\{s^0\}$ regards a plane domain and no more a volume.

To write the R-M transformation in a contracted form let consider a matrix [R] such that:

$$\{s\} = [R]\{s^0\} \tag{3.3}$$

With:

$$\Big[R\Big] = \begin{bmatrix} 1 & 0 & 0 & z & 0 \\ 0 & 1 & 0 & 0 & z \\ 0 & 0 & 1 & 0 & 0 \end{bmatrix} \tag{3.4}$$

3.2 Finite element "Reissner-Mindlin plate"

The R-M plate theory just evaluated can now be exploited to find the expression for the plate finite element.

Since displacements field is linear, deformations $\{\varepsilon\}^T$ can be expressed as[1] :

$$\begin{cases} \varepsilon_{xx} = u_{,x} \\ \varepsilon_{yy} = v_{,y} \\ \varepsilon_{xy} = u_{,y} + v_{,x} \\ \varepsilon_{xz} = u_{,z} + w_{,x} \\ \varepsilon_{yz} = v_{,z} + w_{,y} \end{cases} \tag{3.5}$$

Or in compact form as:

$$\{\varepsilon\} = [b][s] \tag{3.6}$$

Where:

$$\Big[b\Big] = \begin{bmatrix} \frac{\partial}{\partial x} & 0 & 0 \\ 0 & \frac{\partial}{\partial y} & 0 \\ \frac{\partial}{\partial y} & \frac{\partial}{\partial x} & 0 \\ \frac{\partial}{\partial z} & 0 & \frac{\partial}{\partial x} \\ 0 & \frac{\partial}{\partial z} & \frac{\partial}{\partial y} \end{bmatrix} \tag{3.7}$$

If R-M hypothesis are inserted in (3.5) and derivatives are executed, the following expressions are obtained:

$$\begin{cases} \varepsilon_{xx} = u^0{}_{,x} + z\ \phi_{x,x} \\ \varepsilon_{yy} = v^0{}_{,y} + z\ \phi_{y,y} \\ \varepsilon_{xy} = u^0{}_{,y} + v^0{}_{,x} + z\ (\phi_{x,y} + \phi_{y,x}) \\ \varepsilon_{xz} = \phi_x + w_{,x} \\ \varepsilon_{yz} = \phi_y + w_{,y} \end{cases} \tag{3.8}$$

---

[1] ,x stands for $\frac{\partial}{\partial x}$

Or in contracted form:

$$\{\varepsilon\} = [b^0][s^0] \tag{3.9}$$

With:

$$[b^0] = [b^{00}] + z[b^{0z}] \tag{3.10}$$

Where:

$$\left[b^{00}\right] = \begin{bmatrix} \frac{\partial}{\partial x} & 0 & 0 & 0 & 0 \\ 0 & \frac{\partial}{\partial y} & 0 & 0 & 0 \\ \frac{\partial}{\partial y} & \frac{\partial}{\partial x} & 0 & 0 & 0 \\ 0 & 0 & \frac{\partial}{\partial x} & 1 & 0 \\ 0 & 0 & \frac{\partial}{\partial y} & 0 & 1 \end{bmatrix} \tag{3.11}$$

and

$$\left[b^{0z}\right] = \begin{bmatrix} 0 & 0 & 0 & \frac{\partial}{\partial x} & 0 \\ 0 & 0 & 0 & 0 & \frac{\partial}{\partial y} \\ 0 & 0 & 0 & \frac{\partial}{\partial y} & \frac{\partial}{\partial x} \\ 0 & 0 & 0 & 0 & 0 \\ 0 & 0 & 0 & 0 & 0 \end{bmatrix} \tag{3.12}$$

To arrive at the finite element formulation now unknowns $\{s^0\}$ must be express in function of nodal displacements $\{S\}$. The relationship that can be exploited is the following:

$$\{s^0\} = [N]\{S\} \tag{3.13}$$

Where nodal displacements are grouped (for a quad element) as:

$$\{S\}^T = \{\{S_1\}^T,\ \{S_2\}^T,\ \{S_3\}^T,\ \{S_4\}^T\} \tag{3.14}$$

With:

$$\{S_i\} = \{U_i, V_i, W_i, \phi_{xi}, \phi_{yi}\} \tag{3.15}$$

$[N]$ is the shape functions matrix. N_i are essentially interpolation functions, such as Lagrange polynomials, that execute a sort of geometrically weighted average of the values of the variables in the element nodes:

$$u^0(x,y) = \sum_{i=1}^{N\ nodi} N_i(x,y)U_i \tag{3.16}$$

$$v^0(x,y) = \sum_{i=1}^{N\ nodi} N_i(x,y)V_i \tag{3.17}$$

$$w^0(x,y) = \sum_{i=1}^{N\ nodi} N_i(x,y)W_i \tag{3.18}$$

$$\phi_x(x,y) = \sum_{i=1}^{N\ nodi} N_i(x,y)\Phi_{xi} \tag{3.19}$$

$$\phi_y(x,y) = \sum_{i=1}^{N\ nodi} N_i(x,y)\Phi_{yi} \tag{3.20}$$

Now the matrix of interpolation of deformation [B] can be obtained, which relates deformations to nodal displacements:

$$\{\varepsilon\} = [B]\{S\} \tag{3.21}$$

But, from (3.13) and (3.9), it is clear that the following relationship is valid:

$$\{\varepsilon\} = [b^0][N]\{S\} \tag{3.22}$$

Therefor:

$$[B] = [b^0][N] \tag{3.23}$$

That is equal to:

$$[B] = ([b^{00}] + z[b^{01}])[N] \tag{3.24}$$

And, posing:

$$[B^0] = [b^{00}][N] \tag{3.25}$$

$$[B^1] = [b^{01}][N] \tag{3.26}$$

It is obtained that:

$$[B] = [B^0] + z[B^1] \tag{3.27}$$

3.2.1 Evaluation of stiffness matrix

To evaluate the stiffness matrix of the element now it is necessary to exploit the definition of virtual internal work, and substitute inside the definition the relationship just evaluated:

$$\delta W_i = \int_V \{\sigma\}^T \{\delta\varepsilon\}\, dV \tag{3.28}$$

From Hooke's law is then known that:

$$\{\sigma\} = [Q^K]\{\varepsilon\} \tag{3.29}$$

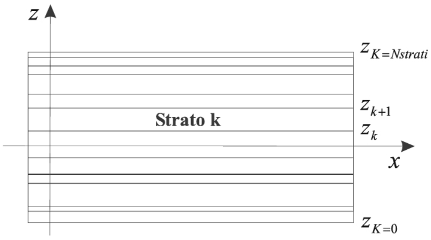

Figure 3.1: Laminated plate

Therefor:

$$\delta W_i = \int_V \{\varepsilon\}^T [Q^k] \{\delta\varepsilon\}\, dV \tag{3.30}$$

Substituting 3.21 inside:

$$\delta W_i = \{\delta S\} \int_V [B]^T [Q^k][B]\, dV\ \{S\}^T \tag{3.31}$$

That can be rewritten in turn, by putting inside (3.27), as:

$$\delta W_i = \{\delta S\} \int_V ([B^0] + z[B^1])^T [Q^k]([B^0] + z[B^1])\, dV\ \{S\}^T \tag{3.32}$$

From which the stiffness matrix [K] is evaluated:

$$[K] = \int_V ([B^0] + z[B^1])^T [Q^k]([B^0] + z[B^1])\, dV \tag{3.33}$$

If a composite laminate plate is considered the volume integral can be rewritten as:

$$\int_V dV = \int_{-h/2}^{+h/2} dz \int_\Omega d\Omega = \sum_{k=0}^{N\ layers} \int_{z_k}^{z_{k+1}} dz \int_\Omega d\Omega \tag{3.34}$$

Where, referring to figure 3.1:
h is the total plate thickness;
Ω is the reference surface;
k is the layer number.

And, consequently, stiffness matrix can be rewritten as:

$$[K] = \sum_{k=0}^{N\ layers} \int_{z_k}^{z_{k+1}} dz \int_\Omega ([B^0] + z[B^1])^T [Q^k]([B^0] + z[B^1])\, d\Omega \tag{3.35}$$

[K] can be conveniently developed as:

$$[K] = \sum_{k=0}^{N\ layers} \int_{z_k}^{z_{k+1}} dz \int_\Omega ([B^0]^T [Q^k][B^0] + [B^0]^T z[Q]^k[B^1] + [B^1]^T z[Q^k][B^0] + [B^1]^T z^2 [Q^k][B^1])\, d\Omega \tag{3.36}$$

Then variables that are function solely of z are integrated along z and are named as:

$$[A] = \sum_{k=0}^{N\ layers} \int_{z_k}^{z_{k+1}} [Q^k]\ dz \tag{3.37}$$

$$[B] = \sum_{k=0}^{N\ layers} \int_{z_k}^{z_{k+1}} z[Q^k]\ dz \tag{3.38}$$

$$[C] = \sum_{k=0}^{N\ layers} \int_{z_k}^{z_{k+1}} z^2[Q^k]\ dz \tag{3.39}$$

$[A]$: membrane stiffness matrix;
$[B]$: coupling stiffness matrix;
$[D]$: bending-torsional stiffness matrix.
$[K]$ can now be rewritten as:

$$[K] = \int_\Omega ([B^0]^T[A][B^0] + [B^0]^T[B][B^1] + [B^1]^T[B][B^0] + [B^1]^T[D][B^1])\ d\Omega \tag{3.40}$$

From which:

$$[K] = [K^{00}] + [K^{01}] + [K^{10}] + [K^{11}] \tag{3.41}$$

With:

$$[K^{00}] = \int_\Omega [B^0]^T[A][B^0]\ d\Omega \tag{3.42}$$

$$[K^{01}] = \int_\Omega [B^0]^T[B][B^1]\ d\Omega \tag{3.43}$$

$$[K^{10}] = \int_\Omega [B^1]^T[B][B^0]\ d\Omega \tag{3.44}$$

$$[K^{11}] = \int_\Omega [B^1]^T[D][B^1]\ d\Omega \tag{3.45}$$

Evaluate the stiffness matrix of the R-M plate is equal to evaluate stiffness matrices $[K^{00}], [K^{01}], [K^{10}], [K^{11}]$.

3.2.2 Evaluation of mass matrix

Evaluation of mass matrix is needed to compute modal analysis and flutter analysis. To evaluate it let start by writing the virtual variation of the inertial work[2]:

$$\delta W_{iner} = \int_V \{\delta s\}^T \rho \{\ddot{s}\}\ dV \tag{3.46}$$

Considering homogeneous plates it can be defined a mass per unit of surface as:

$$m = \int_{-h/2}^{+h/2} \rho\ dz \tag{3.47}$$

And rewriting the virtual variation of inertial work:

$$\delta W_{iner} = \int_\Omega \{\delta s\}^T m \{\ddot{s}\}\ d\Omega \tag{3.48}$$

---

[2] $\ddot{s}$ stands for $\frac{d^2s}{dt^2}$

From section 3.1 it is known that:

$$\{s\} = [R]\{s^0\} \tag{3.49}$$

and from section 3.2 that:

$$\{s^0\} = [N]\{S\} \tag{3.50}$$

Therefor the variation of virtual inertial work can be rewritten as:

$$\delta W_{iner} = \{\delta S\}^T \int_\Omega [N]^T [R]^T m[R][N] \, d\Omega \, \{\ddot{S}\} \tag{3.51}$$

From which the mass matrix can be extracted:

$$[M] = \int_\Omega [N]^T [R]^T m[R][N] \, d\Omega \tag{3.52}$$

Chapter 4

Tsai's Modulus

4.1 What is Tsai's Modulus

Carbon fiber reinforced composites are widely used in aeronautics due to their unique properties, such as high strength and modulus to weight ratio. In 2014 Tsai and Melo [6] proposed a novel invariant-based approach to describe elastic properties of composites plies and laminates. In this approach the trace of the plane stress stiffness matrix is evaluated as a material property.
Considering classical lamination theory (CLT), for a unidirectional tape the the on-axis stress–strain relations, using engineering notation, are:

$$\begin{Bmatrix} \sigma_x \\ \sigma_y \\ \sigma_s \end{Bmatrix} = \begin{bmatrix} Q_{xx} & Q_{xy} & 0 \\ Q_{yx} & Q_{yy} & 0 \\ 0 & 0 & Q_{ss} \end{bmatrix} \begin{Bmatrix} \varepsilon_x \\ \varepsilon_y \\ \varepsilon_s \end{Bmatrix} \tag{4.1}$$

and

$$\begin{Bmatrix} \varepsilon_x \\ \varepsilon_y \\ \varepsilon_s \end{Bmatrix} = \begin{bmatrix} S_{xx} & S_{xy} & 0 \\ S_{yx} & S_{yy} & 0 \\ 0 & 0 & S_{ss} \end{bmatrix} \begin{Bmatrix} \sigma_x \\ \sigma_y \\ \sigma_s \end{Bmatrix} \tag{4.2}$$

where σ_i and ε_i are the stress and strain components, respectively, and [Q] and [S] are the in plain stress stiffness and compliance.

In engineering notation stiffness and compliance are not tensors. Rewriting 4.4 and 4.3 in tensorial notation the following relations are valid:

$$\begin{Bmatrix} \sigma_x \\ \sigma_y \\ \sigma_s \end{Bmatrix} = \begin{bmatrix} Q_{xx} & Q_{xy} & 0 \\ Q_{yx} & Q_{yy} & 0 \\ 0 & 0 & 2Q_{ss} \end{bmatrix} \begin{Bmatrix} \varepsilon_x \\ \varepsilon_y \\ \varepsilon_s/2 \end{Bmatrix} \tag{4.3}$$

and

$$\begin{Bmatrix} \varepsilon_x \\ \varepsilon_y \\ \varepsilon_s/2 \end{Bmatrix} = \begin{bmatrix} S_{xx} & S_{xy} & 0 \\ S_{yx} & S_{yy} & 0 \\ 0 & 0 & S_{ss}/2 \end{bmatrix} \begin{Bmatrix} \sigma_x \\ \sigma_y \\ \sigma_s \end{Bmatrix} \tag{4.4}$$

Now, if a rotation around the reference axis is introduced 4.1, stress, strains, and consequently the stiffness matrix will modify as a function of the rotation angle θ. We will consider a positive rotation in the anti – clockwise direction.

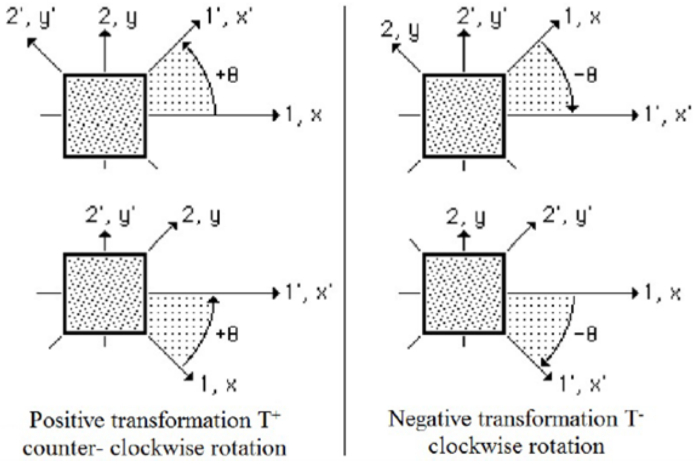

Positive transformation T^+
counter- clockwise rotation

Negative transformation T^-
clockwise rotation

Figure 4.1: Rotation of master ply along reference axis [21]

Due to the rotation stress and strains components will change as it follows:

$$\left\{\sigma'\right\} = \left[J\right]\left\{\sigma\right\} \tag{4.5}$$

$$\left\{\varepsilon'\right\} = \left[J^T\right]^{-1}\left\{\varepsilon\right\} \tag{4.6}$$

where

$$\left[J\right] = \begin{bmatrix} m^2 & n^2 & 2mn \\ n^2 & m^2 & -2mn \\ -mn & mn & m^2-n^2 \end{bmatrix} \tag{4.7}$$

and

$$\left[J^T\right]^{-1} = \begin{bmatrix} m^2 & n^2 & mn \\ n^2 & m^2 & mn \\ -2mn & 2mn & m^2-n^2 \end{bmatrix} \tag{4.8}$$

with

$$m = cos\theta \tag{4.9}$$

$$n = sin\theta \tag{4.10}$$

Note that 4.7 and 4.8 differ because engineering shear strain is used.

Now, if the off axis Hooke relation is written:

$$\begin{Bmatrix} \sigma_1 \\ \sigma_2 \\ \sigma_6 \end{Bmatrix} = \begin{bmatrix} Q_{11} & Q_{12} & Q_{16} \\ Q_{12} & Q_{22} & Q_{26} \\ Q_{61} & Q_{62} & Q_{66} \end{bmatrix} \begin{Bmatrix} \varepsilon_x \\ \varepsilon_y \\ \varepsilon_s \end{Bmatrix} \tag{4.11}$$

Between on – axis and off – axis stiffness matrix is valid the following relation:

$$[Q'] = [J][Q][J^T] \tag{4.12}$$

The transformation relations lead to the following matrix:

$$\begin{Bmatrix} Q_{11} \\ Q_{22} \\ Q_{12} \\ Q_{66} \\ Q_{16} \\ Q_{26} \end{Bmatrix} = \begin{bmatrix} m^4 & n^4 & 2m^2n^2 & 4m^2n^2 \\ n^4 & m^4 & 2m^2n^2 & 4m^2n^2 \\ m^2n^2 & m^2n^2 & m^4+n^4 & -4m^2n^2 \\ m^2n^2 & m^2n^2 & -2m^2n^2 & (m^2-n^2)^2 \\ m^3n & -mn^3 & mn^3-m^3n & 2(mn^3-m^3n) \\ mn^3 & -m^3n & m^3n-mn^3 & 2(m^3n-mn^3) \end{bmatrix} \begin{Bmatrix} Q_{xx} \\ Q_{yy} \\ Q_{xy} \\ Q_{ss} \end{Bmatrix} \tag{4.13}$$

The positive and negative transformations differ because of the sign of the odd powers of sine (which is an anti – symmetrical function), which are present in the shear couplings components.

Now the following trigonometric identities are introduced to transform relations from the fourth powers of trigonometric function to those in multiple angles:

$$\cos^4\theta = \frac{3+4\cos 2\theta + \cos 4\theta}{8} = m^4 \tag{4.14}$$

$$\cos^3\theta \ \sin\theta = \frac{2\sin 2\theta + \sin 4\theta}{8} = m^3n \tag{4.15}$$

$$\cos^2\theta \ \sin^2\theta = \frac{1-\cos 4\theta}{8} = m^2n^2 \tag{4.16}$$

$$\cos\theta \ \sin^3\theta = \frac{2\sin 2\theta - \sin 4\theta}{8} = mn^3 \tag{4.17}$$

$$\sin^4\theta = \frac{3-4\cos 2\theta + \cos 4\theta}{8} = n^4 \tag{4.18}$$

When the transformation relations are repackaged by substituting these identities into those in Equation 4.7, a set of linear combinations of the principal stiffness, listed in Table 4.1, are obtained.

Three of these combinations are invariants. Invariants are very important for composite materials design, because, regardless of laminate layup of multidirectional plies, they remain constant.

The transformation relations (4.13) can now be rearranged in order to be a linear combination

	Q_{xx}	Q_{yy}	Q_{xy}	Q_{ss}	Invariant?
$U_1 = U_4 + 2U_5$	3/8	3/8	1/4	1/2	YES
U_2	1/2	-1/2	0	0	NO
U_3	1/8	1/8	-1/4	-1/2	NO
$U_4 = U_1 - 2U_5$	1/8	1/8	3/4	-1/2	YES
$U_5 = (U_1 - U_4)/2$	1/8	1/8	-1/4	1/2	YES

Table 4.1: Linear combinations of on-axis stiffness moduli

of Us and multiple angles functions:

$$\begin{Bmatrix} Q_{11} \\ Q_{22} \\ Q_{12} \\ Q_{66} \\ Q_{16} \\ Q_{26} \end{Bmatrix} = \begin{bmatrix} U_1 & U_2 & U_3 & 0 & 0 \\ U_1 & -U_2 & -U_3 & 0 & 0 \\ U_4 & 0 & -U_3 & 0 & 0 \\ U_5 & 0 & -U_3 & 0 & 0 \\ 0 & 0 & 0 & U_2/2 & U_3 \\ 0 & 0 & 0 & U_2/2 & -U_3 \end{bmatrix} \begin{Bmatrix} 1 \\ \cos 2\theta \\ \cos 4\theta \\ \sin 2\theta \\ \sin 4\theta \end{Bmatrix} \tag{4.19}$$

Writing tensorial off-axis stress-strains relations a two factor appears in the third column:

$$\begin{Bmatrix} \sigma_1 \\ \sigma_2 \\ \sigma_6 \end{Bmatrix} = \begin{bmatrix} Q_{11} & Q_{12} & 2Q_{16} \\ Q_{21} & Q_{22} & 2Q_{26} \\ Q_{61} & Q_{62} & 2Q_{66} \end{bmatrix} \begin{Bmatrix} \varepsilon_1 \\ \varepsilon_2 \\ \varepsilon_6 \end{Bmatrix} \tag{4.20}$$

By summing the components of the main diagonal of the stiffness matrix its trace is obtained:

$$trace[Q] = Q_{11} + Q_{22} + 2Q_{66} \tag{4.21}$$

Using the relations presented in (4.19) trace [Q] can be written as a function of Us and multiple angles:

$$trace[Q] = 2U_2 + 2U_5 = 2(U_1 + U_5) \tag{4.22}$$

Therefore, it is clear that the trace [Q] is an invariant, as it is the linear combination of two invariants. Trace is a fundamental property of the material and represents the total and upper bound of the stiffness property of a material in an explicit form as defined by mathematics. It is independent by the loading condition (in-plane versus flexural), stacking sequence (mid-plane symmetric versus asymmetric), and material symmetry: isotropic, orthotropic and anisotropic. Since trace[Q] is an invariant with respect to coordinate transformations, in a laminate, the trace of the thickness-normalized inplane (A^*) and flexural (D^*) stiffness matrices are also the same:

$$trace[A^*] = trace[D^*] = trace[Q] \tag{4.23}$$

This is a crucial result and for the merits on the research the invariant trace[Q] has been named as Tsai's Modulus in 2020 by Albertino, Sharma et al. [22].

4.1.1 Master ply for carbon/polymer composites

It was found that carbon fiber/epoxy and thermoplastic composite materials share common stiffness properties when they are normalized by their respective Tsai's Modulus. Tsai and Melo [6] in their analysis proposed ten different carbon fiber composites and found that their trace-normalized stiffness factors were very close (tab. 4.2). In particular, they found that the longitudinal stiffness (parallel to the fiber) has a coefficient of variation equal to 1.5%. The median values of these factors define a 'master ply' used to gain understanding of the laminate behavior of these composites.

The variation on the matrix dominated transverse and shear properties are larger because different matrices and curing processes are used. However, their effect on laminate properties is small. The stiffness along the fiber is, in fact, responsible for about 88% of the trace for the unidirectional carbon/epoxy composites; thus, uncertainty from matrix related property is masked by the dominant fiber property, which has a small variation of 1.5%. Hence, the matrix contribution and its wider variation are of small consequence when ply stiffness is converted to laminate stiffness.

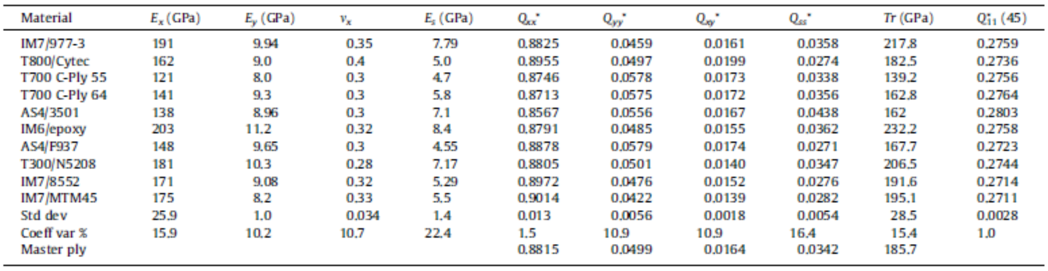

Material	E_x (GPa)	E_y (GPa)	ν_x	E_s (GPa)	Q_{xx}^*	Q_{yy}^*	Q_{xy}^*	Q_{ss}^*	Tr (GPa)	Q_{11}^* (45)
IM7/977-3	191	9.94	0.35	7.79	0.8825	0.0459	0.0161	0.0358	217.8	0.2759
T800/Cytec	162	9.0	0.4	5.0	0.8955	0.0497	0.0199	0.0274	182.5	0.2736
T700 C-Ply 55	121	8.0	0.3	4.7	0.8746	0.0578	0.0173	0.0338	139.2	0.2756
T700 C-Ply 64	141	9.3	0.3	5.8	0.8713	0.0575	0.0172	0.0356	162.8	0.2764
AS4/3501	138	8.96	0.3	7.1	0.8567	0.0556	0.0167	0.0438	162	0.2803
IM6/epoxy	203	11.2	0.32	8.4	0.8791	0.0485	0.0155	0.0362	232.2	0.2758
AS4/F937	148	9.65	0.3	4.55	0.8878	0.0579	0.0174	0.0271	167.7	0.2723
T300/N5208	181	10.3	0.28	7.17	0.8805	0.0501	0.0140	0.0347	206.5	0.2744
IM7/8552	171	9.08	0.32	5.29	0.8972	0.0476	0.0152	0.0276	191.6	0.2714
IM7/MTM45	175	8.2	0.33	5.5	0.9014	0.0422	0.0139	0.0282	195.1	0.2711
Std dev	25.9	1.0	0.034	1.4	0.013	0.0056	0.0018	0.0054	28.5	0.0028
Coeff var %	15.9	10.2	10.7	22.4	1.5	10.9	10.9	16.4	15.4	1.0
Master ply					0.8815	0.0499	0.0164	0.0342	185.7	

Figure 4.2: Trace normalized plane stress stiffness components and engineering constants

In conclusion, master ply's engineering constants and stiffness components are equal to [21]:

$$E_x^* = \frac{E_x}{tr[Q]} = 0.880 \qquad E_y^* = \frac{E_y}{tr[Q]} = 0.052 \qquad E_s^* = \frac{E_s}{tr[Q]} = 0.031 \tag{4.24}$$

$$Q_{xx}^* = \frac{E_x^*}{1-\nu_x\nu_y} = 0.885 \qquad Q_{yy}^* = \frac{E_y^*}{1-\nu_x\nu_y} = 0.0525 \tag{4.25}$$

$$Q_{xy}^* = \nu_x E_y = 0.0167 \qquad Q_{ss}^* = 0.0313 \tag{4.26}$$

4.2 Tsai's Modulus application in structural optimization and design

The opportunities brought by this new invariant based approach based on Tsai's Modulus are almost endless. Arteiro A., Sharma N. et al. [22] cited numerous applications of this new approach in their article. Among them there is a directed laminate sizing method proposed by Tsai et al. [23] using Tsai's Modulus as a normalizing factor. Laminate selection could, therefor, be performed independently of the material system. Material selection would be the last step, according to strength and stiffness requirements. The latter could be matched by direct scaling using the Tsai's modulus. Tsai et al [24] proposed a method where shape optimization of tapered beams could be easily performed, allowing an easy calculation of weight saving with a given material. Shrivastava et al. [25] used stiffness components normalized by Tsai's modulus in layup optimization of a wing box, including thermal deformation analysis. Some universal carpet plots normalized by Tsai's Modulus, valid for every CFRP, have been proposed by Melo et al. [26] and by Barbero [27]. These carpet plots are not sensitive to environmental conditions and the actual Young's and shear moduli can be immediately recovered simply by using the corresponding value of the Tsai's modulus, at the respective environmental conditions. Tsai et al. [21] proposed a possible simplification of the current design certification and processes based on a practical case study without posing risk to the safe design of structures at larger scales. In fact, the result of the analysis is that one test at the laminate level could repalce the three independent tests at the ply level required by current design and certification processes. Furtado et al. [28] used the invariant approach and the master ply concept to obtain the elastic properties of balanced multi-directional laminate and their sub-laminates, in order to predict open–hole strength of laminated panels. Differences below 3% were found for high-strength CFRP systems and below 7% for high-modulus CFRP systems. Also in the field of notched composites Melo et al. [26] obtained the stress concentration factors for open–hole laminates using the normalized Master ply properties, hence valid for any CFRP. Dalli et al. [29, 30] used trace-normalized moduli to simplify the expressions of the geometric correction factors used in fracture mechanics of orthotropic bodies, proposing a general formulation for the Energy release rate valid for the majority of standard balanced woven CFRPs.

Chapter 5

AVL

AVL (Athena Vortex Lattice) is a vortex lattice method originally written by by Harold Youngren circa 1988 for the MIT Athena TODOR aero software collection, and developed by Mark Drela and Harold Youngren.

As every vortex lattice method code the geometry consists of a lattice of 2D panels, on which is placed an horseshoe vortex. The trailing legs of the horseshoe filaments are assumed to be parallel to the x axis. Thus AVL is best suited for aerodynamic configurations which consist mainly of thin lifting surfaces at small angles of attack and sideslip [31]. Furthermore, AVL allows to model slender bodies as fuselages via source plus doublet filaments.

AVL assumes quasi-steady flow, meaning that unsteady vorticity shedding is neglected. It assumes the limit of small reduced frequency, which means that any oscillatory motion must be slow enough so that the period of oscillation is much longer than the time it takes the flow to traverse an airfoil chord. The yaw, pitch and yaw rates used in the computation must be slow enough so that the resulting relative flow angles are small.

Complex wing and aircraft geometries can be modeled in AVL. It is, in fact, possible to model dihedral angle, aileron deflection, high lift devices, both in the leading edge and in the trailing edge. The airfoil lifting properties are modeled by the software by giving it simply the airfoil coordinates. Control surfaces can be model in the same way too.

The general freestream is described through the following parameters/techniques:

- α: angle of attack;
- β: sideslip angle;
- p, q, r: aircraft rotation components;
- Subsonic Prandtl-Glauert compressibility treatment.

By giving it some constraints, such as the required C_L or moments, AVL can execute trim calculations. It can then give the following aerodynamic outputs:

- Direct forces and moments on elements;
- Trefftz plane;
- Derivatives of forces and moments, w.r.t freestream, rotation, controls;

- In body or stability axes.

Optional mass properties file can also be defined to execute eigenmode flight dynamics analysis, as:

- Rigid-body analysis with quasi-steady aero model;
- Display of eigenvalue root progression with a parameter;
- Display of eigenmode motion in real time;
- Output of dynamic system matrices.

5.0.1 Vortex lattice spacing distributions

AVL offers a set of possible discretizations for both spanwise and chordwise wing's directions. The possible discretizations are controlled by the spacing parameters Sspace, Cspace and Bspace, that must fall in the range between -3 and 3. The dicretization distribution associated to each parameter is presented in figure 5.1, and are:

- Equal;
- Sine;
- Cosine.

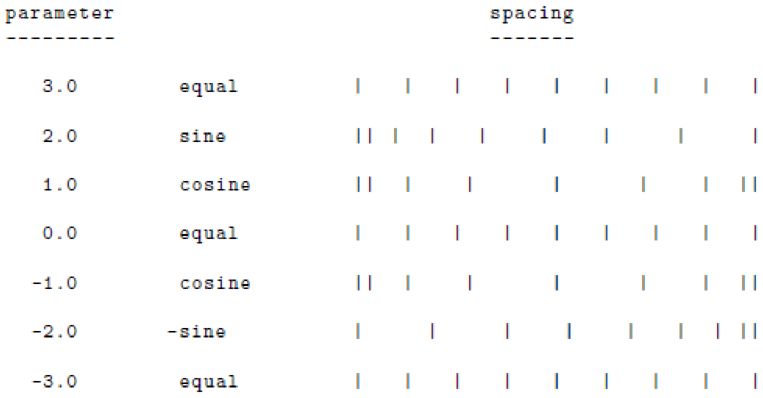

Figure 5.1: Possible AVL discretizations [31]

The most efficient distribution is usually the cosine both chordwise and spanwise . If the wing does not have a significant chord slope discontinuity at the centreline then the -sine distribution from root to tip will be more efficient [31].

To get good results in AVL a set of vortex-spacing rules must be followed:

- In a standard VL method a trailing vortex leg must not pass close to a downstream control point. Consequently surfaces that are lined up along the x direction (that have almost the same y and z components) must have the same spanwise vortex spacing;
- Spanwise vortex spacings should be “smooth", with no sudden changes in spanwise strip width;

- If a surface has a control surface on it, an adequate number of chordwise vortices should be used to resolve the discontinuity in the camberline angle at the hingeline;
- When refining the mesh it is generally necessary to refine in both spanwise and chordwise directions. Refining along only one direction may not converge to the correct result.

Chapter 6

Wing geometry definition

The first step before beginning the analysis is the creation of the CAD of the wing.

The CAD was created with CATIA v5 software. The geometry is all parameterized in function of wing root chord and the fraction $\frac{1}{2}\,\frac{span}{root\ chord}$. The surface area is imposed as $A = 9\ m^2$ and the span imposed is equal to $b = 13,5\ m$. From this data the aspect ratio can be evaluated as:

$$AR = \frac{b^2}{A} = 20.25 \tag{6.1}$$

From AR the mean aerodynamic chord can be evaluated:

$$c_{aero} = \frac{b}{AR} = 0.667\ m \tag{6.2}$$

The wing geometry is created using an ellipse as reference. Then it is divided into three traits using a cosine distribution. Since there must be two intermediate sections the law is applied by using $\theta = [30, 60]$ to find the y coordinate of the sections, applying the law:

$$y = cos(\theta) \tag{6.3}$$

The first section will, therefor, be at 50% of semi-span and the second section will be near $86,6\%$ of semi-span. The first spar is set straight, so the wing will not follow a perfectly elliptical shape, but it will appear a little swept forward. The relative chordwise position of the main spar is set as an editable parameter initially to 30% of chord. The plan areas in the three traits are calculated in order to be equivalent to the respective ellipse's surfaces. The obtained sketch of the wing structure is presented in figure 6.1. Referring to the figure's axis system the main dimension of the wing are here listed:

- Wing semi-span = 6758 mm;
- Wing root chord = 850 mm;
- First kink y coordinate = 3379 mm;
- First Kink chord = 740 mm;
- Second kink y coordinate = 5853 mm;

- Second kink chord = 493 mm;
- Tip chord = 145 mm.

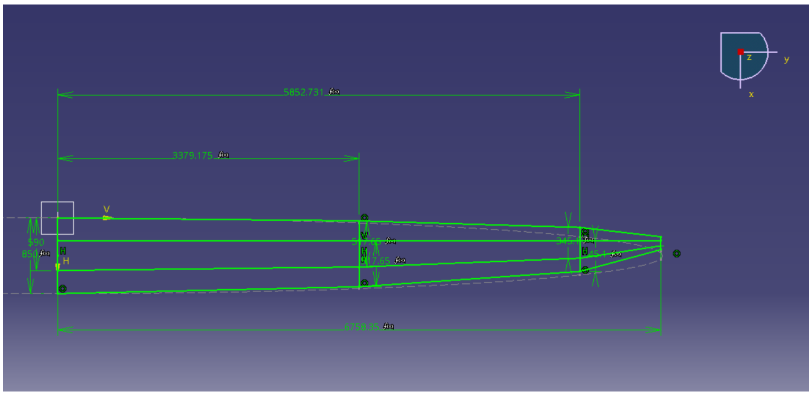

Figure 6.1: Sketch of the wing

Obtained the main structure now the wing profile coordinates (fig. 6.7) are imported in the software in order to match the cord length. The profile NACA 64_1412 is chosen. By importing the profile coordinates a series of point is created by the software. The wing profile is then reconstructed using two nurb curves which approximate in the best way possible the shape of the wing. From these two curve it is now easy to realize the bottom and top surfaces of the wing, extruding the profile along the leading edge and the trailing edge lines. The two spars are than realised with surfaces extruded along z direction and then trimmed with the top and bottom surfaces. The ribs located in the kink are realised by filling the profile section.

Then the flap and the ailerons are inserted. The configuration chosen for both is the plain flap configuration, as it is one of the most common solution for sailplanes high lift devices. The aileron hinge is placed at 80% of chord, as for wing of normal thickness ratio little benefit is obtained by increasing the flap cord to more than 20% of chord [32]. From side view the section of the wing appears as figure 6.2.

After that, the three ribs located are holed, leaving a width of 30 mm for the root rib, 20 mm for the rib located in the first kink and 17 mm for the last rib. The width of the ribs shear webs varies in function of the dimension of the rib . The back part of the ribs, located between the rear spar and the flap/ailerons. The ribs obtained are presented in figure 6.4.

Then on the panels the spar's flanges are introduced by projecting two curves that develop alongside the spars (one in front of the main spar and one behind the back spar). In the FEM model on this two thin surfaces the lamination relative to the flange will be applied. The main spar's flange width is editable and is set to 80 mm from the root section to the second kink, then its width is reduced linearly till 30 mm at the wing tip in order to not intersect the wing leading edge. The rear flange width is set to 60 mm between the root section and the first kink, then its width reduces linearly to 40 mm towards the second kink and then till 12 mm at the wing tip. This tapering is done in order to not intersect the aileron leading edge.

Last, a reinforcement to allow the application of the boundary conditions is realised. The objective is to create a wing box able to sustain the root loads. First the main spar is extruded along negative spanwise direction coordinates for 600 mm. Then a surface parallel to the one just extruded is realized in correspondence of the flange foremost point. Now a diagonal surface that reaches inside the wing is created to connect this surface to the spar's shear web (fig 6.5). The connection point is located at a y coordinate equal to three times the spar root height. Then two circular holes are realised in the wing box to simulate the presence of two bolt joints. The holes axes are located at 20% and 80% of the box extrusion length (respectively 120 mm and 480 mm) and the holes radius are 20 mm (fig .6.6).

The baseline CAD obtained is presented in figure 6.3. This will be the starting point for the structural optimization of the wing.

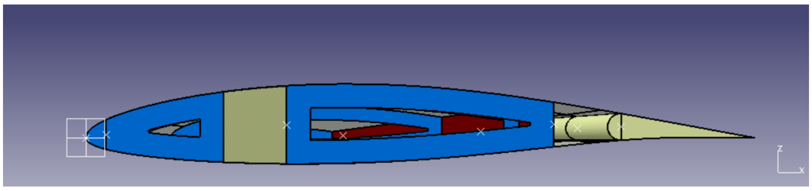

Figure 6.2: Wing root section

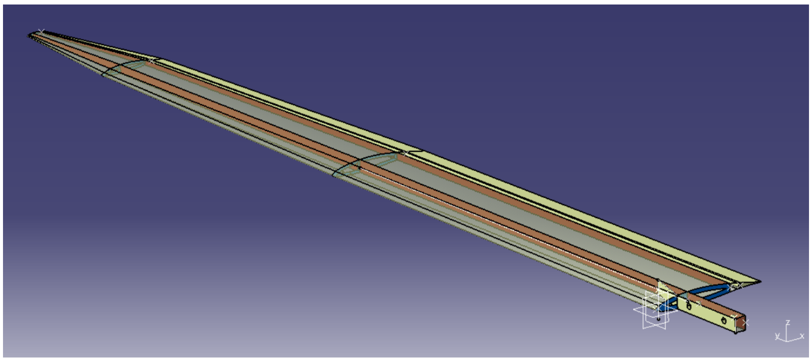

Figure 6.3: Baseline CAD

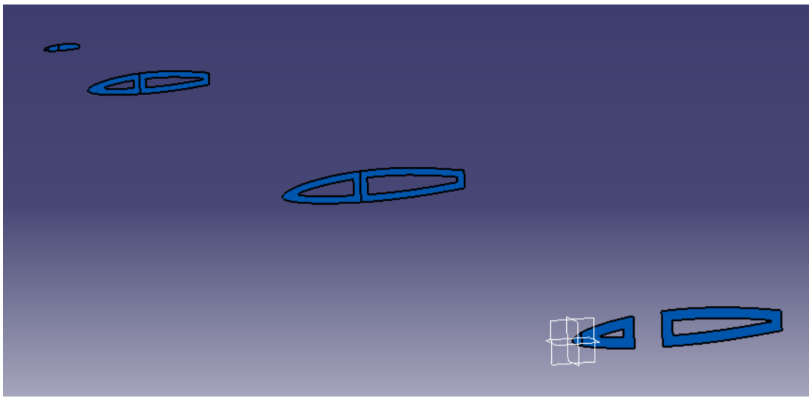

Figure 6.4: Ribs

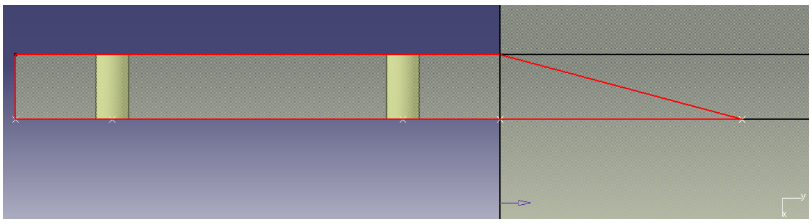

Figure 6.5: Box spars

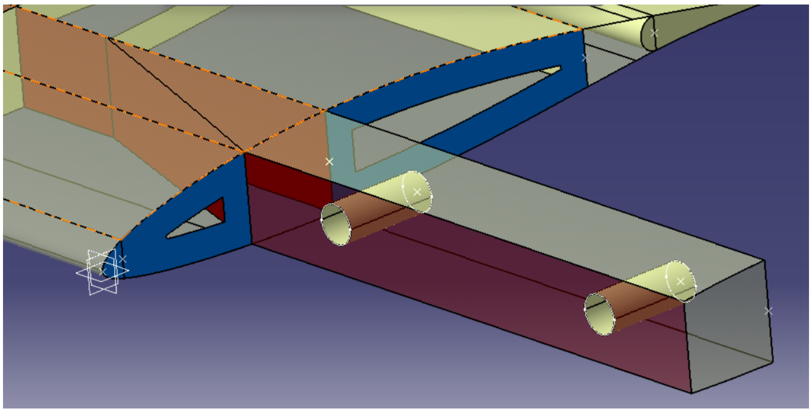

Figure 6.6: Box geometry

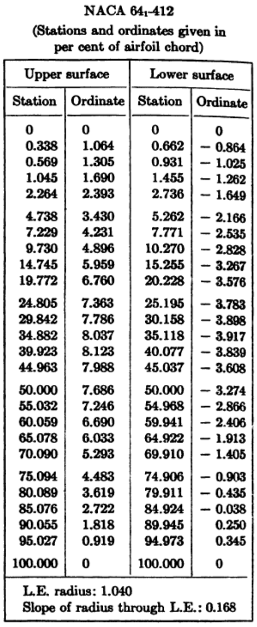

NACA 64_1-412
(Stations and ordinates given in
per cent of airfoil chord)

Upper surface		Lower surface	
Station	Ordinate	Station	Ordinate
0	0	0	0
0.338	1.064	0.662	− 0.864
0.569	1.305	0.931	− 1.025
1.045	1.690	1.455	− 1.262
2.264	2.393	2.736	− 1.649
4.738	3.430	5.262	− 2.166
7.229	4.231	7.771	− 2.535
9.730	4.896	10.270	− 2.828
14.745	5.959	15.255	− 3.267
19.772	6.760	20.228	− 3.576
24.805	7.363	25.195	− 3.783
29.842	7.786	30.158	− 3.898
34.882	8.037	35.118	− 3.917
39.923	8.123	40.077	− 3.839
44.963	7.988	45.037	− 3.608
50.000	7.686	50.000	− 3.274
55.032	7.246	54.968	− 2.866
60.059	6.690	59.941	− 2.406
65.078	6.033	64.922	− 1.913
70.090	5.293	69.910	− 1.405
75.094	4.483	74.906	− 0.903
80.089	3.619	79.911	− 0.435
85.076	2.722	84.924	− 0.038
90.055	1.818	89.945	0.250
95.027	0.919	94.973	0.345
100.000	0	100.000	0

L.E. radius: 1.040
Slope of radius through L.E.: 0.168

Figure 6.7: NACA $64_1$412 coordinates [32]

Chapter 7

Static sizing

Before executing the flutter analysis the wing must be properly sized to resist to static loads, in order to then obtained realistic flutter results. Therefor, in this chapter the sizing to static loads is presented. There will be, as well, a long presentation of the FEM model realized, that will be the basis for every further work.

7.1 FEM Model

In this subsection the development of the FEM model used for the static sizing is presented. The FEM model is developed on the baseline CAD presented in Chapter 6. Based on the results of the static analysis the model will be sized to not have failures following the Tsai-Wu criterion. The FEM model has been realized on Simcenter Femap. The consistent units used for the model are presented in table 7.1.

Mass	Length	Time	Force	Stress	Density	Gravity
$tonn$	mm	s	N	MPa	$tonn/mm^3$	$9810\,mm/s^2$

Table 7.1: Consistent units

7.1.1 Mesh

The first thing executed during the creation of the model is the mesh on the CAD surfaces. For the mesh creation the main objective was to use only CQUAD elements, without having to use any TRIA element in order to obtain a very good mesh quality. This was obtained by slightly modifying the CAD topology, by, for instance, splitting some surfaces.

The mesh was defined starting from the smallest surfaces, like the ribs' leading edge zone and the flanges' small side.

For the front spar's flange small side a mesh seed of 6 six elements was set. This number of elements resulted to be a good compromise between obtaining a smooth mesh relative to the CAD topology and in the mean time having an enough fine discretization in this highly loaded part. The resulting element size was around 13.5 mm at the root station. To keep a good mesh quality also in the spanwise direction, but at the meantime not increase too much the number of cells a biased spacing option is set in the spanwise mesh seed, with a bias factor of 1.3, in order to have smaller cells near the root section. The number of element chosen is 63 spanwise elements, 39 between root section and first kink, 19 between first and second kink and 5 between second kink and wing tip.

For the rear flange small side 5 elements have been inserted, with an element length of nearly 15 mm. This setting also respects the same conditions exposed before.

For the ribs three elements are inserted transversely in the leading edge zone and on the long sides, while two transversal elements are inserted in the short sides. Chordwise, on the leading edge a mesh seed of four elements is set with a bias factor of 1.3 towards the centre in order to be able to represent well enough the leading edge shape. In this leading edge region the rib topology is modified in order to obtain a nice sheaf that surrounds entirely the inside hole. For the front part beetween the leading edge and the front flange some biased discretizations are applied to the various ribs in order to obtain the smoothest mesh possible while using the least elements. Six elements are set there. For the mid part between the flanges an other biased discretization has been used for the same reasons, putting there 11 elements. In the vertical direction, in the root rib ten elements has been inserted in the junction with the front spar in order to have a good mesh quality on the rib, on the spar's shear web and in the wing box. To not incur in topology errors ten elements have been set also in the junction between the wing box front shear web and the root rib. In the junction with the rear spar 8 elements have been set, since there the airfoil is thinner.

These mesh seed number set for the root rib are carried equal to the other ribs, as can be seen in figure 7.1a, 7.1b, 7.2a and 7.2b. The skin and the spars' shear web are then meshed consequently.

For the wing box a mesh size equal to 10 mm is set. Then two pads with washer are created on each box side around the holes, in order to improve the mesh quality. The pad factor is set to 0.5. With these settings a good mesh can be obtained executing some other minor topology modification to allow the software to carry the correct number of element from one side of the box to the other (fig. 7.6).

The total elements obtained using these settings are:

Element type	Number of elements
CQUAD	8758
CTRIA	0

Table 7.2: Number of mesh elements

The obtained mesh quality looks good, with only some small elements in the highest curvature zones in the ribs characterized by a Jacobian over 0.6 (fig. 7.7). The mesh obtained is more fine in the more loaded parts, or with possible high loads gradients, and more coarse in the zones with high chances of having constant or low loads, as for example skin panels (fig. 7.4).

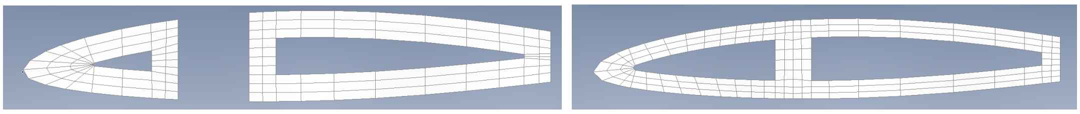

(a) Root rib mesh

(b) First kink rib mesh

Figure 7.1: Side view of first two ribs' mesh

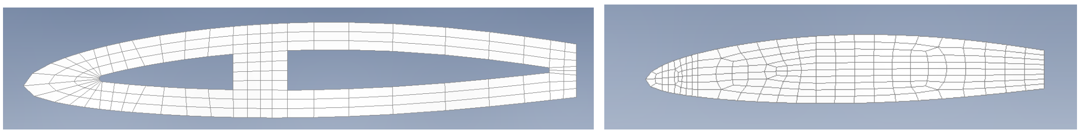

(a) Second kink rib mesh

(b) Tip rib mesh

Figure 7.2: Side view of second two ribs' mesh

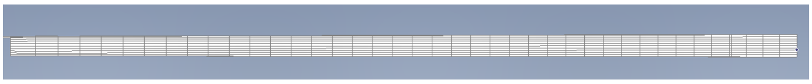

Figure 7.3: Side view of spar's shear web mesh

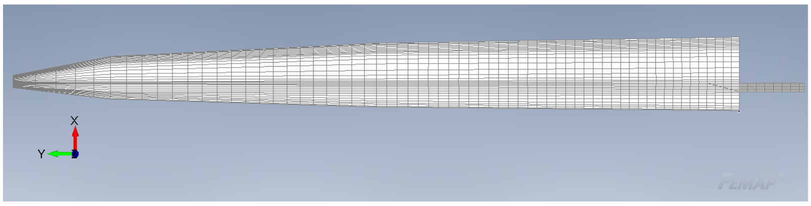

Figure 7.4: TOP view of the mesh

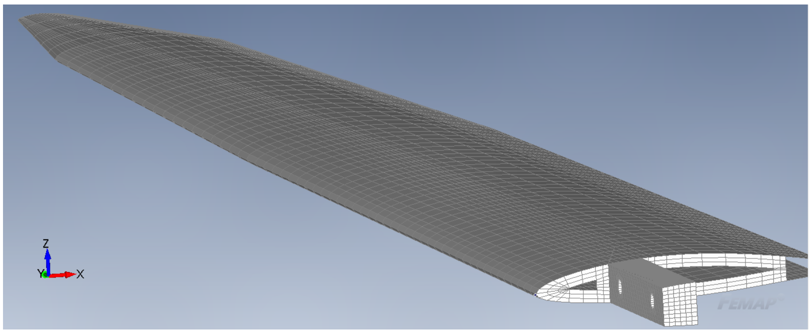

Figure 7.5: Isometric view of the mesh

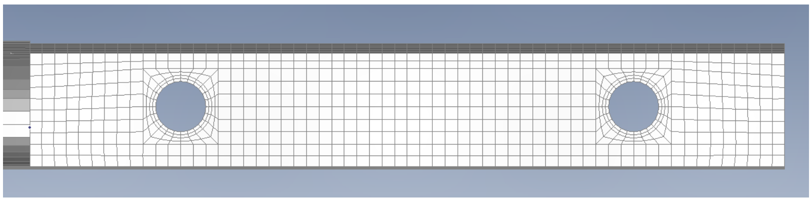

Figure 7.6: Side view of the wing box

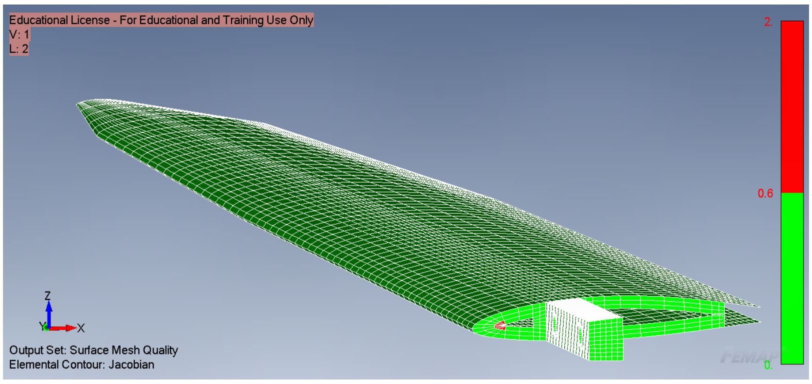

Educational License - For Educational and Training Use Only
V: 1
L: 2

Output Set: Surface Mesh Quality
Elemental Contour: Jacobian

2.
0.6
0.
Z
Y
X
FEMAP

Figure 7.7: Jacobian value on mesh

7.1.2 Materials and global plies definition

After having realised the mesh now it is necessary to define the properties to be assigned to the mesh elements. As the kernel of the thesis is evaluating the relationship between Tsai's Modulus and the flutter behaviour of the wing a model capable of representing composites laminates must be used. The materials must be, therefor, declared as 2D orthotropic. Then, these materials must be stuck in a layup which will be assign to the elements' properties.

Since the model to be analyzed is quite complex the layup sequence is defined using global plies. This method allows to simplify post processing and also make easier to execute modifications on the model by simply adding or removing global plies to a layup sequence.

Since in the global plies definition only a single ply can be defined, the material has been defined as an equivalent global lamination block, putting inside the material properties the resulting moduli of a laminated plate with a lamination equal to the global blocks to be used in the analysis. The three global plies used in the model are 2D orthotropic materials equivalent to:

- $[+0/+50/-50/-0]$ DD lamination;
- $[+45/-45]$ lamination;
- $[0]$ single ply.

Their equivalent moduli are respectively presented in the tables 7.3, 7.4 and 7.5. It can be noted how the values used for the [0] ply refer to the master ply values.

The resulting material properties has been evaluated using an Octave script based on material transformations relations (4.13) and classical lamination theory. The results obtained are compared to the data presented by Tsai, Sharma et al. in 2019 [33], where they characterized a $[0/50/-50/-0]$ DD with a Tsai's Modulus of 118294 MPa and to the Femap layup moduli computation. That value of Tsai's Modulus is the one imposed for the optimization phase. The material properties are then inserted in Femap as a function of Tsai's Modulus. The terms G_{1z} and G_{2z} has been deduced from Tsai's and Melo's "Composite Materials design and testing" [34]. The terms have been imposed to 3500 MPa as a mean value of the epoxy carbon fiber composites presented in the cited book, as both terms are matrix dominated component.

Modulus				Value
E_1	=	$0.485\,TM$	=	$57350\,MPa$
E_2	=	$0.179\,TM$	=	$21166\,MPa$
ν_{12}		=		0.551
G_{12}	=	$0.126\,TM$	=	$14899\,MPa$
G_{1z}	=	C_{66}	=	$3500\,MPa$
G_{2z}	=	C_{44}	=	$3500\,MPa$

Table 7.3: $[0/50/-50/-0]$ equivalent 2D orthotropic material properties

The thickness to be attributed to these global plies is evaluated through rule of mixtures. Hypothesizing to have a carbon fibre with a density equal to 1.8 g/cm^3 and a aereal density

Modulus				Value
E_1	=	$0.110\,TM$	=	$13002\,MPa$
E_2	=	$0.110\,TM$	=	$13002\,MPa$
ν_{12}		=		0.774
G_{12}	=	$0.225\,TM$	=	$26730\,MPa$
G_{1z}	=	C_{66}	=	$3500\,MPa$
G_{2z}	=	C_{44}	=	$3500\,MPa$

Table 7.4: $[+45/-45]$ equivalent 2D orthotropic material properties

Modulus				Value
E_1	=	$0.880\,TM$	=	$104059\,MPa$
E_2	=	$0.052\,TM$	=	$6149\,MPa$
ν_{12}		=		0.32
G_{12}	=	$0.0313\,TM$	=	$3666\,MPa$
G_{1z}	=	C_{66}	=	$3500\,MPa$
G_{2z}	=	C_{44}	=	$3500\,MPa$

Table 7.5: $[0]$ equivalent 2D orthotropic material properties

of 150 g/m^2, an epoxy matrix with a density of 1.2 g/cm^3 and an aereal density of 75 g/cm^3, with a volume fraction of carbon equal to 0.55 a single ply thickness of 0.103030 *mm* is obtained. To find the thickness of the $[+45/-45]$ and of the DD block it is enough to multiply that value respectively by two and by four.

Since for the sizing will be necessary to evaluate failure index on the structure, limit stress must be given as input in the material cards. Starting from the known value of longitudinal tensile and compression stress limit of the $[0/50/-50/-0]$ DD other layups failure properties are evaluated from inverse transformation relationship (4.13), obtaining the results presented in table 7.6 for the DD lamination, table 7.7 for the $[+45/-45]$ lamination and table 7.8 for the $[0]$ ply.

	Direction 1	Direction 2
Tension	$1082\,MPa$	$400.07\,MPa$
Compression	$618\,MPa$	$228.5\,MPa$
Shear	$248.51\,MPa$	

Table 7.6: $[0/50/-50/-0]$ DD failure stress limits

	Direction 1	Direction 2
Tension	$542.24\,MPa$	$542.24\,MPa$
Compression	$309.71\,MPa$	$309.71\,MPa$
Shear	$447.24\,MPa$	

Table 7.7: $[+45/-45]$ failure stress limits

7.1.3 Layups and properties definition

On the baseline FEM model to be used for the first static analysis there will be two layers of DD on the wing skin, which will be identified as global ply 1 and 2, two layers of $[+45/-45]$

	Direction 1	Direction 2
Tension	1753 MPa	103 MPa
Compression	1001 MPa	58.83 MPa
Shear	61.4 MPa	

Table 7.8: [0] failure stress limits

on the shear webs that will be identified as global plies 101 and 102. Since in the flanges there must be a continuity with the global plies of the shear web and the global plies of the skin, as it would be in realty, attention must be put to use the same global plies ids and stack them in the correct order. So, for the flanges the layup sequence imposed is:

Bottom	
Global ply id	lamination sequence
1	$[+0/+50/-50/-0]$
2	$[+0/+50/-50/-0]$
101	$[+45/-45]$
201	$[0]$
102	$[+45/-45]$
top	

Table 7.9: Flange lamination

The obtained lamination for a cross section around the main spar is presented in figure 7.8. The green lines represent the skin global plies, with the DD lamination. The blue lines represent the $[+45/-45]$ global plies that extends from the shear webs to the flanges. Last, the purple lines represent the $[0]$ global ply in the flanges.

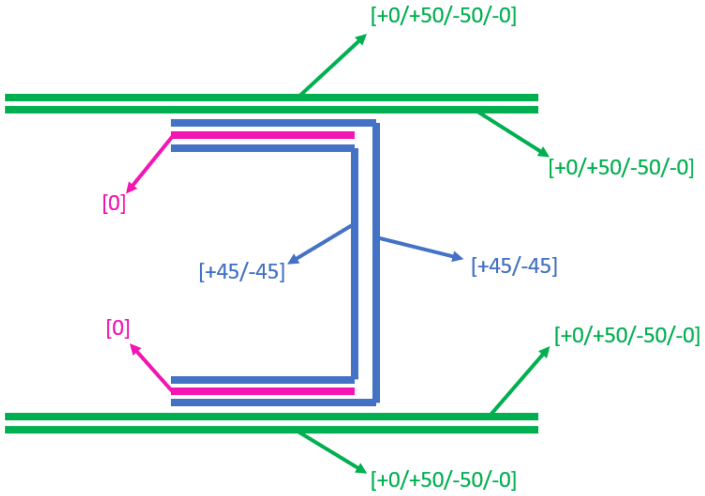

Figure 7.8: Cross sectional view of lamination around a spar

During the optimization iterations using global plies is easier to add or remove an entire lamination block from an element, as it would be done in a real wing. In the flange up to three layers of $[0]$ can be add between two layers of $[+45/-45]$. On the skin and on the shear webs blocks of global plies respectively representing laminations of $[+0/+50/-50/-0]$

and $[+45/-45]$ can be add or removed as necessary. The main two global plies identified respectively as 1,2 and 101 and 102 must always be the first and last plies of the lamination sequence of the skin and of the shear webs to have coeherence in the model.

When assigning the layup sequence to the properties is now important to set an options that allows to stack the plies starting from the CAD surface line toward the inside of the wing. That is done by activating the option "Offset from bottom surface" in the property card and checking that all the surfaces normals points toward the inner of the wing. An other check that can be done is to verify that also the elements normals point towards the inner of the wing. Finally the Tsai-Wu failure criterion is activated in the property card.

The correct properties assignment can be verified assigning a colour to the element properties. In figure 7.9 the yellow colour is assigned to the skin's property, the blue color to the shear web's property and the red colour to the flange's property.

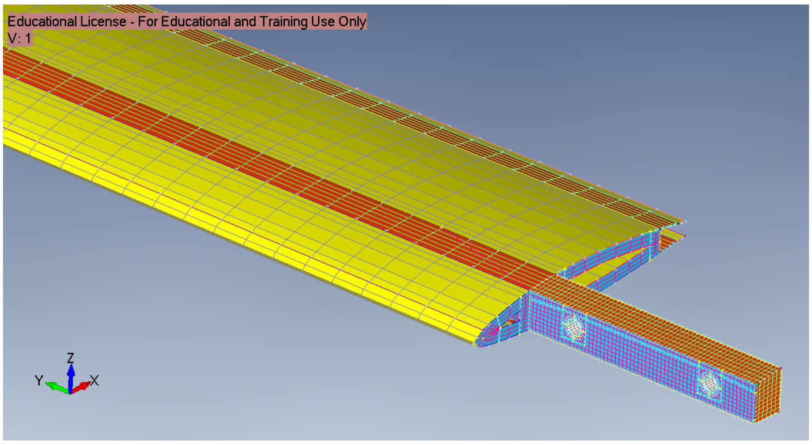

Figure 7.9: Different properties assigned to elements

7.1.4 Boundary conditions and loads

The boundary conditions are set to simulate the presence of two ball joint on the root rib and two bolt connection on the holes (fig. 7.10).

Therefore, on the node place near 3% of chord near half the thickness of the airfoil the translations in x and z are fixed.

On the node place at half thickness in correspondence of the intersection with the rear spar the translation in z is fixed.

On the surface of the hole nearer to the wing translation in z and rotation in y and z are fixed.

On the surface of the hole further from the wing translation in y and z are fixed, as well as rotations in y and z.

To simulate the presence of an acceleration of 10 g a body load is created, that take in count presence of angle of attack and diehdral.

For the aerodynamic loads definition a pressure surface from a data table imported from AVL is created, as described better in the following chapter.

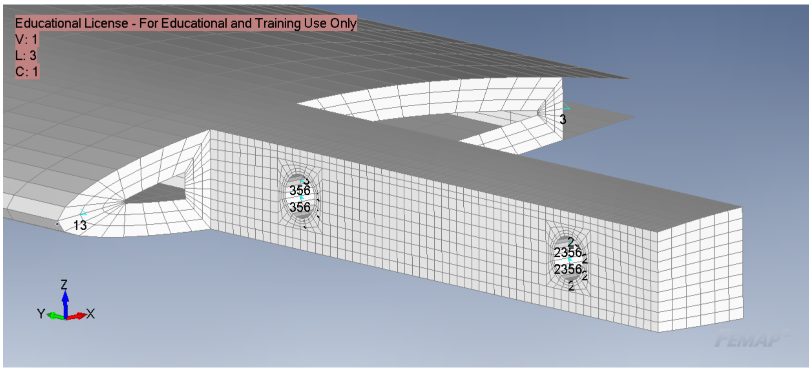

Figure 7.10: Boundary conditions

7.2 Aerodynamics loads

To evaluate aerodynamics loads is necessary to create an envelope diagram. The aerodynamic parameters to realize the envelope diagram, such $C_{L\ max}$ and $C_{L\ min}$ are evaluated through a vortex lattice method called AVL. Then, after realizing the envelope diagram coefficients of pressure that act on the wing surface are evaluated with AVL too and then imported in Femap. The two loading configurations considered in the sizing are pressures at maximum load factor n_{max} at V_a and at minimum load factor n_{min} at V_g.

7.2.1 2D airfoil aerodynamic characteristics

First it is necessary to find the correct 2D value of $C_{L\ max}$, $C_{L\ min}$, positive and negative stall angle of attack α_{max} and α_{min} of the wing profile NACA 64_1412 to be given as an input to AVL.

Since the aerodynamic curves presented in "Theory of wing sections [32]" (fig. 7.11) change with Reynolds number it is necessary to evaluate the correct Reynolds number at stall speed to find the correct values.

For positive stall, hypothesizing a $C_{L\ max}$ of 1.4 and a wing loading of 40 kg/m^2 the guess stall speed is evaluated:

$$V_{s\ guess} = \sqrt{2\frac{W}{S\ \rho\ C_{L\ max}}} = 20\ m/s \tag{7.1}$$

With sea level ISA condition ($\rho = 1.225\ kg/m^2$). This lead to a Reynolds of guess of:

$$Re_{guess} = \frac{\rho\ V\ L}{\mu} = 900000 \tag{7.2}$$

With $\mu = 1.8\ 10^{-5} \frac{kg}{m\ s}$. In the graph of figure 7.11a, the curve for $Re = 900000$ is not present, so the $C_{L\ max}$ is evaluated through an extrapolation using a parabolic interpolation of the three values of $C_{L\ max}$ given:

- $C_{L\ max} = 1.33$ at $Re = 3\ 10^6$;
- $C_{L\ max} = 1.67$ at $Re = 6\ 10^6$;
- $C_{L\ max} = 1.55$ at $Re = 9\ 10^6$;

which led to a $C_{L\ max}\ guess = 1.45$.
Now the positive stall speed can be reevaluated and the process is iterated since the following values are found:

- $V_{s1} = 21\ m/s$;
- $Re = 964590$;
- $C_{L\ max} = 1.44$.

Using the same process of interpolation the positive stall angle of attack is found:

- $\alpha_{max} = 12.85°$.

For the negative angles of attack the process is easier since the curves don't change much with Reynolds, therefor $C_{L\ min}$ and the negative α_{min} are find straightaway:

- $C_{L\ min} = -1.00$;
- $\alpha_{min} = -12°$.

The value of α_{stall} can now be given as an input to AVL to evaluate the 3D aerodynamic characteristics of the wing.

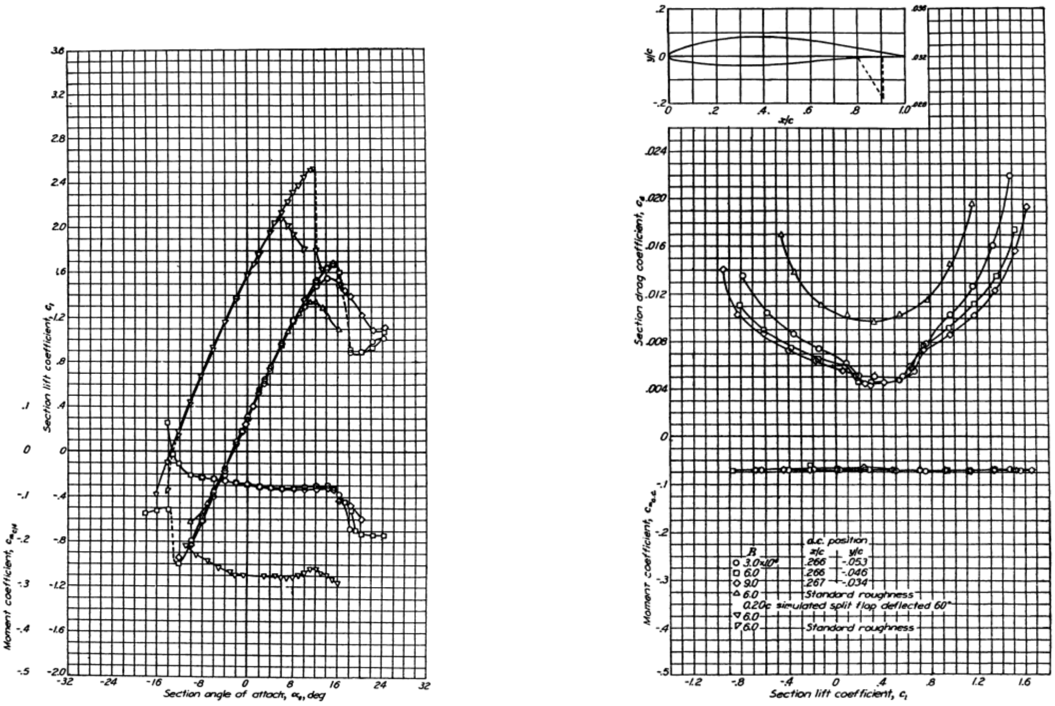

(a) NACA 64_1412 $C_{L\ \alpha}$ and Cm_α curves

(b) NACA 64_1412 $C_{D\ \alpha}$ and $Cm_{ac\ \alpha}$ curves

Figure 7.11: NACA 64_1412 aerodynamic curves [32]

7.2.2 3D wing aerodynamic characteristic

To proceed with the evaluation of the 3D $C_{L\ max}$ and $C_{L\ min}$ first, the wing geometry must be reproduced on AVL. A file .avl (appendix A) is created, representing in a faithful way the wing shape, with the two kinks, the ailerons, and a dihedral angle Γ of 3. For the airfoil reconstruction a file with the airfoil coordinates is read by the .avl file. The obtained wing shape can be seen in figures 7.12 and 7.13.

Now two case study for the analysis are created, one for α_{max} and one for α_{min}. The air density is here set to 1.225 kg/m^3.

Before executing the calculation a definition of the aerodynamic discretization is needed.

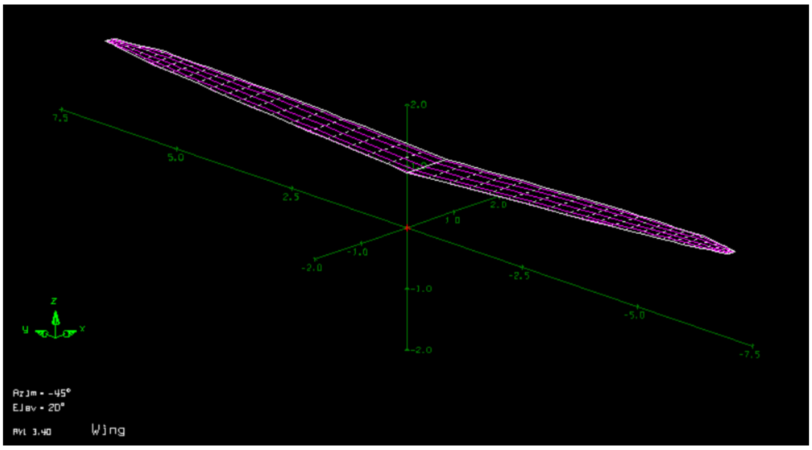

Figure 7.12: AVL geometry isometric view

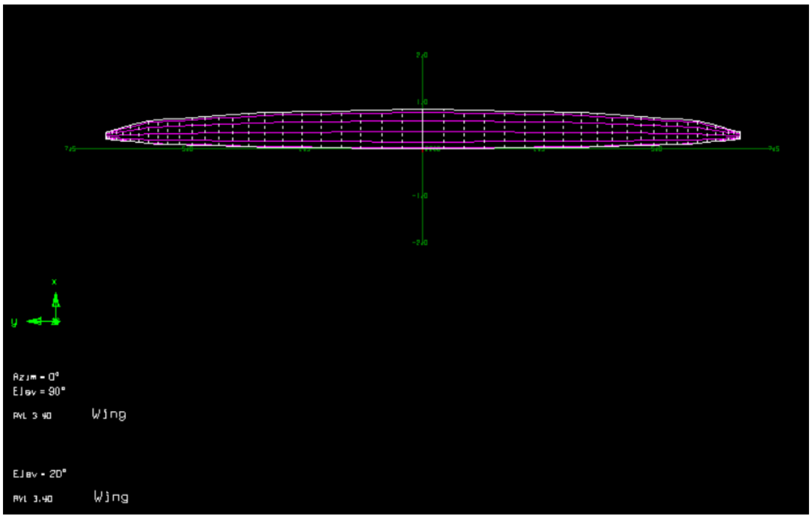

Figure 7.13: AVL geometry top view

For the aerodynamics mesh a cosine distribution is chosen along the chordwise direction and a sine distribution along the spanwise direction, as advised by the AVL User Primer [31] for a wing with little chord slope discontinuity at the centerline. The sine distribution is chosen since only half of the wing is represented by the model, the other half is obtained by symmetry, so, along the spanwise direction the mesh will be more fine near the tip and more coarse near the root section.

The aerodynamic mesh is now defined through a convergence analysis (appendix C). The optimal mesh obtained is composed by 5 elements chordwise and 25 elements spanwise. That is the best compromise found to obtain a good data interpolation when data are imported into

Femap.
The obtained mesh can be seen in figure 7.13, where also the horseshoe vortices are highlighted as red lines.
Using this mesh the aerodynamics coefficients found are:

- $C_{L\ max} = 1.512$;
- $C_{L\ min} = -0.904$.

7.2.3 V-n diagram

Knowing the 3D aerodynamic lifting coefficients it is now possible to realize the V-n diagram.

Maneouvre diagram

First the true stall speeds are evaluated with 3D C_L values:

- $V_{S1} = 20.2\ m/s$;
- $V_{S1}^{1} = 26.2\ m/s$.

From the stall speeds V_a and V_g, design manoeuvring speeds, can be evaluated as:

$$V_a = V_{s1}\ \sqrt{n_1} \tag{7.3}$$

$$V_g = V_{s1}^{1}\ \sqrt{n_1^{1}} \tag{7.4}$$

Imposing a maximum load factor n_1 equal to 10 and a minimum load factor n_1^1 equal to -9:

- $V_a = 63.87\ m/s$;
- $V_g = 78.6\ m/s$.

The V_d, design maximum speed, is then imposed 115 m/s. This value is acceptable by means of the CS 22.3 [35], which prescribes a mandatory V_d of at least:

$$V_d > 3.5(\frac{W}{S}) + 200(km/h) \tag{7.5}$$

With $\frac{W}{S}$ expressed in daN/m^2.
In this case the minimum V_d would be equal to 93.7 m/s, so the imposed V_d is acceptable.

Gust diagram

For the realization of the gust diagram reference to the CS 22.3 [35] has been done. First the gust load is evaluated at V_b, the design gust speed, and V_d using the following relationship:

$$n = 1 \pm \frac{\frac{k}{2}\ \rho_0\ U\ V\ a}{\frac{m\ g}{S}} \tag{7.6}$$

where:
ρ_0: density air sea-level (kg/m^3);

U: gust velocity (m/s);
V: equivalent air speed (m/s);
a: slope of wing lift curve per radian;
m: mass of sailplane (kg);
g: acceleration due to gravity (m/s^2);
S: design wing area (m^2);
k: gust alleviation factor:
$k = \frac{0.96\frac{\mu}{H/l_m}}{0.475+\frac{\mu}{H/l_m}}$;
$\mu = \frac{2\frac{m}{S}}{\rho\ l_m\ a}$ (non dimensional sailplane mass ratio);
ρ: density of air (kg/m^3) at the altitude considered;
l_m: mean geometric chord of the wing;
H: length of the $(1-\cos)$ shaped gust:
$H = (12.17 + 0.191\mu)l_m$;

As prescribed by the CS 22 the design gust speed V_b must not be less than V_a, so V_b is imposed equal to 1.1 V_a.

The gust speeds prescribed by the CS 22 are $\pm 15\ m/s$ at V_b and $\pm 7.5\ m/s$ at V_d.

Using our sailplane characteristics the V-n diagram (fig. 7.14) is obtained. It was obtained through a parametric script in Octave (appendix B). The two sizing condition are therefor maximum load factor at V_a and minimum load factor at V_g.

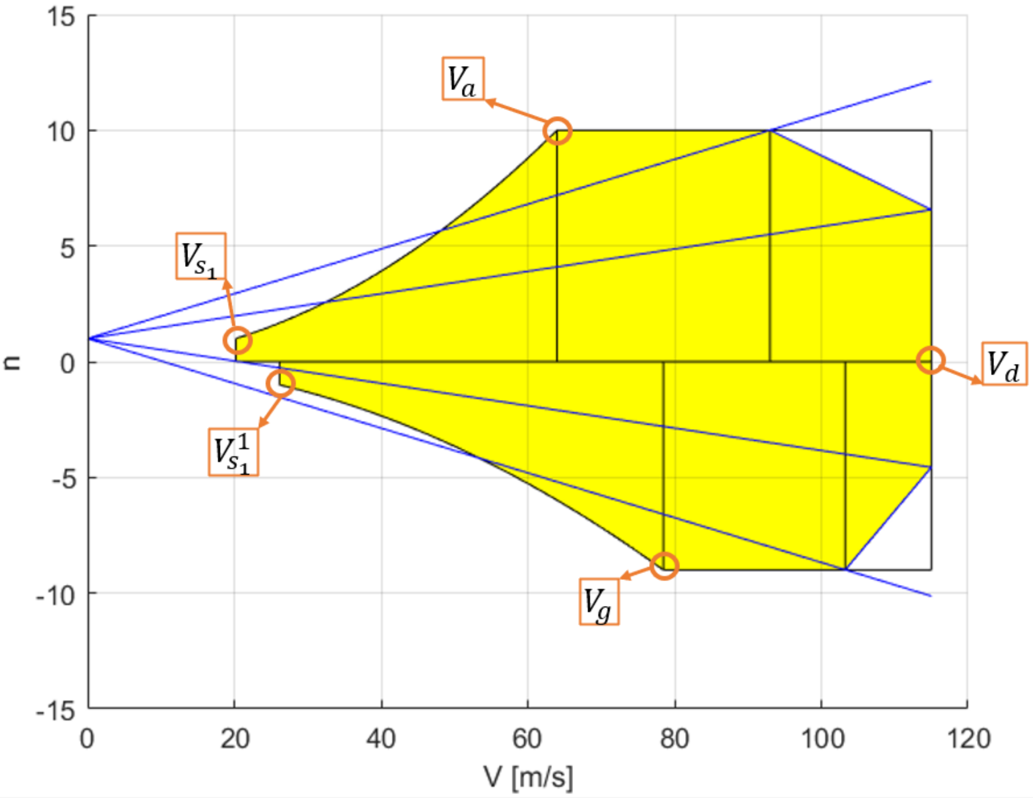

Figure 7.14: V-n diagram

7.2.4 Pressure on wing

Now that the sizing conditions are known it is necessary to evaluate pressure acting on the wing in these conditions. This is easily obtained by printing the elements loads in AVL, which give as an output dc_p. These dc_p are normalized pressure differentials between upper and lower surface of the panels sheet. By multiplying dc_p with dynamic pressure static pressures acting on the panel are obtained:

$$p = \frac{1}{2}\rho V^2 dc_p \tag{7.7}$$

An Octave script that converts dc_p in pressures in Femap data table format is written.
The data table is then imported in Femap and the data are interpolated from the aerodynamic mesh to the FEM mesh to the nearest load point. For the positive lift coefficient the data are interpolated on the upper surface of the wing, whereas for the negative lift coefficient to the lower surface.
For the case of V_a at maximum lift coefficient ($C_L = 1.512$) the obtained pressure surface is presented in figure 7.15. Then these pressure values are multiplied for a safety factor of 2.1.

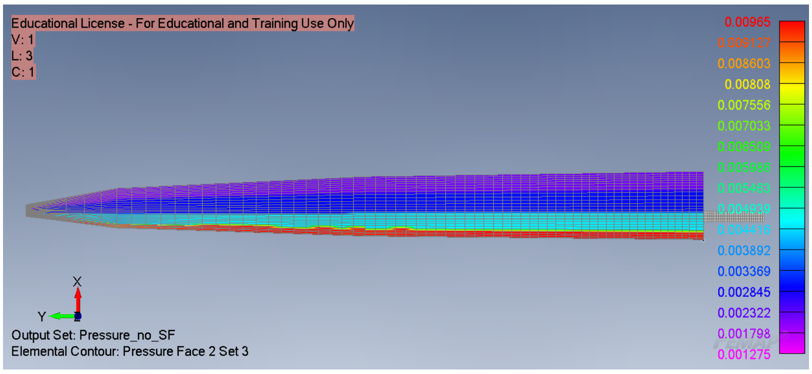

Figure 7.15: Pressure surface evaluated at V_a and $C_L = 1.512$ (values in MPa)

7.3 Sizing results

7.3.1 First results

As result of the sizing of the baseline wing the maximum thickness is obtained on the top flange of the wing box, with a lamination of 45 layers of $[+45/-45/0/0/0/0/0]$, with a thickness of nearly 32 mm. The thickness is gradually reduced along the spar in function of the stress. On the bottom flange of the wing box a lamination of 45 layers of $[+45/-45/0/0/0/0/]$ is obtained, with a thickness of 27.5 mm. On the box shear web a lamination 45 layers $[+45/-45]$ is imposed consistently to the flanges' lamination. With this lamination some failure index greater than 1 remains on the top flange and near the holes 7.16. The loaded zones near the holes are not concerning since in reality there will be present some reinforcement, which for the sake of simplicity are not represented in this simplified model. On the other hand the failure index on the top flange are not acceptable. Moreover, the thickness on that flange is a little too high, so a redesign of the main spar is executed.

On the wing skin some DD layers are added, with a maximum of 20 DDs of $[0/50/-$

50/0] obtained at the root section near the flanges. On the majority part of the wing 3 or 2 DD layers are enough to sustain the loads.

On the ribs and on the rear spar a foam Diab HT 61/81 6 mm thick is inserted in the middle $[+45/-45]$ layers. The HT 61 is a little less dense ($rho = 6.5\ 10^{-}5g/mm^3$) than the HT 81 ($rho = 8.5\ 10^{-}5g/mm^3$), but the HT 81 has got better mechanical properties. The material properties for the foams are taken via the data sheets of the producer [36]. In the tables 7.10 and 7.11 are presented respectively the 2D orthotropic properties inserted for the HT 61 and the HT 81.

Modulus		Value
E_1	=	80 MPa
E_2	=	80 MPa
ν_{12}	=	0.3
G_{12}	=	20 MPa
G_{1z}	=	20 MPa
G_{2z}	=	20 MPa

Table 7.10: Diab HT 61 equivalent 2D orthotropic material properties

Modulus		Value
E_1	=	105 MPa
E_2	=	105 MPa
ν_{12}	=	0.3
G_{12}	=	28 MPa
G_{1z}	=	28 MPa
G_{2z}	=	28 MPa

Table 7.11: Diab HT 81 equivalent 2D orthotropic material properties

Since also the foams are subject to the failure analysis, failure properties must be inserted in the foams material cards too. These are also taken from the data sheets and are presented in tables 7.12 and 7.13 respectively for the HT 61 and the HT 81.

	Direction 1	Direction 2
Tension	1.8 MPa	1.8 MPa
Compression	1 MPa	1 MPa
Shear	0.9 MPa	

Table 7.12: Diab HT 61 failure stress limits

	Direction 1	Direction 2
Tension	2.8 MPa	2.8 MPa
Compression	1.5 MPa	1.5 MPa
Shear	1.25 MPa	

Table 7.13: Diab HT 81 failure stress limits

On the rear spar a lamination with two layers of $[+45/-45]$ with HT 81 in the middle is enough to sustain the loads for all its length.

On the front part of the root rib 20 layers of $[+45/-45]$ with an HT 81 in the middle are needed.
On the rear part of the root rib only 14 layers of $[+45/-45]$ with in between HT 81 are needed.
On the first kink rib 8 layers of $[+45/-45]$ with a HT 81 in the middle are inserted.
On the second kink rib only 4 layers of $[+45/-45]$ with in between a HT 61 foam are enough.
On the tip rib the default single layer of $[+45/-45]$ is left without any foam.

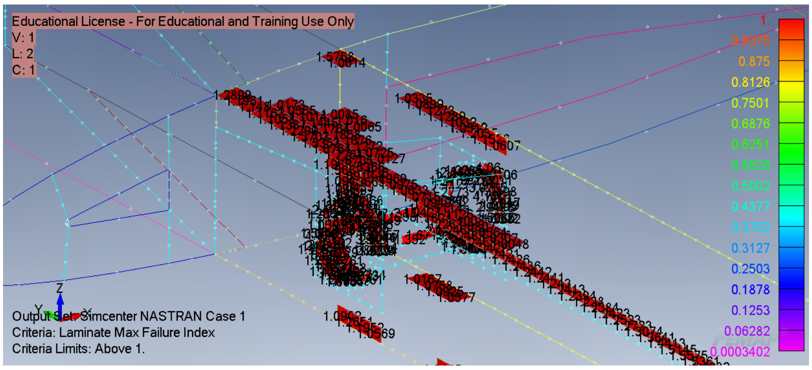
Educational License - For Educational and Training Use Only
V: 1
L: 2
C: 1
1.
0.9375
0.875
0.8126
0.7501
0.6876
0.6251
0.5626
0.5002
0.4377
0.3752
0.3127
0.2503
0.1878
0.1253
0.06282
0.0003402
Z
Y
Output Set: Simcenter NASTRAN Case 1
Criteria: Laminate Max Failure Index
Criteria Limits: Above 1.

Figure 7.16: $FI > 1$ on the wing

In figure 7.9 the different colours associated to the different properties can be seen on the top surface of the wing. It is clear how the main spar's flange reduces its thickness spanwise drastically. The skin results more thick near the main spar in the first section, with the light green associated to 8 DD layers lamination. The red part is associated with 4 DD layers, whereas the darker green is associated to 3 DD layers and the yellow to 2 DD layers.
With this lamination all the failure index remains under 1 on all the top surface (fig. 7.18).

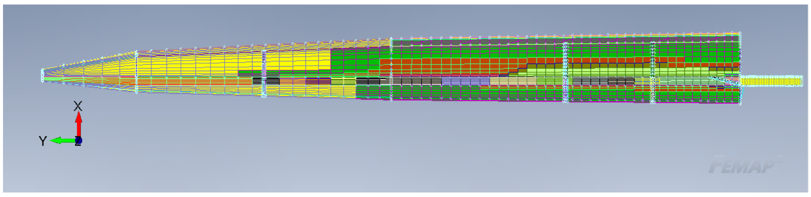

Figure 7.17: Properties on the upper surface of the wing

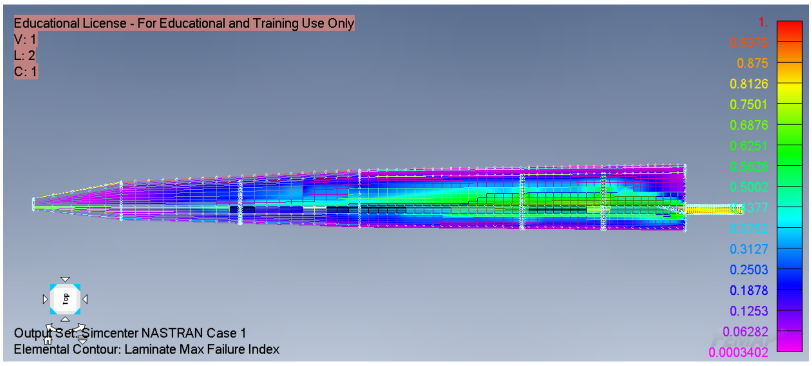
Educational License - For Educational and Training Use Only
V: 1
L: 2
C: 1
1.
0.9375
0.875
0.8126
0.7501
0.6876
0.6251
0.5626
0.5002
0.4377
0.3752
0.3127
0.2503
0.1878
0.1253
0.06282
0.0003402
Output Set: Simcenter NASTRAN Case 1
Elemental Contour: Laminate Max Failure Index

Figure 7.18: FI on the upper surface of the wing

7.3.2 Improvement in geometry

During the first sizing three more ribs are added to the geometry of the wing in order to improve its strength and stability properties:

- One rib at 25 % of distance between chord rib and first kink rib;
- One rib at 50 % of distance between chord rib and first kink rib;
- One rib at 50 % of distance between first kink rib and second kink rib.

The three ribs are holed relatively to their spanwise position, with a left thickness of:

- 27.5 mm for the first of the three;
- 25 mm for the second one;
- 19 mm for the latter.

The ribs are then imported into Femap and are inserted in the model as glued elements. The glue property allow to make in a permanent contact the added elements with the ones already present in order to not have to modify the mesh on the wing. The sizing process is then executed also for these ribs.

On the second rib (the one nearest to the root section) 6 layers of $[+45/-45]$ with HT 61 foam are inserted.

On the third rib (the one in the middle of the first section) 8 layers of $[+45/-45]$ with HT 81 in the middle are needed to sustain the loads.

On the last rib 6 layers of $[+45/-45]$ with HT 61 foam are needed.

Since on the box upper flange the thickness of the lamination is a little too high and failure index still remains greater than one the thickness of the main spar's flanges are increased to 100 mm at the root section. The width remain 100 mm till the first kink, then it reduces gradually to 80 mm to the second kink. After the first the second kink the width of the flange remains the same as before. To allow this enlargement of the flange the spar shear web is moved from 30% of the chord to 33% of chord.

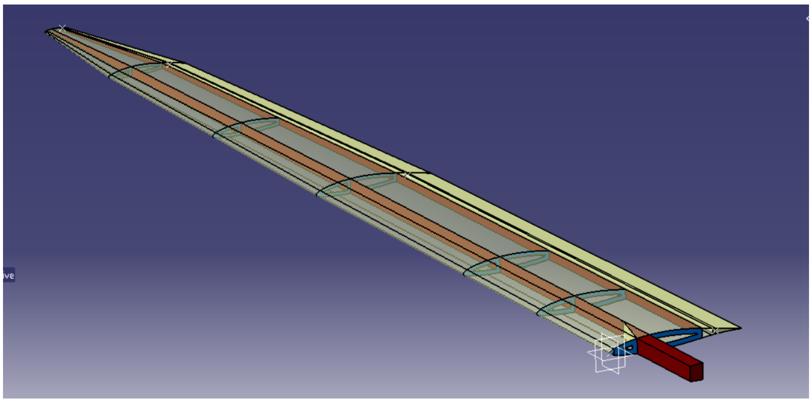

Figure 7.19: Geometry with the three new ribs added

7.3.3 Final sizing

Following the enlargement of the main spar's flanges the stresses on the flanges, and therefor the failure index decrease substantially. This allows to reduce the thickness of the flanges both on the wing box and on the wing spar, managing at the same time to not have almost anymore failure index greater than 1. The only zones with failure index greater than one that remains are near the holes, which, as said before, are not concerning, and near the vertices of the box (fig. 7.20). The latter are due to stress concentration due to the rectangular shape of the wing box section and are acceptable since in an hypothetical real wing these zones can be rounded to reduce the stress.

The maximum thickness obtained on the top flange of the wing box is 27.5 mm, with a lamination of 45 $[45/-45/0/0/0/0]$. The thicknesses obtained on the TOP surface can be seen in figure 7.22.

By enlarging the flanges also the skin takes now less loads, so that is thinned too. As can be seen in figure 7.21 now the wing top surface is composed almost with only 2 layers of DD (yellow part) everywhere. Now a sizing at V_g with a load factor of -9 g and a factor of safety of 2.1 is executed in order to sizing properly also the bottom surfaces of the wing. The obtained thicknesses on the bottom surface are presented in figure 7.23. The maximum thickness on the bottom surface is located on the wing box flange, with a thickness of 23.3 mm and a lamination of $[45/-45/0/0/0]$ repeated 45 times.

The failure index obtained in the most critical condition for the upper surface and the bottom surface are presented in figure 7.24 and 7.25. As can be seen, failure index reach values near one, but remains under one on all the wing. This indicates that the sizing has been executed properly.

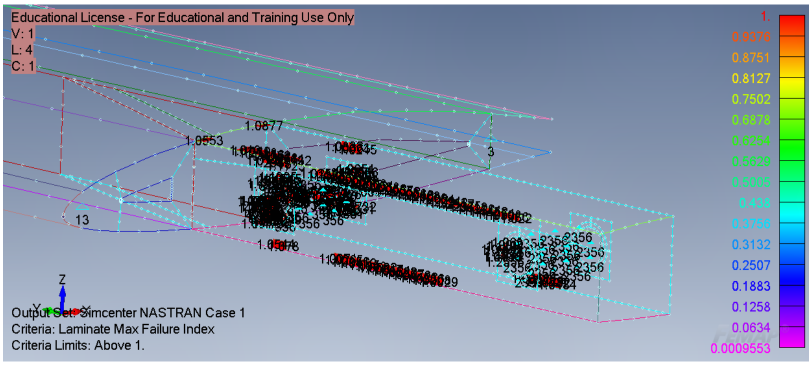
Educational License - For Educational and Training Use Only
V: 1
L: 4
C: 1
1.0877
1.0553
13
3
Z
X
Y
Output Set: Simcenter NASTRAN Case 1
Criteria: Laminate Max Failure Index
Criteria Limits: Above 1.
1.
0.9376
0.8751
0.8127
0.7502
0.6878
0.6254
0.5629
0.5005
0.438
0.3756
0.3132
0.2507
0.1883
0.1258
0.0634
0.0009553

Figure 7.20: $FI > 1$ on the wing with larger flanges

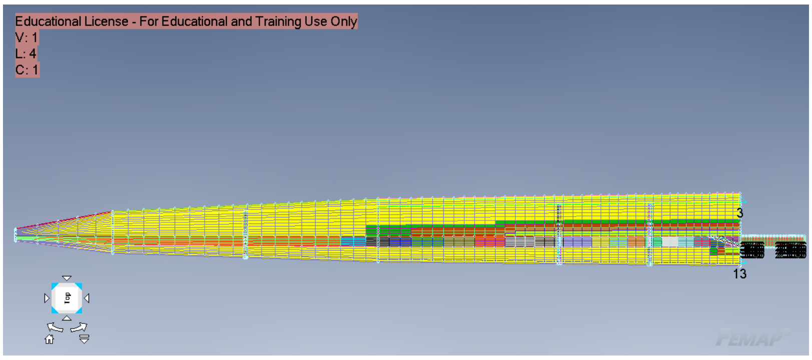
Educational License - For Educational and Training Use Only
V: 1
L: 4
C: 1
3
13
FEMAP

Figure 7.21: Properties on the upper surface of the wing with larger flanges

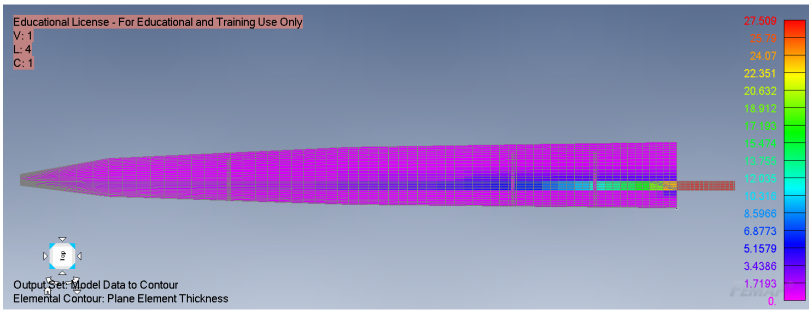
Educational License - For Educational and Training Use Only
V: 1
L: 4
C: 1
27.509
25.79
24.07
22.351
20.632
18.912
17.193
15.474
13.755
12.035
10.316
8.5966
6.8773
5.1579
3.4386
1.7193
0.
FEMAP

Output Set: Model Data to Contour
Elemental Contour: Plane Element Thickness

Figure 7.22: Contour of thickness on top surface

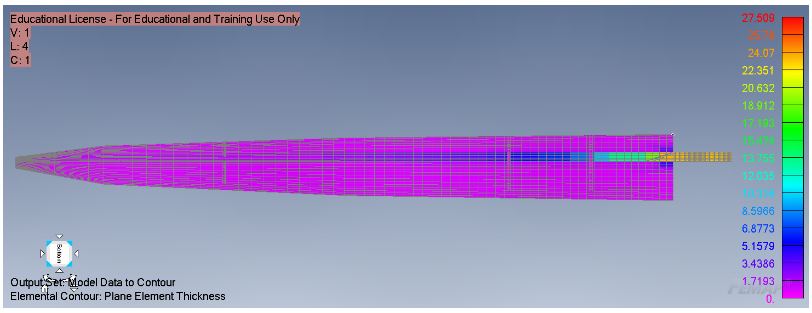
Educational License - For Educational and Training Use Only
V: 1
L: 4
C: 1
27.509
25.79
24.07
22.351
20.632
18.912
17.193
15.474
13.755
12.035
10.316
8.5966
6.8773
5.1579
3.4386
1.7193
0.
FEMAP

Output Set: Model Data to Contour
Elemental Contour: Plane Element Thickness

Figure 7.23: Contour of thickness on bottom surface

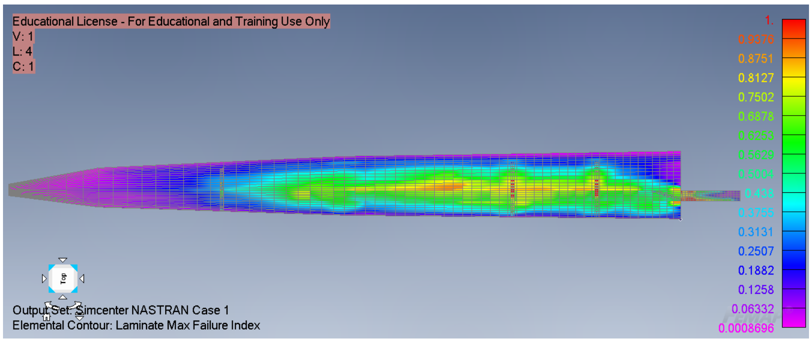
Educational License - For Educational and Training Use Only
V: 1
L: 4
C: 1
1.
0.9376
0.8751
0.8127
0.7502
0.6878
0.6253
0.5629
0.5004
0.438
0.3755
0.3131
0.2507
0.1882
0.1258
0.06332
0.0008696
FEMAP

Output Set: Simcenter NASTRAN Case 1
Elemental Contour: Laminate Max Failure Index

Figure 7.24: FI on upper surface

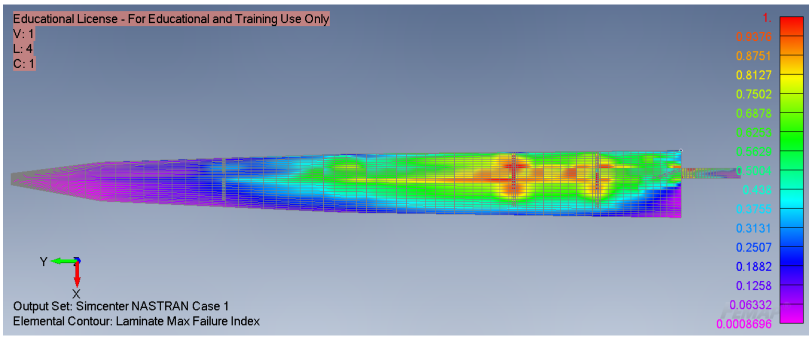
Educational License - For Educational and Training Use Only
V: 1
L: 4
C: 1
Y
X
Output Set: Simcenter NASTRAN Case 1
Elemental Contour: Laminate Max Failure Index
1.
0.9376
0.8751
0.8127
0.7502
0.6878
0.6253
0.5629
0.5004
0.438
0.3755
0.3131
0.2507
0.1882
0.1258
0.06332
0.0008696
FEMAP

Figure 7.25: FI on bottom surface

Chapter 8

Modal analysis

With the wing now sized properly the first step to be done before executing the flutter analysis is a modal analysis. Calling a modal analysis (Nastran SOL 103) the solver solves an eigenvalue problem extracting the lowest N eigenvalue and eigenvectors (with N selected by the user) from the following problem:

$$(-M\omega^2 + K)\overline{U} = 0 \tag{8.1}$$

With:
M: mass matrix;
ω: eigenvalues (angular frequencies);
K: stiffness matrix;
$\bar{U}$: eigenvector (modal shapes).

By solving the characteristic polynomial it is easy to find the natural frequencies:

$$f = \frac{\omega}{2\pi} \tag{8.2}$$

The frequencies associated with their modal shapes will then be the input for the flutter analysis, as these modes will interact with aerodynamic flow damping or amplifying the oscillations.

Executing some preliminary modal analysis it was understood that some more ribs were needed, as the modal shapes were strongly stained by internal deformation modes, due to having too large skin panels. To prevent this phenomenon to occur more ribs has been inserted. The final configuration of the wing is composed with 14 ribs, 1 at the root section, 7 equally spaced spanwise between the root section and the first kink, one at the first kink, 3 equally spaced between the first kink and second kink, one at the second kink and finally one rib at the wing tip (fig 8.1).

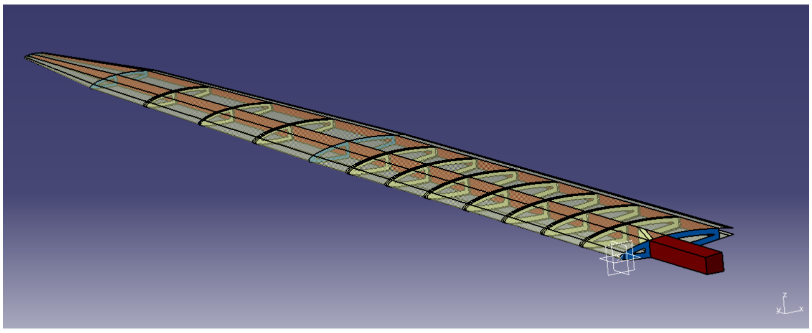

Figure 8.1: Final configuration of the wing

8.1 Normal modes and natural frequencies

Setting up a modal analysis the first 20 modes are requested. Here in table 8.1 is presented a description of the first 7 modes, with their natural frequencies:

Mode	Type	frequency [Hz]
1	Bending	5.04
2	Inplane	7.98
3	Bending	18.19
4	Bending	41.13
5	Torsion	53.77
6	Inplane	54.35
7	Bending	68.44

Table 8.1: Wing modes and associated frequencies

The associated modal shapes are presented from figure 8.2 to 8.8.

From the seventh mode on, all the modes are dirtied by internal deformation modes due to the wing's trailing edge deflection and would not be greatly interesting to the analysis purposes. Their frequencies span from 70 Hz to 85 Hz. This high deformation in the trailing edge is due to the fact that this part of the wing is a free edge part and results to be an open section, therefore has got more freedom to vibrate. Modal shapes 8 and 9 are reported in figure 8.9 as an example.

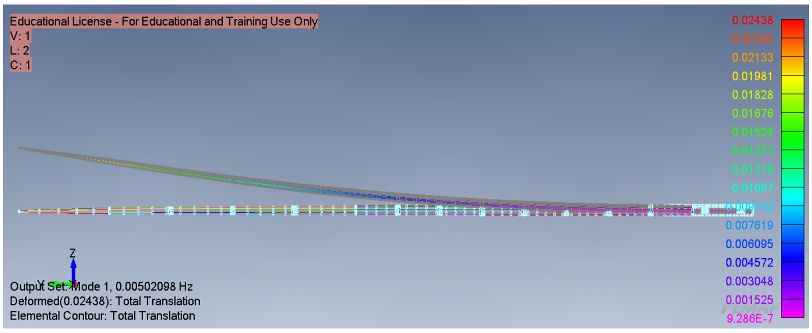
Educational License - For Educational and Training Use Only
V: 1
L: 2
C: 1

Output Set: Mode 1, 0.00502098 Hz
Deformed(0.02438): Total Translation
Elemental Contour: Total Translation

0.02438
0.02285
0.02133
0.01981
0.01828
0.01676
0.01524
0.01371
0.01219
0.01067
0.009142
0.007619
0.006095
0.004572
0.003048
0.001525
9.286E-7
Z
Y
X

Figure 8.2: Mode 1, $f = 5.04\ Hz$

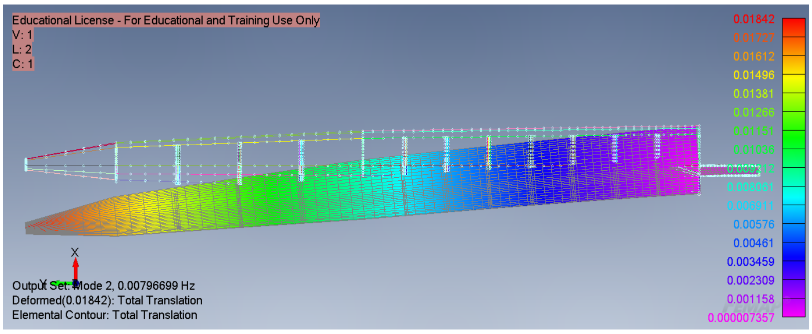
Educational License - For Educational and Training Use Only
V: 1
L: 2
C: 1
X
Output Set: Mode 2, 0.00796699 Hz
Deformed(0.01842): Total Translation
Elemental Contour: Total Translation
0.01842
0.01612
0.01496
0.01381
0.01266
0.00576
0.00461
0.003459
0.002309
0.001158
0.000007357

Figure 8.3: Mode 2, $f = 7.98\ Hz$

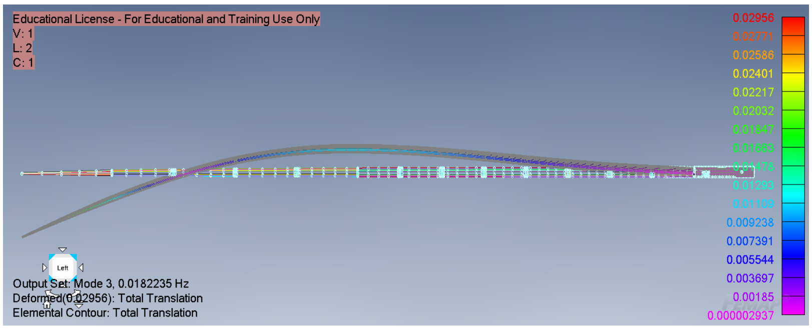
Educational License - For Educational and Training Use Only
V: 1
L: 2
C: 1
Left
Output Set: Mode 3, 0.0182235 Hz
Deformed(0.02956): Total Translation
Elemental Contour: Total Translation
0.02956
0.02586
0.02401
0.02217
0.02032
0.009238
0.007391
0.005544
0.003697
0.00185
0.000002937

Figure 8.4: Mode 3, $f = 18.19\ Hz$

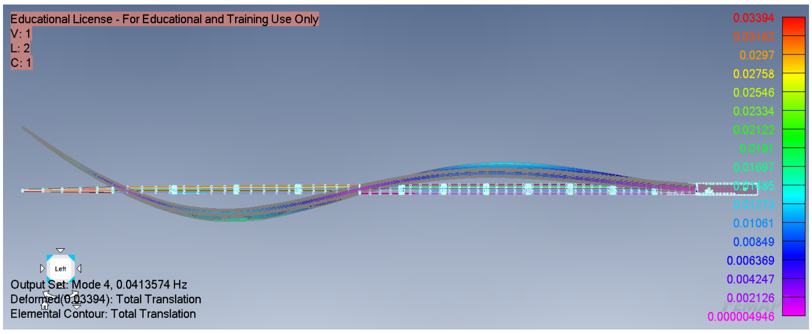
Educational License - For Educational and Training Use Only
V: 1
L: 2
C: 1
Left
Output Set: Mode 4, 0.0413574 Hz
Deformed(0.03394): Total Translation
Elemental Contour: Total Translation
0.03394
0.0297
0.02758
0.02546
0.02334
0.01061
0.00849
0.006369
0.004247
0.002126
0.000004946

Figure 8.5: Mode 4, $f = 41.13\ Hz$

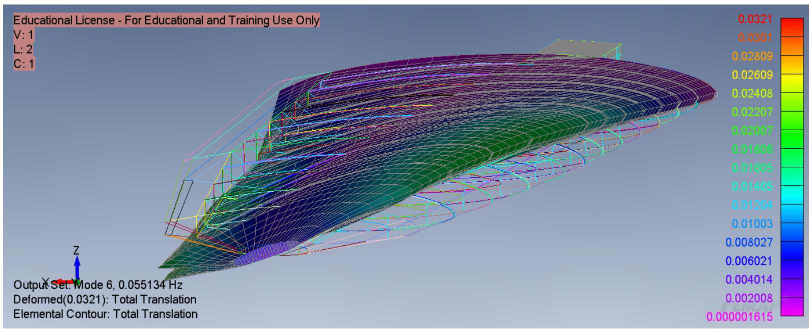
Educational License - For Educational and Training Use Only
V: 1
L: 2
C: 1
Z
Output Set: Mode 6, 0.055134 Hz
Deformed(0.0321): Total Translation
Elemental Contour: Total Translation
0.0321
0.02809
0.02609
0.02408
0.02207
0.01003
0.008027
0.006021
0.004014
0.002008
0.000001615

Figure 8.6: Mode 5, $f = 53.77\ Hz$

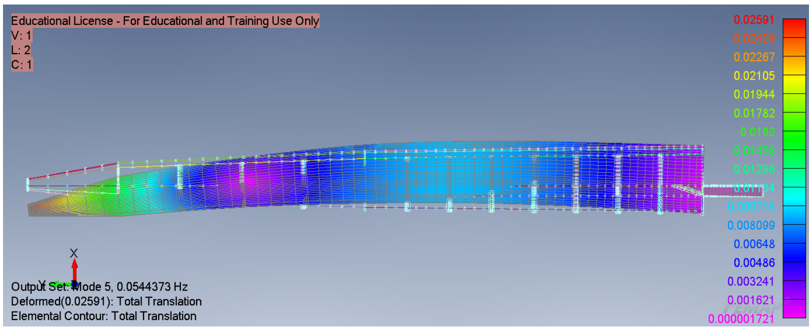
Educational License - For Educational and Training Use Only
V: 1
L: 2
C: 1
X
Y
Output Set: Mode 5, 0.0544373 Hz
Deformed(0.02591): Total Translation
Elemental Contour: Total Translation
0.02591
0.02429
0.02267
0.02105
0.01944
0.01782
0.0162
0.01458
0.01296
0.01134
0.009718
0.008099
0.00648
0.00486
0.003241
0.001621
0.000001721

Figure 8.7: Mode 6, $f = 54.35\ Hz$

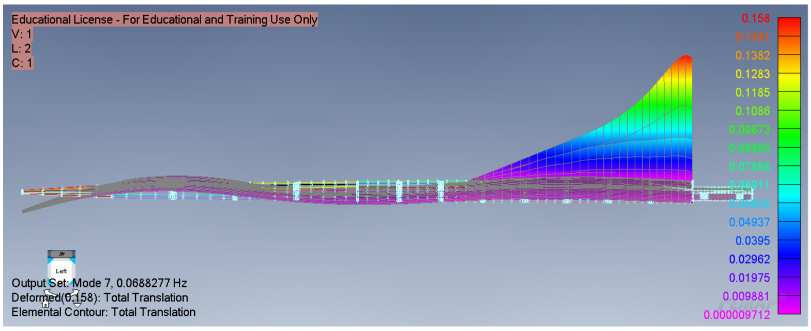
Educational License - For Educational and Training Use Only
V: 1
L: 2
C: 1
Left
Output Set: Mode 7, 0.0688277 Hz
Deformed(0.158): Total Translation
Elemental Contour: Total Translation
0.158
0.1481
0.1382
0.1283
0.1185
0.1086
0.09873
0.08885
0.07898
0.06911
0.05924
0.04937
0.0395
0.02962
0.01975
0.009881
0.000009712

Figure 8.8: Mode 7, $f = 68.44\ Hz$

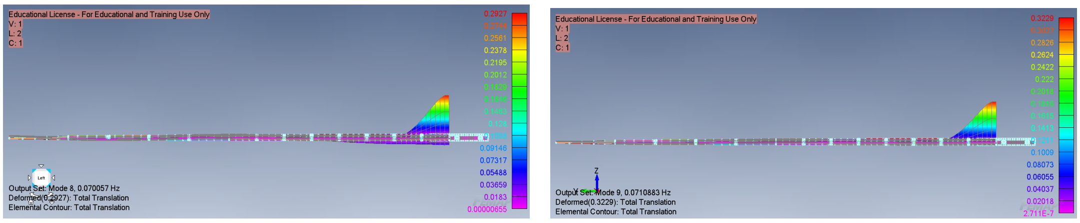
Educational License - For Educational and Training Use Only
V: 1
L: 2
C: 1
Left
Output Set: Mode 8, 0.070057 Hz
Deformed(0.2927): Total Translation
Elemental Contour: Total Translation
0.2927
0.2744
0.2561
0.2378
0.2195
0.2012
0.1829
0.1646
0.1463
0.128
0.1098
0.09146
0.07317
0.05488
0.03659
0.0183
0.00000655
Educational License - For Educational and Training Use Only
V: 1
L: 2
C: 1
Z
Y
Output Set: Mode 9, 0.0710883 Hz
Deformed(0.3229): Total Translation
Elemental Contour: Total Translation
0.3229
0.3027
0.2826
0.2624
0.2422
0.222
0.2018
0.1816
0.1615
0.1413
0.1211
0.1009
0.08073
0.06055
0.04037
0.02018
2.711E-7

(a) Mode 8

(b) Mode 9

Figure 8.9

8.2 Results comparison with analytic model

The evaluated modes in the previous paragraph can be compared with analytic results. In fact, for uniform cantilever beam a close solution to evaluate the first modes can be found. The model in exam in this thesis is not, of course, a uniform beam, but comparing the results can give an idea about the correctness of the FEM model.

For a cantilever beam subjected to free vibration, and the system is considered as continuous system in which the beam mass is considered as distributed along with the stiffness of the shaft, the free vibration equation is [37]:

$$\frac{d^4Y(x)}{dx^4} - \beta^4 Y(x) = 0 \tag{8.3}$$

With:

$$\beta^4 = \frac{\omega^2 m}{EI} \tag{8.4}$$

Where:
$Y(x)$: transversal displacement;
x: beam axis coordinate;
m: mass of the cantilever beam;
ω: angular frequency;
E: stiffness modulus of the beam;
I: moment of inertia of the beam;

By imposing the correct boundary conditions:

$$\begin{cases} x = 0, \; Y(x) = 0, \; \frac{dY(x)}{dx} = 0 \\ x = L, \; \frac{d^2Y(x)}{dx^2} = 0, \; \frac{d^3Y(x)}{dx^3} = 0 \end{cases} \tag{8.5}$$

A close form for the bending angular frequencies can be found [37]:

$$f_{bi} = \frac{\alpha^2}{2\pi}\sqrt{\frac{EI}{\rho A L^4}} \tag{8.6}$$

Where, for the first three modes, $\alpha = 1.875, 4.694, 7.855$.
The first three associated bending modal shapes are presented in figure 8.10.
For the torsional modes the following relation is valid:

$$f_{ti} = \frac{2i-1}{4L}\sqrt{\frac{GJ}{\rho I_p}} \tag{8.7}$$

For our beam model inertia moduli and area of the cross section have been evaluated at the section put at 50% of wing's span; the Young's and shear moduli have been evaluated for an equivalent isotropic material of the composite used (as it was all laminated with a $[0/45/-45/90]_s$ lamination), obtaining the following values:

- $A = 1.241\ 10^{-3}\ m^2$;

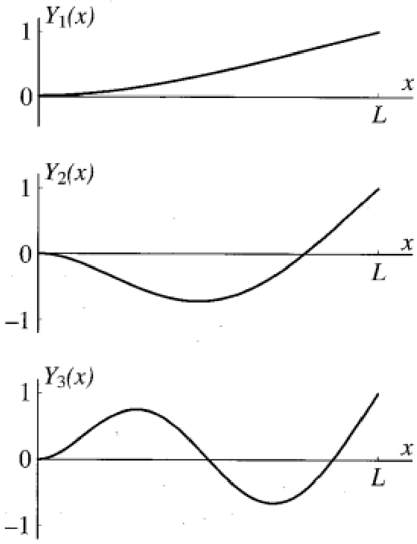

Figure 8.10: Analytic first three bending modal shapes [37]

- $E = 39749\ MPa$;
- $G = 13035\ MPa$;
- $I_1 = 1.87\ 10^{-6}\ m^4$;
- $I_2 = 3.31\ 10^{-5}\ m^4$
- $I_p = 1.00\ 10^{-6}\ m^4$;
- $J = 3.00\ 10^{-7}\ m^4$
- $L = 6.75\ m$

The previous values have been evaluated by importing in Femap a cross section placed in $y = 3.375\ m$ with its skin and spar laminate thickness. The software, in fact, has got an automatic calculator for inertia and other beam properties. Since the calculator needed a thickness of at least 4 mm some of the evaluated values would not have been accurate, as the thickness of the skin there is well under 4 mm. Therefor, a Matlab code based on a semimonocoque model and colloborant areas has been created to correct data regarding inertia areas and concentrated areas values. The simplified semimonocoque model used is presented in figure 8.11. The amount of concentrated area due to every section component is defined depending on the major load condition of the component. For every 2D panel, if b is the width and t is the thickness, for:

- Uniaxial stress (horizontal elements), $A = \frac{bt}{2}$;
- Bending (vertical elements), $A = \frac{bt}{6}$.

Having corrected the inertia areas values, the major uncertainty remains on the torsional constant value J, as the value evaluated by Femap is left there.

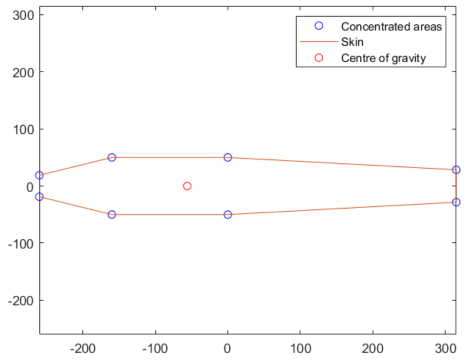

Figure 8.11: Semimonocoque model for cross section

The obtained results in comparison with what has been found through the FEM model are listed in table 8.2. From the table it can be seen that the values found with the FEM model do not differ much from the analytical ones, with the exception of the first bending. The main differences are due to the fact that mass distribution, geometry and inertia spanwise along the wing are not constant, as it is assumed by the analytical beam model and, moreover, some uncertainties are present in the evaluation of the inertia values. The associated modal shapes found with the FEM model (both for bending and inplane modes) match almost perfectly with the ones predicted by the analytical theory (fig. 8.10). Therefor, this is a confirmation of the reliability of the FEM model.

Mode	Type	Wing fr. [Hz]	Beam fr. [Hz]
1	Bending	5.04	2.43
2	Inplane	7.98	10.22
3	Bending	18.19	15.24
4	Bending	41.13	42.67
5	Torsion	53.77	59.21
6	Inplane	54.35	64.07

Table 8.2: Comparison between beam analytic model and wing's FEM model frequencies

8.3 Results comparison with a FEM equivalent beam model

To have an even more accurate confirmation of the goodness of the wing's FEM model a comparison with an equivalent beam model has been executed.

To obtain a piecewise tapered beam six section and their respective properties have been imported into Femap. The spanwise coordinate of each imported section is 0 mm, 280 mm, 735 mm, 1390 mm, 2500 mm, 3750 mm, 5000 mm, 6000 mm. Showing the cross section, the obtained beam is presented in figure 8.12. A boundary condition with every degree of freedom fixed is imposed at the root node.

With this model it was possible to catch quite accurately the bending modes. By now accounting a piecewise tapering of the beam, the first three bending modes match pretty well with the original wing FEM model, as it can be seen in table 8.3, in support of the fact that the

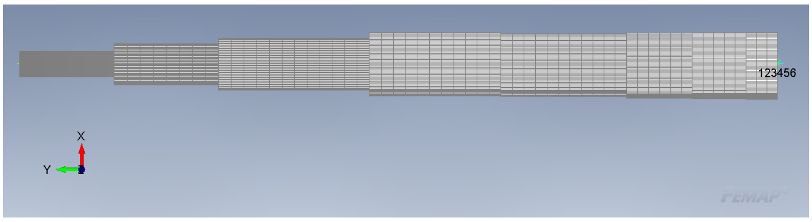
123456
X
Y
FEMAP

Figure 8.12: Equivalent beam

discrepancy between the analytical first bending frequency and the wing model was mainly due to the wing's tapering. Moreover, taking a look to the equivalent beam bending modal shapes they are almost identical to the wing's ones (fig. 8.13 & 8.2, 8.14 & 8.4, 8.15 & 8.5).

Mode	Analytical	Eq. beam	Wing
First bending	2.4 Hz	5.7 Hz	5.02 Hz
Second bending	15.2 Hz	20.0 Hz	18.22 Hz
Third bending	42.7 Hz	41.8 Hz	41.36 Hz

Table 8.3: Comparison of beam analytic model, equivalent beam model and wing model frequencies

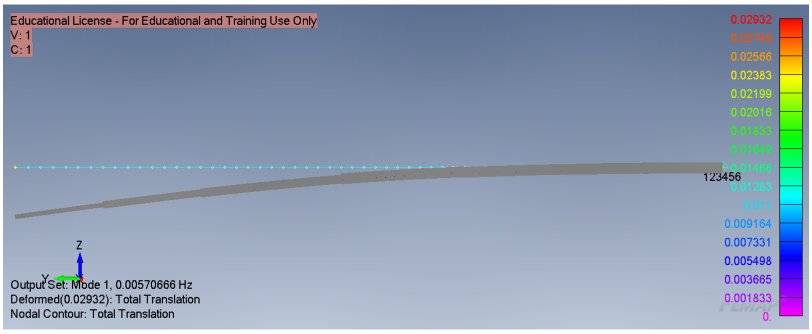
Educational License - For Educational and Training Use Only
V: 1
C: 1
123456
Z
Y
Output Set: Mode 1, 0.00570666 Hz
Deformed(0.02932): Total Translation
Nodal Contour: Total Translation
0.02932
0.02749
0.02566
0.02383
0.02199
0.02016
0.01833
0.01649
0.01466
0.01283
0.011
0.009164
0.007331
0.005498
0.003665
0.001833
0.
FEMAP

Figure 8.13: Equivalent beam first bending

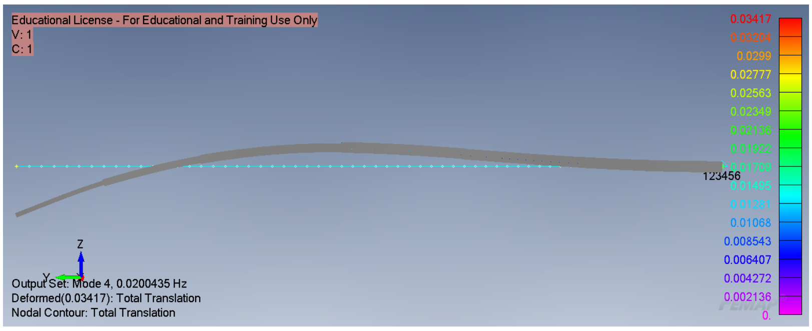

Educational License - For Educational and Training Use Only
V: 1
C: 1

Output Set: Mode 4, 0.0200435 Hz
Deformed(0.03417): Total Translation
Nodal Contour: Total Translation

0.03417
0.03204
0.0299
0.02777
0.02563
0.02349
0.02136
0.01922
0.01709
0.01495
0.01281
0.01068
0.008543
0.006407
0.004272
0.002136
0.
123456
Z
Y
FEMAP

Figure 8.14: Equivalent beam second bending

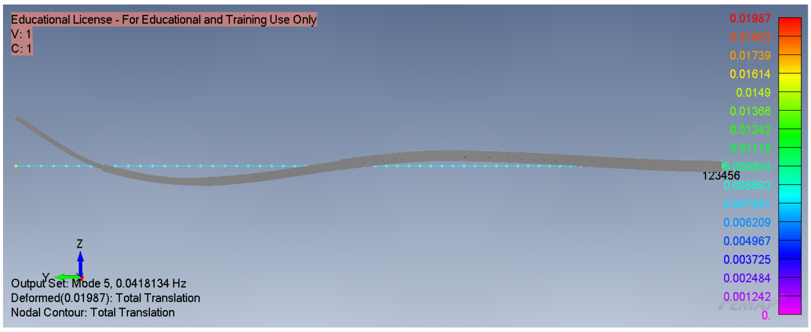

Educational License - For Educational and Training Use Only
V: 1
C: 1

Output Set: Mode 5, 0.0418134 Hz
Deformed(0.01987): Total Translation
Nodal Contour: Total Translation

0.01987
0.01863
0.01739
0.01614
0.0149
0.01366
0.01242
0.01118
0.009934
0.008693
0.007451
0.006209
0.004967
0.003725
0.002484
0.001242
0.
123456
Z
Y
FEMAP

Figure 8.15: Equivalent beam third bending

Chapter 9

Flutter analysis

Having identified the first six modes as the more significant ones, it is now time to perform the flutter analysis. To set a flutter analysis is necessary to create an aerodynamic mesh from which the solver, using DLM, can take the aerodynamic pressures. The imposed deformation on the aerodynamic panels is evaluated thanks to a splining process that transfer deformations from FEM nodes due to the modal shapes to the aerodynamic panels' control points. Then the loads on the aerodynamic panels are evaluated through DLM at the load points and are transferred back again to the FEM mesh again with a spline interpolation. Then the generalized aerodynamic matrix is evaluated and thanks to p-k method the stability analysis is performed.

The solver used to perform the flutter analysis is MSC Nastran. The specific flutter method used will be the PKNL method, which is a variant of the p-k method with no looping. In this method, the number of entries in the FLFACT data for density ratios, Mach numbers, and velocities need to be the same and the eigenvalue extraction is carried out at each linear selection of density ratio, Mach number, and velocity. This reduces much the computational costs without affecting much the results accuracy, especially considering constant density ratio and Mach number.

9.1 Aerodynamic mesh

The aerodynamic mesh was created using three set of flat plates, one for each section between wing's kinks. The leading edge of the plates corresponds to the leading edge of the wing. The total length of the plates' surface is then obtained giving as input the chord length of the wing at the edge sections. The optimal discretizion was obtained through a convergence analysis (appendix D). The best configuration obtained (fig. 9.1) is composed with 25 panels in spanwise direction: 10 equally spaced between root section and first kink, 10 equally spaced between first and second kink and 5 equally spaced between second kink and tip. The mesh in the chordwise direction is composed by ten elements distributed in bias way with a bias factor of 5, obtaining a mesh thinner near the leading and trailing edges. These thinner elements towards leading and trailing edge allows to obtain more precise results compared to using an uniform mesh.

With this discretization there are not elements with excessive aspect ratio and, moreover, by increasing further the number of elements flutter results don't change much (there is a 3% variation in respect with a mesh composed by 15 chordwise elements and 60 spanwise elements).

Then a CAERO1 property (to perform DLM) is associated to the panels and three surface splines are associated to the three sections of aerodynamic panels and the respective structural nodes placed on the wing top surface are set up.

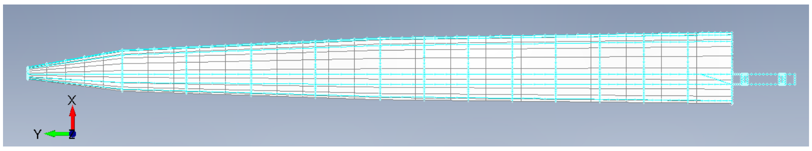

Figure 9.1: Aerodynamic mesh

9.2 Analysis settings

Before performing the flutter analysis some important settings must be passed to the solver.

The complex solution method selected is the complex Lanczos, with a number of six desired eigenvalues to extract.

The mean aerodynamic chord is set to 667 mm and the reference density to 1.225 10^{-12} g/mm^3, consistently with the units used in the model.

The velocities where to perform the stability analysis are set to 500, equally spaced between 10 m/s and 300 m/s.

The Mach numbers associated to the velocities are all set to 0. This is coherent to the mathematical model, which uses DLM and PKNL and also to the purposes of the sailplane from which the wing is taken, as its maximum speed evaluated from the envelope diagram is 115 m/s, which is fully subsonic and incompressible ($M \simeq 0.3$). Thus, if the flutter speed is below the V_d it will be captured faithfully by the model without any imposed compressibility correction. If the flutter speed is found at higher Mach number it will be influenced by some compressibility error, but there is the certainty that it will not fall into the envelope diagram. Moreover, for the analysis of the relationship between Tsai's Modulus and the flutter behaviour it is better to leave Mach number equal to zero, as in this way there won't be captured any non-linearity due to the air compressibility.

Then, since we are not interested in analyzing flutter behaviour at different altitudes, the density ratio are imposed to one.

Finally, in the MKAERO card the starting k values that the solver uses to evaluate the aerodynamic matrix are imposed as it follows:

```
MKAERO1 0.                                                              +MK
+MK     0.001   0.05    0.10    0.20    0.50    1.0     2.0     5.0     +MK
+MK     10.0    20.0    50.0
```

9.3 Results

The output from Nastran is read with a Matlab script that converts numerical values into graphs: frequencies vs velocities and damping vs velocities (fig. 9.2).

First, it can be seen that the modes' frequencies at low speed match almost perfectly the ones evaluated with the modal analysis (table 8.1), with the blue line associated to the first mode, the orange line to the second, the yellow line to the third, the purple line to the fourth, the green line to the fifth and the light blue line to the sixth. Then, the damping of every mode starts at low speed with negative values, as it would be expected.

By analyzing more in detail the graphs it can be seen that the first mode whose damping becomes positive is the fifth, namely the torsional mode, at a speed of:

$$V_f = 199.9\ m/s \tag{9.1}$$

That is much more than the minimum flutter velocity prescribed by the CS 22 of 1.2 V_D, that in this case corresponds to 138 m/s. Therefor, from the analysis it appears the wing is free from any danger of flutter in all its flight conditions.

From the frequencies vs velocity graph it can be seen that in correspondence of the flutter speed the torsional mode (purple line) merges almost perfectly with the third bending mode (green line), as their frequencies assume almost identical values. By looking at the flutter modal shape (fig. 9.3) this is confirmed, as the torsional mode is dirtied by the third bending mode. This merging phenomenon is well known in literature and it occurs near the flutter establishment speed very often, as flutter is generally induced by flexural-torsional coupled oscillations.

Another interesting phenomenon that can be noted from the graphs is that the first mode and the third mode become strongly damped respectively from 54 m/s and 261.6 m/s and their frequency become zero. Then, from 213.5 m/s the damping of the first mode become positive, with an associated frequency that remain zero. This occur when the wing encounters the divergence phenomenon, as the static deformation of the wing induced by aerodynamic loads cannot be countered anymore by the wing stiffness, and the wing reaches a theoretically infinite deformation. Practically this is a destructive configuration that led to the failure of the wing. Therefor, the previously cited velocity is the divergence speed of the wing model:

$$V_d = 213.5 m/s \tag{9.2}$$

Last, it is interesting to note that inplane modes (orange and light blue lines) don't interact by any means with the aerodynamic flow, as their frequency is constant with velocity and their damping is almost zero.

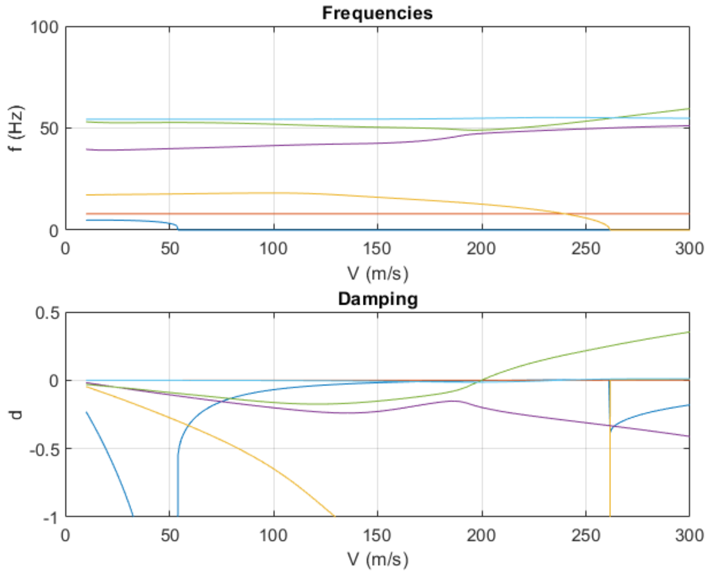

Figure 9.2: Frequencies and damping vs velocities

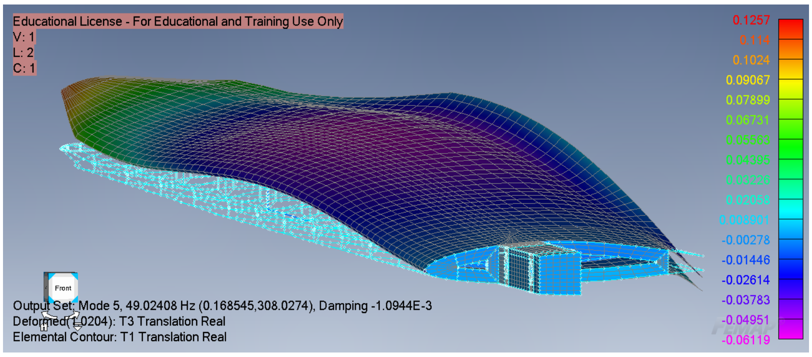
Educational License - For Educational and Training Use Only
V: 1
L: 2
C: 1
Front
0.1257
0.114
0.1024
0.09067
0.07899
0.06731
0.05563
0.04395
0.03226
0.02058
0.008901
-0.00278
-0.01446
-0.02614
-0.03783
-0.04951
-0.06119
FEMAP

Output Set: Mode 5, 49.02408 Hz (0.168545,308.0274), Damping -1.0944E-3
Deformed(1.0204): T3 Translation Real
Elemental Contour: T1 Translation Real

Figure 9.3: Flutter modal shape, $f = 49.0\ Hz$

Chapter 10

Parametric analysis and results

After having build, sized and then performed a flutter analysis on a wing model, it can be used to execute some parametric analysis. The first analysis will evaluate wing's aeroelastic behaviour as function of the position of the main spar. Then a second analysis will be executed to evaluate the relationship between the aeroelastic behaviour of the wing and the value of the material's Tsai's Modulus. It must be remembered that the wing model used to perform the two analysis is all composed with the same fiber reinforced composite material, parameterized in function of Tsai's Modulus (chapter 7.1.2).

10.1 Aeroelastic behaviour by varying the position of the main spar

To evaluate wing's aeroelastic behaviour by changing the position of the main spar three new models are created in addition to the one used up to this point. The four models differs only for the location of the main spar, which is located respectively for each model at:

- 33% of chord;
- 37% of chord;
- 43% of chord;
- 47% of chord.

The mesh on the models is executed in order to be the more similar possible to the original model. The materials, properties and boundary conditions assigned to the various models are exactly the same. The aerodynamic mesh and splines are also executed in the same way as described in chapter 9.1.

By drawing back the main spar position the elastic line and center of mass will consequently draw back in turn. In particular, by moving back the elastic line divergence velocity should decrease in a quasi-hyperbolic way, as

$$U_d \propto \frac{1}{\sqrt{x_0 - x_{ac}}} \tag{10.1}$$

Where:
x_0: chordwise position of the elastic line;
x_{ac}: chordwise position of the aerodynamic centre.
Moreover, this shift of the elastic line towards the trailing edge should determine a reduction in the flutter speed.

The computed frequencies and damping diagrams obtained for the four configurations are presented respectively in figures 10.1, 10.2.

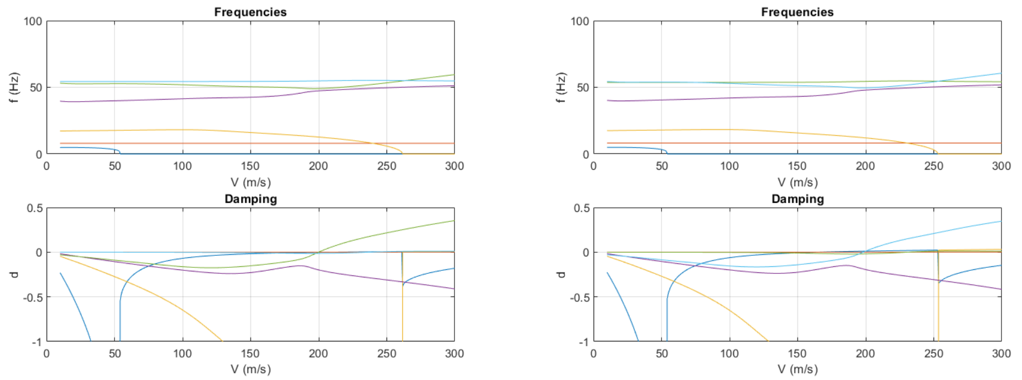

(a) spar position: 33 % of chord

(b) spar position: 37 % of chord

Figure 10.1: Frequencies and damping vs velocities diagrams

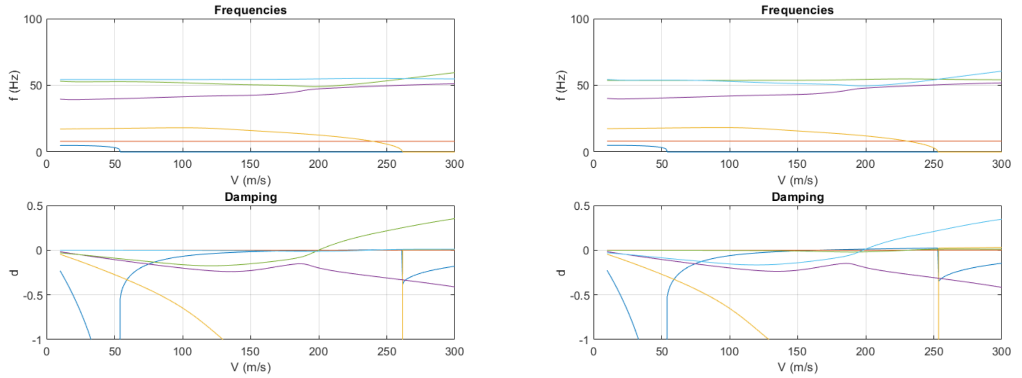

(a) spar position: 43 % of chord

(b) spar position: 47 % of chord

Figure 10.2: Frequencies and damping vs velocities diagrams

By analyzing the graphs the results presented in table 10.1 are extracted:

Spar position (% of chord)	V divergence [m/s]	V flutter [m/s]
33	213.5	199.9
37	165.7	198.1
43	137.9	184.4
47	121.6	166.3

Table 10.1: Divergence and flutter speed with different spar positions

By plotting these results (fig. 10.3) the trend of divergence and flutter speeds variation with spar position can be better understood. From the graph the quasi-hyperbolic decrease in divergence speed with the moving back of the spar is evident, as it is predicted by theory. On the other hand, flutter speed takes a different trend, with only a slight decrease in its value until the spar reaches higher downstream positions. Then its value start to decrease faster. It is clear that for wing configurations with the main spar rearmost than 34% of chord the most critical aerolastic phenomenon become divergence, as it is more sensitive than flutter to the position of the elastic axis.

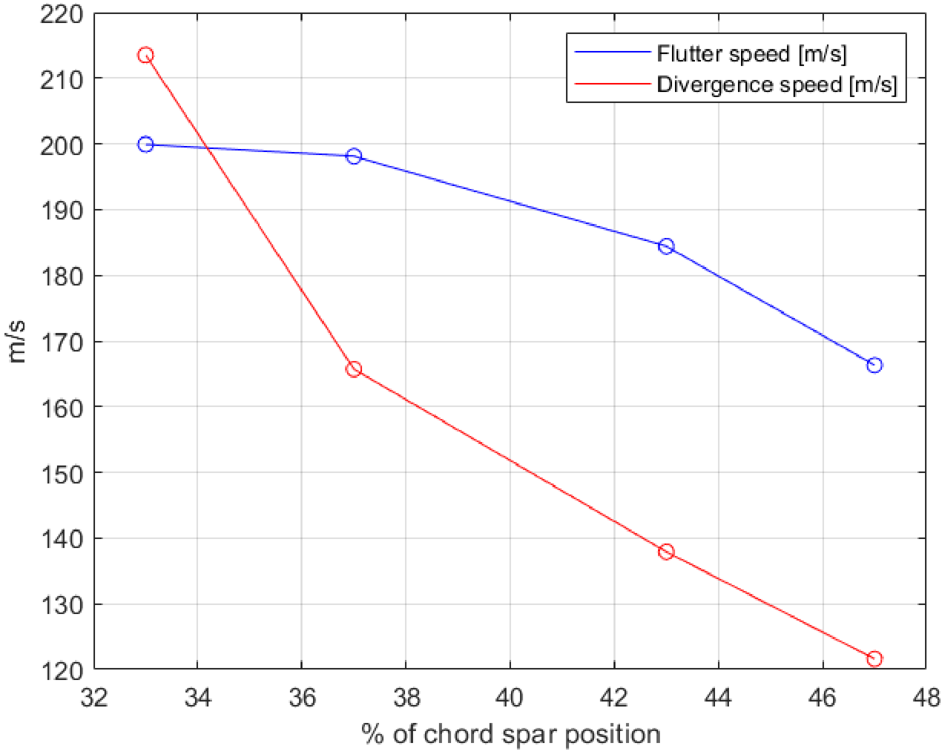

Figure 10.3: Divergence and flutter speeds variation with spar position

10.2 Evaluation of the relationship between flutter speed and Tsai's Modulus

The four wing models created previously are now used in this section to investigate the relationship between flutter speed and Tsai's Modulus.

The experiment carried on in this section consists of evaluating flutter speed using MSC Nastran on the wing models by varying material's Tsai's Modulus and then evaluate through Matlab curve fitting Toolbox the existence of a possible relationship.

The set of Tsai's moduli used to perform the analysis spans from 50 GPa to 250 GPa, considering every value equally spaced by 25 GPa between the two. The value of 118 GPa used during the wing's development is also inserted in the analysis. This range of values has been chosen as it spans a range of widely used aeronautical fiber composite materials, such as carbon fiber and fiberglass composites.

As expected the modes' frequencies increase with Tsai's Modulus, as it represent material's stiffness. This leads to an increase in the energy dissipated per cycle and therefor an increase in the flutter speed. In addition to this it can be seen that by increasing Tsai's Modulus the mode that cause flutter remains always the same (in this case the torsional mode), therefor, there will not be any non linearity due to change in the mode responsible for flutter establishment. By looking at three frequencies and damping vs velocities graphs (fig. 10.4), taken from the 33% of chord model, it looks that whatever the value of Tsai's Modulus the flutter behaviour remains analogous, as the modes evolves in the same way with speed, with the only difference that with higher Tsai's Modulus the graphs are scaled at higher speed.

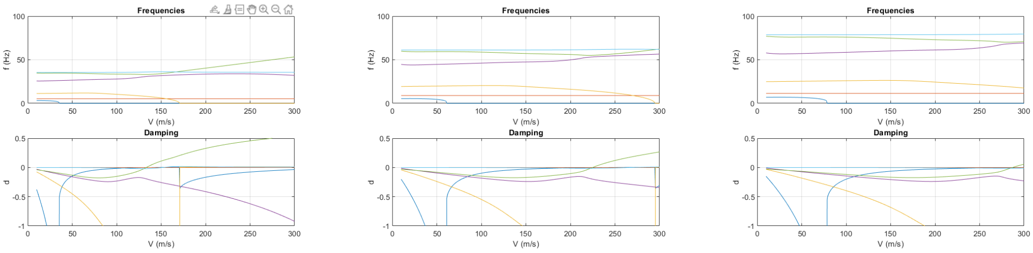

(a) $TM = 50\ GPa$ (b) $TM = 150\ GPa$ (c) $TM = 250\ GPa$

Figure 10.4: Evolution of flutter stability graphs with Tsai's Modulus

Considering now the flutter speed, in table 10.2 are reported the obtained values of flutter speed in respect to the Tsai's Modulus (TM) for the four models. For the sake of simplicity the subscripts 1,2,3,4 will be assigned respectively to the models with the main spar positioned at 33%, 37%, 43% and 47% of chord.

$TM\ [GPa]$	$V_{f1}\ [m/s]$	$V_{f2}\ [m/s]$	$V_{f3}\ [m/s]$	$V_{f4}\ [m/s]$
50	133.2	131.5	123.6	111.5
75	161.7	159.9	149.6	134.7
100	185.3	183.5	171.3	154.1
118	199.9	198.1	184.5	166.3
125	206.1	204.2	190.3	171.4
150	224.7	222.8	207.5	186.9
175	241.9	239.8	223.2	201.1
200	257.8	255.7	237.9	214.3
225	272.7	270.4	251.7	226.7
250	286.9	284.6	264.8	238.5

Table 10.2: Flutter speed in respect to Tsai's Modulus

By plotting these data (fig. 10.5) it can be seen that there is a quasi-linear relationship between the two quantities. The curves move towards lower flutter speeds and tend to be slightly less sloping as the spar position moves downstream. Interesting is to note that towards lower Tsai's Moduli the curves tend to lose by a little margin the linearity, as in the material the matrix start to assume a more important role in respect to the fiber.

Executing a linear fit with Matlab's curve fitting Toolbox the relationships that best fit the data are expressed by the following equations and represented in figure 10.6.

$$V_{f1} = 0.7488\, TM + 107.1 \tag{10.2}$$

$$V_{f2} = 0.7456\, TM + 105.6 \tag{10.3}$$

$$V_{f3} = 0.6883\, TM + 99.37 \tag{10.4}$$

$$V_{f4} = 0.6198\, TM + 89.54 \tag{10.5}$$

With velocity expressed in m/s and Tsai's Modulus expressed in GPa.

The slope m and intercept q of the linear equations are, therefor, not constant and depend on geometry, position of centre of gravity and position of elastic line of the wing.

The goodness of the fit can be expressed by the coefficient of determination R^2. It is a statistical measure of how well the regression line approximates the actual data. It is defined as:

$$R^2 = 1 - \frac{\sum_i (y_i - f_i)^2}{\sum_i (y_i - \bar{y})^2} \tag{10.6}$$

Where:
y_i: value of the experimental data;
f_i: value evaluated through the fit equation;
$\bar{y}$: mean of the experimental data.

The closest R^2 is to 1 the better the data are approximated by the fit. In the present case the value of R^2 found are:

Model	R^2
1	0.9865
2	0.9862
3	0.9870
3	0.9872

Table 10.3: R^2 values

For the present case R^2 values are pretty high, therefor the linear relationships can be assumed as a good predictor of flutter speed given a certain Tsai's Modulus.

In conclusion, given a significative range of Tsai's Moduli (that are representation of existing materials), to determine the flutter speed of a simple single material full composite wing for every Tsai's Modulus inside the range it is enough to execute two flutter analysis at the highest and lower values of the Modulus. Then, through a linear interpolation of the obtained values, every other flutter speed in corrispondence to every other material Tsai's Modulus can be determined by simply exploit the linear relationship just found. In this way, the optimal wing material, able to guarantee a desired flutter speed, could be chosen by executing only two flutter analysis, using two arbitrary low and high Tsai'Moduli, and then exploit the linear approximation.

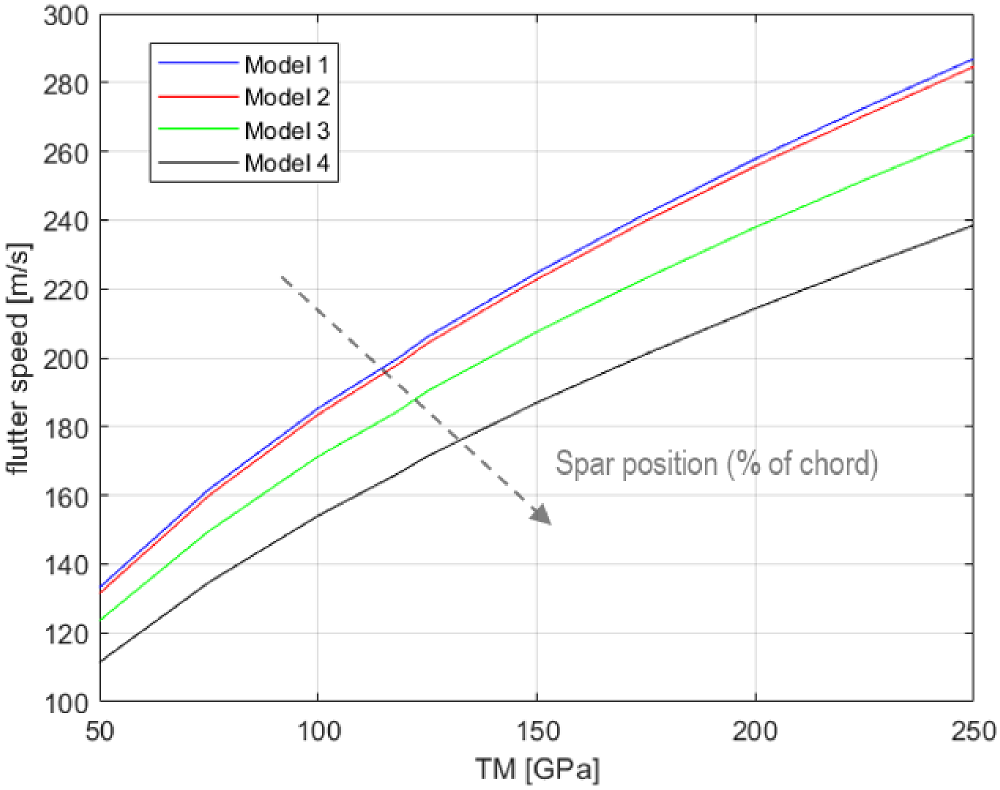

Figure 10.5: Flutter speed vs Tsai's Modulus

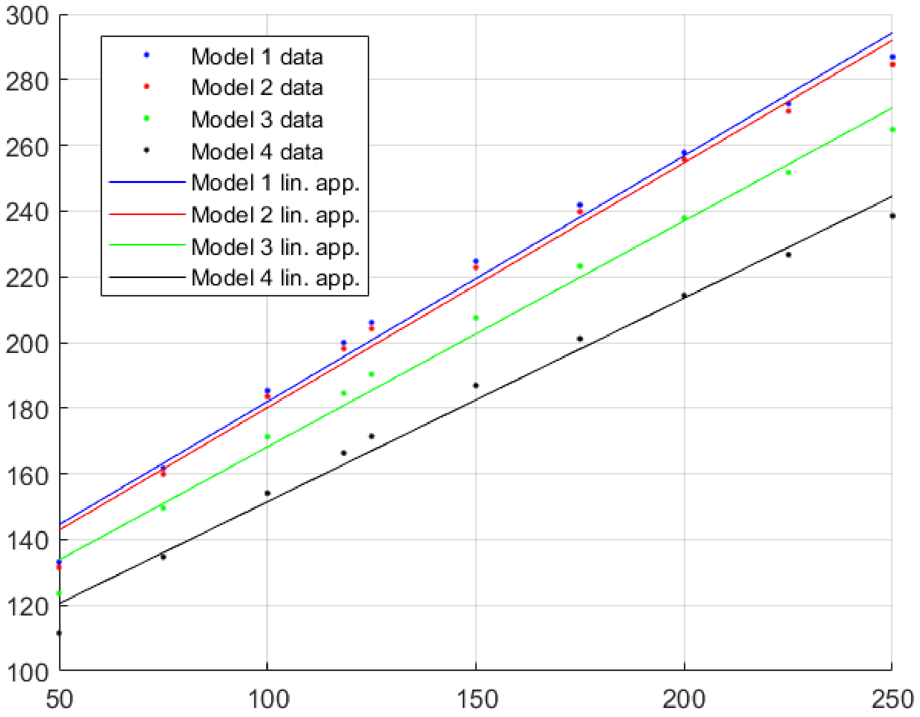

Figure 10.6: Flutter speed data vs Tsai's Modulus and linear approximations

10.2.1 Validity of the linear approximation

Let consider again the previous case study with the four models. Let find the linear equation using the lower and upper limits of the Tsai's Modulus range and their respective flutter speeds:

$$V_{f1\ app} = 0.7685\, TM + 94.78 \tag{10.7}$$

$$V_{f2\ app} = 0.7655\, TM + 93.23 \tag{10.8}$$

$$V_{f3\ app} = 0.7060\, TM + 88.30 \tag{10.9}$$

$$V_{f4\ app} = 0.6350\, TM + 79.75 \tag{10.10}$$

These are approximated linear equations found using only the end points of the range.

By inserting in these equations the same Tsai's moduli used in the case study of the previous paragraph the values of flutter speed presented in table 10.4 are found.

$TM\ [GPa]$	$V_{f1\ app}\ [m/s]$	$V_{f2\ app}\ [m/s]$	$V_{f3\ app}\ [m/s]$	$V_{f4\ app}\ [m/s]$
50	133.2	131.5	123.6	111.5
75	152.4	150.6	141.3	127.4
100	171.6	169.8	158.9	143.3
118	185.7	183.8	171.8	154.9
125	190.8	188.9	176.6	159.1
150	210.1	208.1	194.2	175.0
175	229.3	227.2	211.9	190.9
200	248.5	246.3	229.5	206.8
225	267.7	265.5	247.2	222.6
250	286.9	284.6	264.8	238.5

Table 10.4: Flutter speed values found using approximated linear equations

If these values are compared with the original ones (tab 10.2), obtained through classical flutter analysis, the differences are quite small. Evaluating relative errors in respect to the original results as:

$$e = \frac{V_f - V_{f\ app}}{V_f}\ \% \tag{10.11}$$

it is found that the error never exceed 7.5% (tab. 10.5). Therefor, for a simple single material full composite wing, executing a linear approximation between two extremes can be considered as a good predictor of flutter speed given a Tsai's Modulus inside the two limits and vice versa. Moreover, thanks to the concavity of the original flutter speed vs Tsai's Modulus curves (fig 10.5) errors will always be conservative. The magnitude of the errors can be reduced if smaller range of Tsai's Moduli are considered, so a correct choice of range of Moduli is necessary to obtain accurate results in such analysis.

10.2.2 Example of application of the linear approximation

If the envelope diagram of the wing model developed during the present thesis is considered (fig. 7.14), by the dictates of the CS 22 a minimum flutter velocity of 1.2 V_d is required to obtained a certifiable aircraft. For the present wing this flutter speed correspond to 138 m/s.

$TM\ [GPa]$	$e_1\%$	$e_2\%$	$e_3\%$	$e_4\%$
50	0	0	0	0
75	-5.74	-5.79	-5.58	-5.44
100	-7.38	-7.48	-7.24	-7.04
118	-7.11	-7.23	-6.88	-6.88
125	-7.38	-7.48	-7.23	-7.16
150	-6.51	-6.62	-6.41	-6.37
175	-5.20	-5.26	-5.09	-5.08
200	-3.62	-3.67	-3.53	-3.52
225	-1.83	-1.83	-1.81	-1.80
250	0	0	0	0

Table 10.5: Percentage error on the approximate flutter speeds

If someone would find the value of the minimum material Tsai's Modulus to not have flutter under the prescribed velocity the linear approximation could be used to find a quick and reliable result. If the usual range between Tsai's Moduli of 50 GPa and 250 Gpa is considered, the linear equation which go through the extreme points is:

$$V_{f1\ app} = 0.7685\ TM + 94.78 \tag{10.12}$$

By imposing in this equation the required flutter speed the relative Tsai's Modulus can be easily calculated, and it is equal to:

$$TM = 56.24\ GPa \tag{10.13}$$

Then, it will be simply necessary to select the material with a Tsai's Modulus close to 56.24 GPa.

To verify the goodness of the result a flutter analysis with MSC Nastran is executed on the FEM model imposing the just found Tsai's Modulus. The flutter velocity evaluated computationally is equal to 140.9 m/s. This velocity is very close to the one desired ($e = 2.1\%$), therefor the linear approximation led to a very accurate result.

10.3 Evaluation of the relationship between divergence speed and Tsai's Modulus

From the flutter diagrams of the four wing model analyzed previously is straightforward to find also the divergence speed of the wing. The divergence, in fact, can be found when a mode with null frequency value assumes a positive damping. For the present wing model the mode that causes divergence is the first bending. Therefor, an analogous investigation to the previous about flutter can be carried on also on the divergence phenomenon.

In table 10.6 are reported the obtained values of divergence speed for the four wing models.

By plotting these data (fig. 10.7) it can be immediately noted that the quasi-linear trend between Tsai's Modulus and the aeroelastic variable can be found in an analogous way to

TM $[GPa]$	V_{d1} $[m/s]$	V_{d2} $[m/s]$	V_{d3} $[m/s]$	V_{d4} $[m/s]$
50	138.5	108.2	90.0	79.7
75	170.0	132.5	110.0	97.3
100	196.6	153.0	125.9	112.2
118	213.0	165.9	137.6	121.6
125	220.2	171.1	141.8	125.3
150	241.7	187.5	155.3	137.1
175	261.7	202.5	167.6	147.9
200	280.3	216.6	179.1	158.0
225	297.9	229.7	190.0	167.5

Table 10.6: Divergence speed in respect to Tsai's Modulus

flutter also for the divergence phenomenon.

The curves move drastically towards lower flutter speeds as the spar position move downstream and they tend to be slighty less sloping. In addition to that, the curves tend to have a little negative concavity similarly to what was found with flutter. This is a confirmation that this slight non-linearity is due to mainly to the effects of the material matrix and not due to aeroelastic phenomena.

Executing the linear fit with Matlab's curve fitting Toolbox the relationships that best fit the data are expressed by the following equations and represented in figure 10.8.

$$V_{d1} = 0.8944\,TM + 103.4 \tag{10.14}$$

$$V_{d2} = 0.6813\,TM + 81.89 \tag{10.15}$$

$$V_{d3} = 0.5616\,TM + 68.12 \tag{10.16}$$

$$V_{d4} = 0.4919\,TM + 60.81 \tag{10.17}$$

With velocity expressed in m/s and Tsai's Modulus expressed in GPa.

Even for divergence the slope m and intercept q of the linear equations are not constant and depend on geometry, position of centre of gravity and position of elastic line of the wing.

The associated values of R^2 (tab. 10.7) result to be pretty high also in this analysis, in confirmation of the validity of these linear relationships.

Model	R^2
1	0.9899
2	0.9885
3	0.9889
3	0.9880

Table 10.7: R^2 values

The same conclusions as in the case of flutter can be expressed also for the divergence case. Given a significative range of Tsai's Moduli (that are representation of existing materials), to determine the divergence speed of a simple single material full composite wing for every modulus' value inside the range it is enough to execute two aeroelastic analysis at the highest and lower values of the Modulus. Then, through a linear interpolation of the obtained values, every other flutter speed in correspondence of every other material Tsai's Modulus can be determined by simply exploit the linear relationship just found. In this way, the optimal wing material, able to guarantee a desired divergence speed, could be chosen by executing only two aeroelastic analysis, using two arbitrary low and high Tsai's Moduli, and then exploit the linear approximation in the same way as done in the example executed for flutter (paragraph 10.2.2).

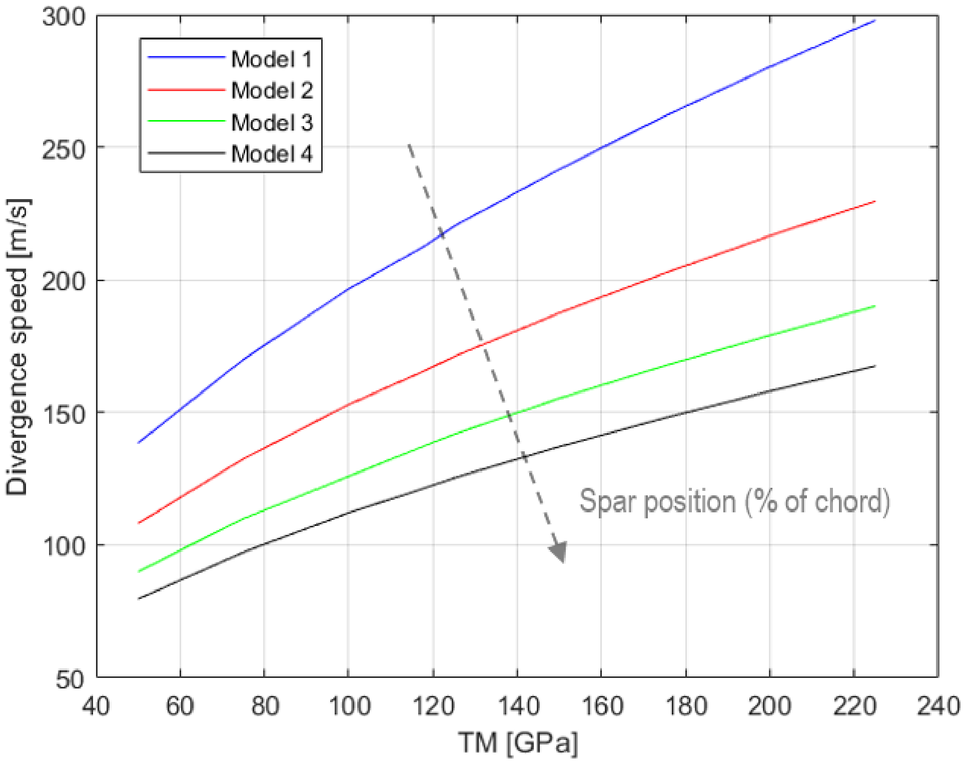

Figure 10.7: Divergence speed vs Tsai's Modulus

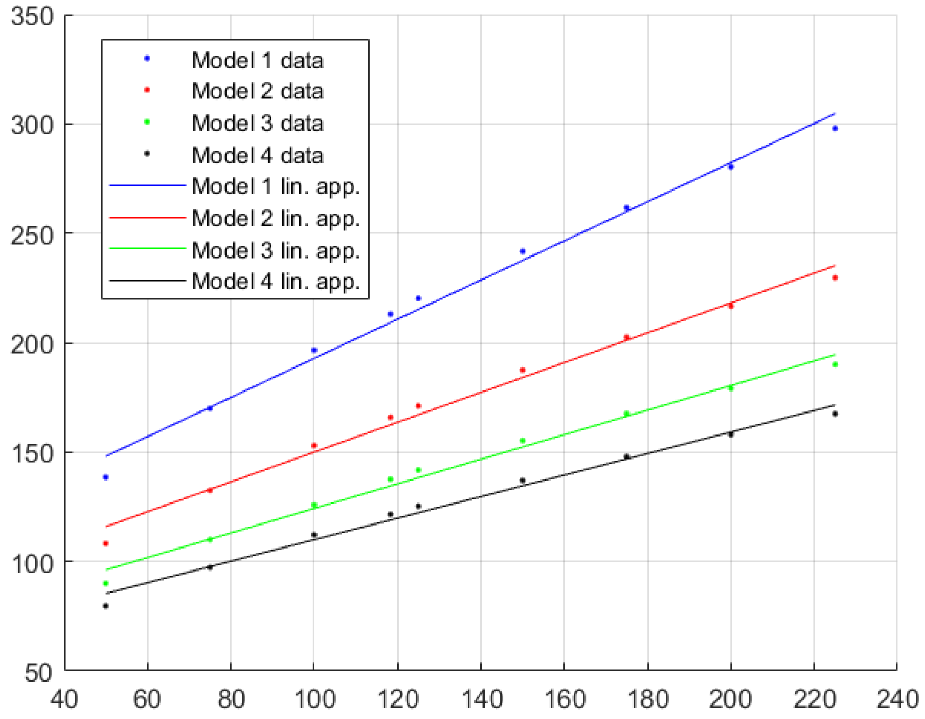

Figure 10.8: Divergence speed data vs Tsai's Modulus and linear approximations

10.3.1 Validity of the linear approximation

Let now find the linear equations using the extremes of the range as done for the flutter case:

$$V_{d1\ app} = 0.9190\ TM + 92.96 \tag{10.18}$$

$$V_{d2\ app} = 0.6943\ TM + 73.49 \tag{10.19}$$

$$V_{d3\ app} = 0.5714\ TM + 61.43 \tag{10.20}$$

$$V_{d4\ app} = 0.5017\ TM + 54.61 \tag{10.21}$$

Inserting in these equations the same Tsai's moduli used throughout the entire chapter the values of flutter speed presented in table 10.8 are found.

$TM\ [GPa]$	$V_{d1\ app}\ [m/s]$	$V_{d2\ app}\ [m/s]$	$V_{d3\ app}\ [m/s]$	$V_{d4\ app}\ [m/s]$
50	138.5	108.2	90.0	79.7
75	161.3	125.6	104.3	92.2
100	184.0	142.9	118.6	104.8
118	200.7	155.6	129.0	114.0
125	206.8	160.3	132.9	117.3
150	229.6	177.6	147.1	129.9
175	252.4	195.0	161.4	142.4
200	275.1	212.3	175.7	155.0
225	297.9	229.7	190.0	167.5

Table 10.8: Divergence speed values found using approximated linear equations

Evaluating the errors as:

$$e = \frac{V_d - V_{d\ app}}{V_d}\ \% \tag{10.22}$$

in respect to the original values evaluated with classic aeroelastic analysis (tab. 10.6) it is found that the errors never exceed 6.6% (tab. 10.9). Therefor, for a simple single material full composite wing, executing a linear approximation between two extremes can be considered as a good predictor also for divergence speed given a Tsai's Modulus inside the two limits and viceversa. Moreover, thanks to the concavity of the original divergence speed vs Tsai's Modulus curves (fig 10.5) errors will always be conservative. The magnitude of the errors can be reduced if smaller range of Tsai's Moduli are considered, so a correct choice of range of Moduli it is necessary to obtain accurate results in such analysis.

$TM\ [GPa]$	$e_1\%$	$e_2\%$	$e_3\%$	$e_4\%$
50	0	0	0	0
75	-5.13	-5.24	-5.13	-5.13
100	-6.39	-6.59	-6.39	-6.39
118	-5.77	-6.20	-5.77	-5.77
125	-6.08	-6.33	-6.08	-6.08
150	-5.01	-5.26	-5.01	-5.01
175	-3.57	-3.71	-3.57	-3.57
200	-1.85	-1.97	-1.84	-1.85
225	0	0	0	0

Table 10.9: Percentage error on the approximate divergence speeds

Chapter 11

Conclusions

A comprehensive parametric flutter analysis has been executed on a simple sailplane wing model. The novelty presented in this thesis is to investigate the relationship between the flutter behaviour of a simple wing and Tsai's Modulus, a novel invariant that measure exactly the total stiffness of an orthotropic laminated composite, exploiting classical and reliable techniques such as FEM modelling for the structure of the wing and DLM (doublet lattice method) for aerodynamics.

11.1 Outline

In the first part of this thesis a theoretical review of the main topics covered and tool used to execute calculations is present.

In chapter 2 an extensive review of aeroelasticity theory is carried on, focusing on every single component that takes part in aeroelastic phenomena, such as structural dynamics, aerodynamics and elasticity. There a comprehensive review on static and dynamic aeroelasticity is present, describing first qualitatively the phenomena and then presenting some models to predict their establishment, starting from the simpler and arriving to the state of the art, such as the p-k method, as it is the flutter evaluation method used during the present work. A brief description of aerodynamics models, in the form of VLM (vortex lattice method) and DLM (doublet lattice method), exploited for evaluating static and dynamic loads during an aeroelastic anlysis is also present. Last, the aeroelastic equations of motion that put toghether all these elements are described.

In chapter 3 a brief review of 2D FEM theory, in form of the Reissner-Mindlin element, is executed. The stiffness and mass matrices are here evluated, starting from the Reissner-Mindlin plate theory and then exploiting nodal displacements, shape functions and virtual work principle.

In chapter 4 the essence of Tsai's Modulus, the fulcrum of the presence thesis, is presented. Here, referring to Classical Lamination Theory, starting from the on-axis stress–strain relations for a unidirectional tape and then evaluating off axis relationships, the transformations relationship, using some trigonometric identities, can be rearranged in order to demonstrate that the trace of the stiffness matrix, namely Tsai's Modulus, is a material invariant. It represents the total and upper bound of the stiffness property of a material in an explicit form as defined by mathematics. This newly discovered invariant can be exploited to defined a "master ply", an universal normalized [0] ply common for every composite material.

Then in chapter 5 the software used to evaluate static aerodynamics loads, Athena Vortex Lattice (AVL), is presented. On this software, based upon vortex lattice method (VLM), the wing model has been recreated using a lattice of panels and horseshoe vortices to extract the loads to be used for the static sizing of the wing..

From chapter 6 on the computational model realized to perform the various analysis is presented. In the said chapter the construction of the parametric CAD is presented, with the reference quantities used to size it. The main parameter that can be changed is the position of the front spar relative to the chord length.

In chapter 7 is then presented in detail the FEM model realized to perform the static sizing of the wing. First, the techniques used to obtained a mesh composed of only CQUAD elements are described accurately. To this mesh are then applied the correct properties using laminates and global plies, boundary conditions and loads. The loads are evaluated through the software AVL, in a condition of maximum load factor. Then, after having built the model a static sizing based on the Tsai-Wu failure criterion is performed. Where the materials fail other layers on the laminates are added. After performing some change in the wing geometry, a configuration with no failures is obtained.

Then in chapter 8 a modal analysis to find the most significant modes to be included in the flutter analysis is performed. The first 20 modes are extracted. It was found that only the first 6 modes are interesting, as from the seventh mode on every mode is dirtied by internal trailing edge deflection. The 6 significant modes with their relative frequencies are presented in table 11.1. The validity of the calculations executed are demonstrated by comparing these results with an analytical beam model and with a FEM equivalent beam model.

Mode	Type	frequency [Hz]
1	Bending	5.04
2	Inplane	7.98
3	Bending	18.19
4	Bending	41.13
5	Torsion	53.77
6	Inplane	54.35

Table 11.1: Wing modes and associated frequencies

In chapter 9 the flutter analysis is set up and executed on the just sized wing model. The flutter method chosen is the PKNL, setting density ratio and Mach number constant and equal respectively to 1 and 0. Then, the optimal aerodynamic mesh is obtained through a convergence analysis. The best configuration found is composed by 10 chordwise elements distributed in a bias way at both ends with a bias factor of 5. Spanwise 25 elemets are present, 10 equally spaced between root section and first kink, 10 equally spaced between first and second kink and 5 equally spaced between second kink and tip. Performing the analysis on 500 equally spaced velocities between 10 and 300 m/s it is found that the wing's flutter speed is equal to:

$$V_f = 199.9\ m/s \tag{11.1}$$

and the divergence speed is equal to:

$$V_d = 213.5m/s \tag{11.2}$$

The flutter speed is the most critical of the two. Anyhow, it results to be acceptable by the means of CS22.

Finally, in chapter 10 some parametric analysis are performed to find the aeroelastic behaviour by varying main spar position and material Tsai's Modulus. By moving downstream the main spar position it is found that divergence speed decreases in a quasi-hyperbolic way as predicted by theory, whereas flutter speed decreases more gradually.
Then, the relationships between flutter and divergence speeds and Tsai's Modulus are investigated. By varying Tsai's Modulus in a range between 50 Gpa and 250 Gpa it was found that both in flutter and divergence case the evolution of the instability speeds as function of Tsai's Modulus can be approximated quite accurately by a linear law:

$$V_{f/d} = m\,TM + q \tag{11.3}$$

This relationship could be conveniently exploited to speed up the process of choice of the ideal material [1] to build a wing to resist to a certain flutter or divergence speed.

11.2 Concluding remarks

Results from the parametric aeroelastic analysis as function of Tsai's Modulus have highlighted the following key-features:

- The varying of flutter and divergence speeds as function of Tsai's Modulus for a simple single composite material wing can be accurately approximated by a linear law;
- The slope m and intercept q are not constants and must be evaluated by conducting at least two aeroelastic analysis;
- The just found linear equation can now be used to predict accurately the evolution of flutter speed with Tsai's Modulus and vice versa inside the range of Tsai's Moduli in between the two used to conduct the two original flutter analysis to find the linear equation[2].
- Pay attention to not execute the approximation on too big Tsai's Modulus ranges, as non linearity start to get more important influence on bigger ranges.

11.3 Further works

Developments of the results found seem to be interesting. In the present work the validity of the linear relationship between Tsai's Modulus and flutter and divergence speeds has been demonstrated only for a simple wing on a computational basis. It would be interesting to try to demonstrate the validity of this relationship for more complex wing structures, with more complex laminations, internal elements, flaps, or even entire aircraft. If the relationship stands true even for more complex structures then results could be verified by means of ground vibration testing, wind tunnel testing and flight testing.

---

[1] Remember that the present wing model is composed of a single composite material, therefor this statement is valid only for simple single material wings

[2] An example of this is given in paragraph 10.2.2

Moreover, since in this thesis air compressibility effects are not been taken in count, using higher fidelity aerodynamic models, able to take in count aerodynamic non linear effects, would be interesting to see how the relationship between flutter and Tsai's Modulus would change.

Appendix A

AVL wing model

The following code was created to reproduce the wing geometry on AVL. A single surface with four section was used. The four section correspond to root rib, first kink rib, second kink rib and tip.

```
    Wing
0.0                   !   Mach
0     0     0         !   iYsym  iZsym  Zsym
9.0   0.667 13.5      !   Sref   Cref   Bref   reference area, chord, span
1.0   1.0   1.0       !   Xref   Yref   Zref   moment reference
# 0.001                 !   CDp
#
#==============================================================
#
SURFACE
Wing
5   1.0  25  -2.0   ! Nchord   Cspace   Nspan  Sspace
#
# reflect image wing about y=0 plane
YDUPLICATE
     0.00000
#
# twist angle bias for whole surface
ANGLE
     0.00000
#
SCALE
  1.0   1.0   1.0
#
# x,y,z bias for whole surface
TRANSLATE
    0.00000     0.00000     0.90000
```

```
# Here the sections start
#---------------------Inner section----------------------------------------
#    Xle         Yle         Zle         chord       angle
SECTION
    0.0          0.0        0.0         0.850        0.000

#NACA
#0010

AFIL
NACA_641412.dat

#Cname   Cgain  Xhinge  HingeVec       SgnDup
CONTROL
flap      1.0    0.80    -0.01636 1.0 0.0    1.0

#------------------------First kink-----
#    Xle         Yle         Zle         chord       angle
SECTION
    0.03315      3.379       0.1768      0.740       0.000

#NACA
#0010

AFIL
NACA_641412.dat

#Cname   Cgain  Xhinge  HingeVec       SgnDup
CONTROL
flap      1.0    0.80    -0.01636 1.0 0.0    1.0

#Cname   Cgain  Xhinge  HingeVec       SgnDup
CONTROL
aileron  -1.0   0.80     -0.01636 1.0 0.0   -1.0

#--------------------------Second kink---
#    Xle         Yle         Zle         chord       angle
SECTION
    0.1071       5.852       0.306       0.493        0.000
```

```
#NACA
#0010

AFIL
NACA_641412.dat

#Cname   Cgain  Xhinge  HingeVec       SgnDup
CONTROL
aileron  -1.0   0.80    -0.0497 1.0 0.0   -1.0

#----------------------------Tip section----
SECTION
    0.2116       6.758        0.353       0.145        0.000

#NACA
#0010

AFIL
NACA_641412.dat

CONTROL
aileron  -1.0   0.80    -0.192 1.0 0.0   -1.0
#==============================================================
```

Appendix B

V-n parametric diagram definition

The parametric V-n diagram was obtained through the Octave script below. In this way the output diagram changes with the input parameters that are:

- $C_{L\ max}$;
- $C_{L\ min}$;
- Load factors in every flight fase;
- Mass to surface ratio;
- V_d;
- Wing reference surface;
- Air density.

For the gust diagram reference to the CS22 has been done, as described in paragraph 7.2.3.

```
%% manouvre
CL_max=1.51196;
n_1=10;
n_2=10;
n_3=-9;
n_4=-9;
CL_min=-0.90474;

m_s=40; %m/s [kg/m^2]
W_s=40*9.8/10; %W/S [daN/m^2]
W=3412;
Vd_lim=(3.5*W_s+200)/3.6; % [m/s]
Vd=115;
rho=1.225;
S=9;
N=1000;
```

```
n_s_1=[1:0.01:n_1];

V_s=sqrt(abs(2*W/(rho*S*CL_max)));
V_stall=V_s*sqrt(n_s_1);

W=0.5*rho*V_s^2*CL_max*S;

Va=V_s*sqrt(n_1);
Vs_neg=sqrt(abs(2*W/(rho*S*CL_min)));
Vg=Vs_neg*sqrt(abs(n_3));

n_s_3=[1:0.01:-n_3];

V_stall_neg=Vs_neg*sqrt(abs(n_s_3));



%% gust
Vb=1.1*Va;
a=6.283;
Ub=15;
Ud=7.5;

lm=0.666;
mu=2*m_s/(rho*lm*a);
H=(12.17+0.191*mu)*lm;

k=0.96*mu/(H/lm)/(0.475+(mu/(H/lm)));

np_b=1+(0.5*k*rho*Ub*Vb*a/(W_s*10));
nm_b=1-(0.5*k*rho*Ub*Vb*a/(W_s*10));

np_d=1+(0.5*k*rho*Ud*Vd*a/(W_s*10));
nm_d=1-(0.5*k*rho*Ud*Vd*a/(W_s*10));

P=polyfit([0 Vb], [1 np_b], 1);
X=linspace(0, Vd, N);
Y=polyval(P,X);

i=1;
while Y(i)<(n_1-0.01) || Y(i)>(n_1+0.01)
```

```
  i=i+1;
end

P2=polyfit([0 Vb], [1 nm_b], 1);
Y2=polyval(P2, X);

k=1;
while Y2(k)<(n_3-0.01) || Y2(k)>(n_3+0.01)
  k=k+1;
end



%% plots

hold on
fill([V_s V_stall Va],[0 n_s_1 0],'y')
fill([Vs_neg V_stall_neg Vg],[0 -n_s_3 0],'y')
fill([Va Va X(i) X(i)],[0 n_1 n_1 0],'y')
fill([Vg Vg X(k) X(k)],[0 n_3 n_3, 0],'y')
fill([X(i) X(i) Vd Vd],[0 n_1 np_d 0], 'y')
fill([X(k) X(k) Vd Vd],[0 n_3 nm_d 0],'y')
set(gca, "Layer", "top")

% plot(V_s,0,'oy')
% plot(Vs_neg,0,'oc')
% plot(Va,0,'or')
% plot(Vg,0,'og')
% plot(Vd,0,'om')

plot(V_stall,n_s_1, 'k')
plot(V_stall_neg, -n_s_3, 'k')

plot([Va Vd], [n_1 n_2], 'k')
plot([Vg Vd], [n_3 n_4], 'k')
plot([Vd Vd], [n_2 n_4], 'k')

plot([Va Va], [n_1 0], 'k')
plot([Vg Vg], [n_3 0], 'k')
plot([V_s V_s], [1 0], 'k')
plot([Vs_neg Vs_neg], [-1 0], 'k')
grid on
```

```
plot(X, Y, 'b')
plot(X, Y2, 'b')

plot([0 Vd], [1 np_d], 'b')
plot([0 Vd], [1 nm_d], 'b')

plot([X(i) Vd], [Y(i), np_d], 'b')
plot([X(k) Vd], [Y2(k), nm_d], 'b')

xlabel('V [m/s]')
ylabel('n')

np_check=1.25*(Vb/V_s)^2;
nm_check=1.25*(Vb/Vs_neg)^2;
```

Appendix C

AVL mesh convergence analysis

To find the optimal mesh to evaluate the aerodynamics loads a convergence analysis is executed. The chordwise number of elements is made vary between 2 and 12, the spanwise elements number between 5 and 50. For the chordwise sensibility analysis the number of spanwise elements is set fixed to 20, whereas for the spanwise case the chordwise elements are set fixed to 8.
As can be seen from the graphs in figure C.1, for the chordwise case the percentage error on the evaluated C_L becomes very low starting from a number of elements of 4, with an error equal to 0.204 %.
For the spanwise case the percentage error on the evaluated C_L becomes very low starting from a number of elements of 12, with an error equal to 0.131 % (figure C.2).

The chosen mesh will be composed by 5 elements chordwise and 25 elements spanwise as it is the best compromise to obtain a good data interpolation when data are imported into Femap.

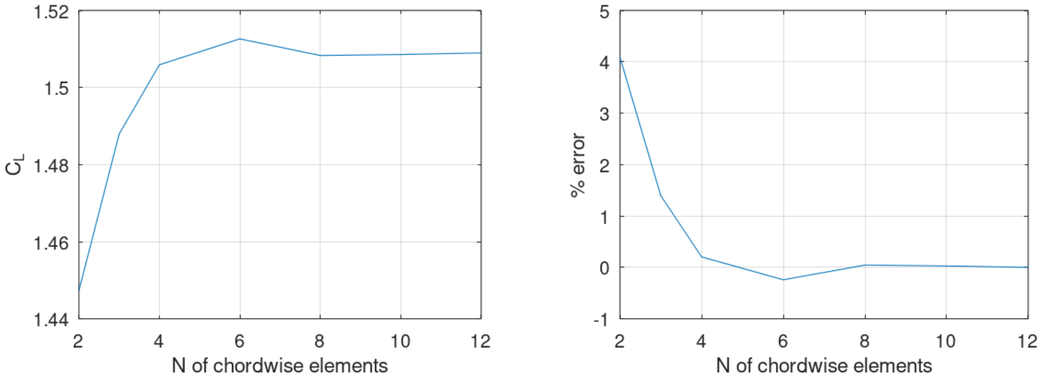

(a) C_L in function of chordwise elements (b) % error in function of chordwise elements

Figure C.1: Chordwise elements number convergence analysis

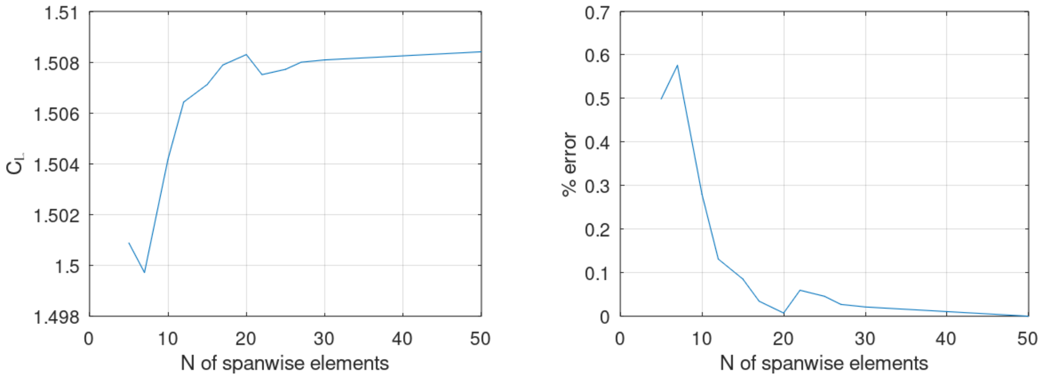

(a) C_L in function of spanwise elements (b) % error in function of spanwise elements

Figure C.2: Spanwise elements number convergence analysis

Appendix D

DLM mesh definition

The aerodynamic mesh to perform DLM for flutter analysis was defined through a convergence analysis. The chordwise elements are made varying from 6 to 20 equally spaced, whereas the spanwise elements are made varying from 25 to 60. Results are much more sensitive to chordwise elements in respect to spanwise, as can be seen from the graphs of figure D.1. Spanwise 25 elements give already good results and allow to execute a correct interpolation with FEM nodes.
In the chordwise direction accurate results can be obtained inserting a bias factor in the mesh distribution, as with a bias factor equal to 5 with 12 elements similarly accurate results as having 20 equally spaced elements are obtained. In fact, elements near leading and trailing edges are the most sensitive and reducing their dimension respect to central elements allows to obtain more accurate results.

Therefor, a mesh with 12 chordwise elements, spaced with 5 bias factor at both ends, and 25 spanwise elements is used during the analysis.

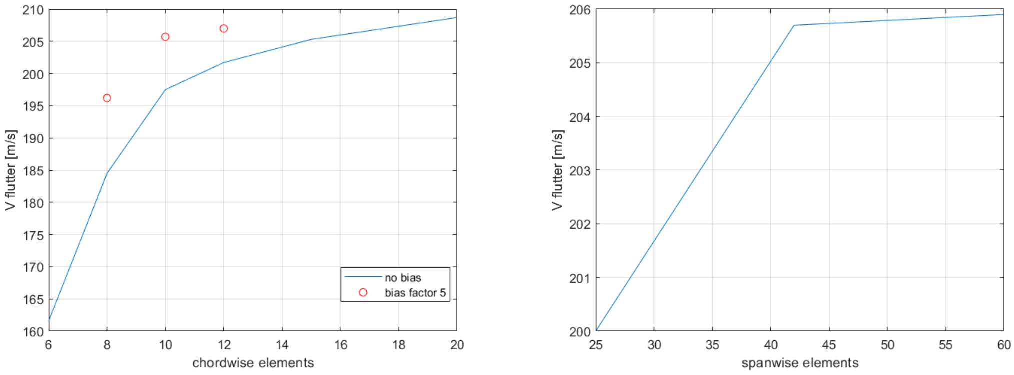

(a) V flutter in function of chordwise elements (b) V flutter in function of spanwise elements

Figure D.1: DLM mesh elements convergence analysis

Bibliography

[1] D. H. Hodges and G. A. Pierce, *Introduction to Structural Dynamics and Aeroelasticity*. Cambridge University Press.

[2] H. W. R. I. I E Garrick, "Historical development of aircraft flutter," *AIAA*, 1981.

[3] E. Albano and W. P. Rodden, "Doublet-lattice method for calculating lift distributions on oscillating surfaces in subsonic flows," *AIAA*, 1969.

[4] W. P. Rodden, P. F. Taylor, and S. C. M. Jr, "Further refinement of the subsonic doublet-lattice method," *AIAA*, 1998.

[5] R. Yurkovich, "Status of unsteady aerodynamic prediction for flutter of high performance aircraft," *Journal of Aircraft*, 2003.

[6] S. W. Tsai and J. D. D. Melo, "An invariant-based theory of composites," *ELSEVIER*, 2014.

[7] EASA, "Certification specifications, acceptable means of compliance and guidance material for sailplanes and powered sailplanes (cs-22)," in *Amendment 1*, EASA, 2008.

[8] C. V. Jutte and B. K. Stanford, "Aeroelastic tailoring of transport aircraft wings: State-of-the-art and potential enabling technologies," *NASA Technical Reports Server*, 2014.

[9] M. Shirk, T. Hertz, and T. Weisshaar, "Aeroelastic tailoring – theory, practice, promise," *Journal of Aircraft*, 1986.

[10] T. Weisshaar, C. Nam, and A. Batista-Rodriguez, "Aeroelastic tailoring for improved uav performance," *AIAA*, 1998.

[11] AIAA, "Exploring structural dynamics," *AIAA*.

[12] O. Tylén, "Fluid-structure interaction; stiffness effects on airfoil flutter," tech. rep., CHALMERS UNIVERSITY OF TECHNOLOGY, 2022.

[13] S. Qiao, J. Jiao, Y. Ni, H. Chen, and X. Liu, "Effect of stiffness on flutter of composite wings with high aspect ratio," *Hindawi*, 2021.

[14] C. J. Barnes and M. R. Visbal, "Stffness effects on laminar separation flutter," tech. rep., Air Force Research Laboratory, 2019.

[15] R. H. Scanlan, F. Sisto, E. H. Dowell, H. C. Curtiss, and H. Saunders, *A Modern Course in Aeroelasticity*.

[16] H. J. Hassig, "An approximate true dumping solution of the flutter equation by determinant iteration," *Journal of Aircraft*, vol. 8, no. 11, 1971.

[17] C. Nae, "Vlm tool for ids integration," *INCAS BULLETIN*, vol. 2, no. 1, 2010.

[18] R. Arina, *Fondamenti di aerodinamica*. Levrotto e Bella, 2019.

[19] T. M. Kier, "Comparison of unsteady aerodynamic modelling methodologies with respect to flight loads analysis," *American Institute of Aeronautics and Astronautics*.

[20] M. Petrolo, *Advanced aeroelastic models for the analysis of lifting surfaces made of composite materials*. PhD thesis, Politecnico di Torino, 2011.

[21] S. W. Tsai, J. D. D. Melo, S. Sihn, A. Arteiro, and R. Rainsberger, *Composite Laminates*. Stanford, 2017.

[22] A. Arteiro, N. Sharma, J. D. D. Melo, S. K. Ha, A. Miravete, Y. Miyano, T. Massard, P. D. Shah, S. Roy, R. Rainsberger, K. Rother, C. C. Jr., J. M. Seng, F. K. Arakaki, T.-E. Tay, W. I. Lee, S. Sihn, G. S. Springer, A. Roy, A. Riccio, F. D. Caprio, S. Shrivastava, A. T. Nettles, G. Catalanotti, P. P. Camanho, W. Seneviratne, A. T. Marques, H. T. Yang, and H. T. Hahn, "A case for tsai's modulus, an invariant-based approach to stiffness," *ELSEVIER*, 2020.

[23] S. W. Tsai, A. Arteiro, and J. D. D. Melo, "A trace-based approach to design for manufacturing of composite laminates," *J Reinf Plast Comp*, 2016.

[24] S. W. Tsai, S. Sihn, and J. D. D. Melo, "Trace-based stiffness for a universal design of carbonfiber reinforced composite structures," *Compos Sci Technol*, 2015.

[25] S. Shrivastava, N. Sharma, S. W. Tsai, and P. M. Mohite, "D and dd-drop layup optimization of aircraft wing panels under multi-load case design environment," *Compos Struct*, 2020.

[26] J. D. D. Melo, J. Bi, and S. W. Tsai, "A novel invariant-based design approach to carbon fiber reinforced laminates," *Compos Struct*, 2017.

[27] E. J. Barbero, "Universal carpet plots for stiffness and strength of carbon/epoxy laminates," *CAMX — The Composites and Advanced Materials Expo Conference Proceedings. Orlando, FL, USA*, 2017.

[28] C. Furtado, A. Arteiro, M. A. Bessa, B. L. Wardle, and P. P. Camanho, "Prediction of size effects in open-hole laminates using only the young's modulus, the strength, and the rcurve of the 0° ply," *Compos Part A-Appl*, 2017.

[29] D. Dalli, G. Catalanotti, L. F. Varandas, B. G. Falzon, and S. Foster, "Compressive intralaminar fracture toughness and residual strength of 2d woven carbon fibre reinforced

composites: New developments on using the size effect method," *Theor Appl Fract Mec*, 2020.

[30] D. Dalli, G. Catalanotti, L. F. Varandas, B. G. Falzon, and S. Foster, "Mode 1 intralaminar fracture toughness of 2d woven carbon fibre reinforced composites: A comparison of stable and unstable crack propagation technique," *Eng Fract Mech*, 2020.

[31] M. Drela and H. Youngren, *MIT AVL User Primer - AVL 3.36*.

[32] I. H. Abbot and A. E. V. Doenhoff, *Theory of wing sections*. Dover publications, 1958.

[33] S. W. Tsai, N. Sharma, A. Arteiro, S. Roy, and B. Rainsberger, *Composite Double-Double and grid/skin structures*. Stanford University, 2019.

[34] S. W. Tsai and J. D. D. Melo, *Composite Materials Design and Testing*. Stanford University, 2015.

[35] EASA, "Certification specifications, acceptable means of compliance and guidance material for sailplanes and powered sailplanes (cs-22)," in *Amendment 3*, EASA, 2021.

[36] Diab, *TECHNICAL DATA Divinycell HT*. Diab Group, 2020.

[37] L. Meirovitch, *Fundamentals of Vibrations*. McGraw-Hill, 2001.